Contribution to the study of damping in bolted structures

Marco Rosatello

To cite this version:

Marco Rosatello. Contribution to the study of damping in bolted structures. Solid mechanics [physics.class-ph]. Université Paris Saclay (COmUE), 2019. English. NNT : 2019SACLC049 . tel-02340994

HAL Id: tel-02340994
https://theses.hal.science/tel-02340994v1

Submitted on 31 Oct 2019

université
PARIS-SACLAY

CentraleSupélec

NNT : 2019SACLC049

Contribution to the study of damping in bolted structures

Thèse de doctorat de l'Université Paris-Saclay
préparée à Centrale Supélec

Ecole doctorale n°579 Sciences Mécaniques et Energétiques,
Materiaux et Géosciences (SMEMAG)
Spécialité de doctorat : Mécanique de solides

Thèse présentée et soutenue à Saint-Ouen, le 5 Juin 2019, par

MARCO ROSATELLO

Composition du Jury :

David NERON Professeur, ENS Cachan, LMT	Président
Emmanuel RIGAUD Maître de Conférences, École Centrale de Lyon, LTDS	Rapporteur
Olivier THOMAS Professeur, ENSAM Lille, LSIS	Rapporteur
Gaël CHEVALLIER Professeur, FEMTO-ST	Examinateur
Cyril TOUZÈ Professeur, ENSTA Paris Tech, IMSIA	Examinateur
Jean-Luc DION Professeur, Supméca, Laboratoire QUARTZ	Directeur de thèse
Nicolas PEYRET Maitre de Conférences - Supméca, Laboratoire QUARTZ	Co-directeur de thèse
Benoît PETITJEAN Ingénieur Expert, Ariane Group	Invité
Lionel ZOGHAIB Ingénieur Expert, Airbus	Invité

Thèse de doctorat

Contents

List of Figures

List of Tables

Acknowledgements

Getting a Ph.D. is not an easy task. However, with the right people around you, it can get a lot easier.

Firstly I would like to acknowledge the CLIMA project for founding this work and for creating an active research environment between companies and academic partners.

Then I would like to thank the figures who most influenced this work and that helped me to carry it out. The first one is my main supervisor Prof. Jean Luc Dion, who guided me in each phase of this work, always trying to bring out the best from me. I would like to thank my co-supervisor Prof. Nicolas Peyret who was always available for me, with his great knowledge of the contact physics. On the company side, I would like to thank Dr. Benoit Petitjean, my industrial supervisor at Airbus, that welcomed me in his office in Suresnes and helped me on many levels, from unveiling the secrets of the dynamics lab to giving me great technical advice thanks to his experience with jointed structures. Inside Airbus, I also would like to make a special thank you to Dr. Lionel Zoghaib, with which I had great talks about the world of research and that helped me many times during these years. A special thank you goes to Prof. Etienne Balmes, which, with his infinite knowledge of structural dynamics, made possible the construction of the finite element connector in SDTools software.

I would like to acknowledge all the members of the jury and the guests for having accepted to attend the discussion and which has shown great interest in this work. In particular, I would like to thank Prof. Emmanuel Rigaud and Prof. Olivier Thomas for carefully reviewing this thesis and for their great insights, Prof. David Neron for having accepted to be the president of the jury, and Prof. Cyril Touzè and Gaël Chevallier for their role of examinator.

I would like to acknowledge the SANDIA Laboratory of Albuquerque New Mexico, in particular, Prof. Matthew Brake, for financing and accepting my application to participate in the NOMAD Research Institute in 2016. It was a unique and essential experience for my thesis. I would also like to thank my project team members, Allen, Kelsey, and Samson, for the great moments spent in the lab.

A Ph.D. is also made of places: during these three years Supmeca, a small university with great potential and great people, has been my second family (the first one being in Italy). It's important to have nice colleagues around you during a doctorate: a very special thank you goes to Adrien C., who worked too on the CLIMA project and with whom something much deeper than a simple work relationship was developed. Mutual support in difficult moments has been crucial. Speaking of mutual support it's impossible not to mention Emna and Reza: our coffee break talks really made my day on countless occasions. A huge acknowledgement goes to

Adrien G., who introduced me to the Kalman Filter and helped me to understand when it didn't want to work. Getting out of the office, the next acknowledgment goes the team VAST, a group of dynamic people from which I've learned a lot. I would like to thank all the staff of Supmeca, always available and reactive to help me solve my problems, especially when I was new to the school and my French was not that good.

A particular thank you goes to a special group of friends that created in Supmeca and with which I've shared wonderful moments. Therefore thank you, Adrien, Alain, Alexandre, Jpal, Paul, Sophie, and Stefania.

During the period of my thesis, I had the chance of organizing the JJCAB 2017, between Supmèca and the CNAM. Therefore, I would like to thank the organization group Aro, Arthur, Christophe, Martin et Sylvain.

I would like to thank my family, that made the graduation day a very special one and that always supported me even if I was far from them during all these years.

Finally, I would like to thank Pauline, without whom anything of this would have happened. Thank you for sharing every single moment of this adventure with me.

Résumé

Introduction

La dynamique des structures assemblées est un sujet de recherche d'actualité. Plus précisément, une prédiction correcte de l'amortissement apporté par les liaisons boulonnées est devenu une condition essentiel pour un certain nombre d'applications, comme par exemple les véhicules aéronautiques et spatiaux. En effet, pour ces applications,l'utilisation de matériaux avec un coefficient d'amortissement plus élevé, comme les matériaux visco élastiques, est limité par les conditions de fonctionnement. Dans ces cas, les sources principales d'amortissement proviennent des liaisons vissées, essentiellement dû au frottement qui a lieu à l'interface entre les composants. L'évaluation de l'amortissement apporté par les liaison vissées est le sujet principal de ces travaux.
Le problème rencontré par les chercheurs sont est le fait qu'une méthode pour la prédiction de l'amortissement d'une structure assemblée n'existe pas. Donc, les liaisons boulonnées sont conçues en tenant compte des normes existantes, mais le comportement dynamique est évalué seulement une fois que la structure a été construite, ce qui peut impliquer des pertes de temps considérables. La raison principale pour laquelle l'évaluation de l'amortissement des structures assemblées est compliqué, vient du fait que son comportement est de type non-linéaire. Toutefois, la nonlinearité n'est pas toujours très marqué, ce qui permet parfois l'utilisation d'outils d'identification modale linéaire, avec quelques précautions et hypothèses.

Chapitre 1

La thèse fait partie d'un projet important appelé *Projet CLIMA -Conception de LIaisons Mécaniques Amortissantes*, un projet collaboratif de recherche FUI. Ce type de projet supporte la recherche appliqué de façon transversale. En fait, il permet la connexion entre grandes, moyennes et petites entreprises, ainsi que des laboratoires de recherche.
Les objectifs du projet CLIMA peuvent être divisés en quatre aspects:

1. Conception: création et prototypage de liaisons avec un haut pouvoir dissipatifs, sans influencer l'intégrité structurelle;
2. Contrôle: développement de nouveaux capteurs et actionneurs pour mesurer et modifier les propriétés des liaisons;
3. Modélisation: développer un outil numérique pour l'optimisation de l'amortissement dans la phase de conception;
4. Évaluation: développer un set d'outils de post-traitement pour la détermination de l'amortissement non-linéaire des structures assemblées.

Les travaux présentés sont focalisés sur les objectifs de modélisation et d'évaluation. En fait, le défi d'évaluer l'amortissement dû aux liaisons vissées sera approché par deux cotés. D'une part, une formulation analytique du problème de contact à l'interface de la liaison sera présentée et implémentée dans les éléments finis, afin de prédire l'amortissement dans la phase de conception. D'autre part, un set d'outils adaptés aux liaisons boulonnées sera développé pour évaluer le comportement dynamique d'une structure assemblée soumise à différents types d'excitation.

Chapitre 2

Les liaisons boulonnées, entendues comme l'utilisation d'une vis et un boulon pour connecter deux pièces, font leur apparition dès le 15ème siecle. A l'époque, ils étaient faits à la main, et c'était très difficile de faire deux filets correspondants. Aujourd'hui, les dimensions des vis, des boulons et des filets sont strictement normées, comme il est également le dimensionnement des liaisons. Toutefois, le comportement de ce type de liaisons est toujours un sujet de recherche, en particulier en ce qui concerne leur comportement dynamique.

Il peut être intéressant de comparer le comportement dynamique, en particulier concernant l'amortissement,d'une structure avec une liaison boulonnée et la même structure, mais cette fois monolithique et sans liaison. La structure boulonnée aura un taux d'amortissement plus élevé que la structure monolithique. Ce comportement est dû au frottement qui survient dans l'interface de contact. En outre, le taux d'amortissement évolue de façon non-linéaire avec l'amplitude d'excitation et il dépend de plusieurs facteurs caractéristiques des liaisons, dont le niveau de pré-charge de la vis, les dimensions de la vis, la conformabilité des surfaces en contact, la direction de l'excitation, la forme des modes propres sollicités et autres paramètres.

Vu l'importance du frottement dans la dynamique des liaisons,les modèles principaux sont décrits, en faisant la distinction entre macro-modèles et modèles constitutifs. Les macro-modèles sont basés sur des lois empiriques et/ou des observations expérimentales, lorsque les modèles constitutifs dérivent de la physique du contact. Les macro-modèles peuvent être divisés en modèles statiques (Coulomb, Stribeck), dynamiques (Dahl, Valanis) et hystéretiques (Masing,Iwan). Une fois la description des différents modèles de frottement est faite, une liaison entre le modèle constitutif de Mindlin et le modèle hystéretique de Dahl est trouvée. Ce lien sera utilisé dans la phase de modélisation du chapitre 3.

Dans la dernière partie du chapitre 2, une structure de référence, la poutre de Brake-Reuss, est étudiée expérimentalement et numériquement, et les résultats sont montrés. Enfin, une discussion sur le caractère multi-échelle des structures assemblées est amenée.

Chapitre 3

La simulation numérique des structures assemblées n'est pas une tache facile. Le problème principal vient du fait que les liaisons représentent une petite partie de la structure, ce qui génère un problème multi-échelle, très lourd à résoudre numériquement par la méthode des éléments finis. L'autre aspect à considérer est que la physique du contact des liaisons demande une modélisation détaillée, en particulier en ce qui concerne le frottement.

Le premier objectif de ces travaux est de trouver une méthode de modélisation pour la dynamique des liaisons boulonnées. Un état de l'art est accompli sur les techniques de modélisation des liaisons boulonnées couramment utilisées. Ensuite, dans le cadre des travaux de thèse, un système original de connecteurs est développé. L'idée de ce système est de réussir à modéliser le comportement des liaisons à partir seulement de ses paramètres physiques (dimensions, géométrie des surfaces en contact, rugosité, jeux entre les composants, etc.). Le système développé est constitué par deux connecteurs: le premier modélise le comportement de la vis, des boulons et, le cas échéant, des rondelles. Le deuxième décrit le contact normale et tangentiel entre les surfaces en contact. Pour le contact normal, le modèle de Greenwood-Williamson est utilisé, pour le contact tangentiel et le frottement, le modèle de Dahl est appliqué. Tout les paramètres des modèles sont calculés à partir des données disponibles sur la définition de la liaison.

L'implémentation du connecteur a été réalisée dans le logiciel SDTools, une toolbox de dynamique structurelle basée sur MATLAB. Le système de connecteurs a été appliqué sur une des maquettes développées pour le Projet CLIMA, pour laquelle une campagne expérimentale a été menée. Les résultats obtenus numériquement avec le nouveau système de connecteurs ont été comparés aux données expérimentales. Les résultats ont montré que le système développé est capable de modéliser le comportement non-linéaire typiques des liaisons. Par contre, les paramètres du système a dû être recalés pour avoir une correspondance précise avec les résultats expérimentaux. Toutefois, la solution développée représente un bon compromis entre precision des résultats, simplicité d'usage et implémentation pour une usage de type industriel.

Chapitre 4

Après la partie de modélisation, l'autre objectif de ces travaux est d'identifier l'amortissement d'une structure boulonnée à partir des données expérimentales. En particulier, le développement d'un set d'outils adaptés aux structures assemblées et à différents types d'essais a été développé.

La base commune des méthodes développées est l'utilisation du filtre de Kalman, un outil très puissant qui, dans ces travaux, a été adapté pour amener une identification modale non-linéaire de haute precision. Le filtre a été crée par Rudolph Kalman en 1960 et il a été utilisé pour une vaste gamme d'applications, par exemple dans le secteur de la navigation, contrôle, optimisation de la trajectoire, en particulier pour de véhicules aéronautiques et spatiaux. Par définition, le filtre de Kalman est un algorithme d'estimation optimale, dont l'objectif principal est de suivre l'évolution en temps d'un système dynamique. La première formulation originel du filtre de Kalman est linéaire, mais ils existent plusieurs versions non-linéaires. Une description étendue des différents types de filtres de Kalman est fournie dans ce chapitre.

Dans ces travaux la formulation du filtre utilisée est le *Unscented Kalman Filter*. Trois méthodes d'identification non-linéaires sont développées: la première pour les essais aux chocs, la deuxième pour les essais au balayage sinus et la troisième pour les essais au sinus aléatoire. La base d'identification de ces trois méthodes développées est la suivie en temps d'un signal sinusoïdal générique par le filtre de Kalman. Ce procédé de suivie utilise le concept de signal analytique pour reconstruire le signal mesuré et extrapoler les caractéristiques modales d'un système.

Les méthodes pour les essais aux chocs et aux balayages sinus sont décrites et validées avec succès sur un cas test à 1-DDL incluant un modèle d'Iwan qui simule la non-linéarité d'une liaison. Ensuite, une description et une petite guide sur la délicate phase d'initialisation du filtre de Kalman sont fournis avec un exemple sur le cas test. L'initialisation du filtre reste la tache plus lourde dans son utilisation, surtout parce que sans une initialisation correcte, le filtre ne convergera pas ou, encore pire, convergera sur des résultats incorrectes.

En concernant la méthode pour les essais aux sinus aléatoire, elle est décrite mais elle ne sera pas implémentée.

Chapitre 5

Tout au long du projet CLIMA, plusieurs campagnes expérimentales ont été réalisées sur plusieurs maquettes. Les méthodes développées dans le chapitre 4 ont donc été testées sur la maquette principale du projet, la maquette AERO. Une procédure précise de pre-test a été effectuée pour déterminer numériquement les meilleurs points d'excitation et de support pour la structure étudiée.
Ensuite une campagne expérimentale d'essais au choc et en balayage sinus a été réalisée. Les méthodes basées sur le filtre de Kalman ont été appliquées aux données expérimentales et les résultats sont très positifs. Pour les deux méthodes, il a été possible de visualiser la non-linéarité sur les fréquences propres et l'amortissement apportées par les liaisons boulonnées, même avec des niveaux d'amortissement très faibles. Différentes configurations de la maquette ont été testées, en changeant le couple des serrage des vis, le nombre de vis et après désassemblage et assemblage.
Les résultats montrent que les méthodes développées peuvent être appliquées à des cas réel et qu'elles sont très résistantes au bruit et arrivent à déterminer la non-linéarité sur des amortissement très faibles, de l'ordre de 0.05%.

Conclusion

La contribution principale de cette thèse a été d'explorer et d'étendre la connaissance sur la dynamique des liaisons boulonnées, dans un premier temps avec la conception d'une méthode de modélisation des liaisons et, dans un deuxième temps, avec le développement d'un outils de post-traitement originale, basé sur la technique du filtre de Kalman. Les résultats obtenus sont encourageants. Par contre, les projets futures liés à ces travaux doivent passer par une meilleure description des surfaces en contact pour la partie modélisation, et par une automatisation ou simplification de l'initialisation du filtre de Kalman.

Introduction

Sometimes we give for granted aspects of our *engineering* life that have been around and used for centuries. This thesis is about one of them: bolted joints.

Bolts and nuts can look like basic tools of which we know everything and could even be considered as a boring thesis topic. However, the static dimensioning of bolted joints is still an ongoing research topic, even if a large number of norms and directives exists. Here is where we have to introduce the dynamic part of the story. In fact, when a metallic structure undergoes a dynamical excitation, it's important that the vibrations are damped in order to reduce their amplification at the resonances. Since metals material damping is usually very low, the damping is usually provided by the deployment of visco-elastic materials. However, there are certain applications, especially in the aeronautical and aerospace fields, where, due to the particular environmental conditions, visco-elastic materials are not suitable. In these cases the main sources of damping become the bolted joints, due the friction that can take place at the contact interface of the assembled parts. Therefore, the evaluation of the bolted joints' damping potential is the main topic of this thesis.

The current problem with which researchers and engineers working on assembled structures dynamics are dealing with, is that a method to predict the damping contribution of bolted joints does not exist. Therefore, bolted joints are designed according to the existing norms, and the dynamical behavior is evaluated only after the structure has been built. Useless to say, this leads to time losses and to an iterative validation process.

The challenge of evaluating the damping due to bolted joints will be tackled from two directions. On one hand, an analytic formulation of the contact problem at the bolted joint interface will be designed and implemented into finite elements, in order to predict the damping in the design phase. On the other hand, a set of tools, particularly adapted to bolted structures, will be developed in order to carefully evaluate the dynamic behavior of bolted structures undergoing different types of tests.

The main reason why the damping evaluation of assemblies is complicated, is that their behavior is nonlinear, ie the natural frequencies and damping coefficients are nonlinear functions of the displacement amplitude. However, we are still lucky because bolted structures are only slightly nonlinear, which means that sometimes linear identification tools can still be used, with the necessary precautions and assumptions.

In Chapter 1 the context of this work will be described, with a particular attention to the project of which this thesis is part and to the players involved.
In Chapter 2 an extensive state of the art will be provided, describing the typical nonlinear behavior of bolted structures and how they are studied in the community orbiting around this topic. Furthermore, real examples and numerical investigations performed by the author will be supplied to give a complete and exhaustive overview of the problematic under study.
Next, Chapter 3 will talk about the design of a finite element connector system to numerically model the full behavior of bolted joints. The several laws implemented in the system will be thoroughly described. Finally the numerical model will be tested and evaluated for an application on a real structure.
In Chapter 4 a nonlinear post-processing set of tools based on the Kalman filter method will be outlined and applied on simple nonlinear test cases.
Finally, in Chapter 5 the same post-processing tools will be applied on real experimental data from a test campaign on a mock-up structure developed by the project in which the thesis is inserted.

All illustrations and graphs that the reader will find throughout this thesis, except where differently specified, are entirely created by the author.

1

The CLIMA Project

Contents

Summary This thesis is part of a large project called *Projet CLIMA - Conception de LIaisons Mécaniques Amortissantes* — *Design of Dampening Mechanical Joints*, an R&D collaborative FUI project. The FUI (*Fonds Unique Interministeriel* is a program that supports the applied research, in order to develop new products and services to be put on the market in the short or medium term. The interesting aspect of an FUI project is its *collaborative* nature: in fact, it allows connections between larger established companies, smaller emerging ones, universities and laboratories. In this first chapter the CLIMA project, its context, its partners and its goals are briefly described.

1.1 Context

The prediction of a structure dynamic response is a crucial task in the design process. In particular, a good prediction of the structure damping is critical in order to be able to design a structure that meets specifications and, even more important, doesn't fail under operating conditions. The structures interested by the project belong to the aeronautics and aerospace fields, in which the importance of accurately predicting the damping behavior is higher than in other areas of study. By being able to correctly predict the damping of an assembly it will be possible to have a better control of the vibration levels to which the structure is submitted. The latter aspect has very important industrial fall-outs. If we take for example a space launcher, it will be possible to reduce the vibrations to which its payload is submitted. In fact, the payload usually consists of expensive and delicate structures such as satellites or measurement equipment that are sensitive to vibrations. Another example is a plane fuselage and the internal cockpit: if the vibrations transmitted by the joints are reduced, the comfort inside the cockpit will be improved, both mechanically and acoustically. The same is obviously valid for a car interior.
The CLIMA project is not the first of its kind, but it takes place from a rich history of projects dedicated to the damping characterization of jointed structures. To give some examples:

- **MAIAS**: partially the precursor of CLIMA, it produced several test benches on which the first results on damping prediction have been obtained. In addition, a set of software prototypes for dynamic test post-processing have been developed and some of the technologies used in the CLIMA project have been conceived during MAIAS.
- **CARAB**: the objective of this project was to develop and validate a set of methods and tools that can be used to optimize bolted assemblies for aerospace products. The focus of the CARAB project was mainly on the *static* or quasi-static behavior of bolted structures, while the CLIMA project focuses on their *dynamic* behavior.
- **ARIAN**: the project focuses on the prediction of damping in bolted interfaces between composite structures, with a particular interest on the space rocket Ariane.
- **INMAT**: a slightly different project, where the damping function is obtained through the development of new materials. Jointed structures are not treated.

It's also worth noting that besides the cited French projects, there is an international community, the *ASME Research Committee on the Mechanics of Jointed Structures (RCMJS)*, which sets the research roadmap for the community itself and regularly organizes and collaborates on a series of actions and challenges. The RCMJS is currently led by a committee consisting of David Ewins (Imperial College London), Larry Bergman (University of Illinois), Dan Segalman (Michigan State University), and Matthew Brake (Rice University). Furthermore, Supméca and FEMTO, the first being the university where this thesis was conducted and the second being a research institute partner of the CLIMA project, are active contributors of this community.
The existence of many projects and of an international committee gives an idea of how important is the knowledge of bolted structures dynamics and how much work is still there to be done.

1.2 Partners

A project, like any good movie, needs good actors in order to be successful. The industrial *actors* of the CLIMA project are:

- **Airbus**: the well known aeronautic and space European industrial group, previously known as the EADS (Europen Aeronautic Defence and Space).

- **Sopemea**: a set of laboratories specialized in all range of testing services in the fields of mechanics, vibration, climate, electricity, hydraulics and electromagnetic.
- **ADR-Alcen**: a producer of high-precision ball bearings, special electromechanical actuators, and mechanism for electro-optical applications.
- **Aderis**: company specialized in bonding technologies through advanced polymers.
- **AVNIR Engineering**: a mechanical engineering consultancy firm for the aerospace and energy industry.
- **CEDRAT Technologies**: company specialized in smart actuators, smart sensors, mechatronic and detection systems.
- **SDTools**: a software company providing a complete structural dynamics toolbox based on MATLAB®
- **Texense**: a producer of high-tech embedded sensors for sports mechanics and automotive and aerospace industry.

Concerning the academic partners, these are:

- **Supméca**: an engineering school, part of the ISAE group, where this thesis was carried out.
- **Femto-st**: a research institute attached to the CNRS (Centre Nationale de Recherche Scientifique).

Each of the partners makes its expertise available to the project in order to reach the established goals.

1.3 Project Goals

The objectives of the CLIMA project can be divided into four different fields:

1. **DESIGN**: Create and prototype joints with a high dissipative potential by understanding the physics behind the energy dissipation. Of course, the new joints must not interfere with the integrity of the structure.
2. **CONTROL**: Develop new sensors and actuators for the measurement and control of the joints properties. For example, during the MAIAS project, some bolts were instrumented in order to measure the instantaneous bolt load.
3. **MODELING**: Develop a modeling and simulation numerical tool for the damping optimization of an assembly in the design phase.
4. **EVALUATION**: Develop a toolbox for the post-processing of different types of tests on jointed structures, capable of evaluating the nonlinear modal properties.

The array of goals fixed by the CLIMA project produces a comprehensive and exhaustive set for the analysis and design of jointed structures.

1.4 Thesis Goals

As it can be presumed, the thesis goals cannot include all of the project goals. A first selection has to be made on the type of joints that are studied. In fact, the CLIMA project involves the study of two different assembly techniques:

- Metallic joints: they put directly in contact two or more metallic interfaces.
- Viscous joints: they link metallic or composite components using glue only, or they combine the use of viscous materials with traditional metallic joints.

This thesis will only consider the metallic joints. Furthermore, concerning the goals set up by the project, the current work will mainly focus on the **MODELING** and **EVALUATION** fields. To accomplish the first, a FEM connector system will be developed and numerically implemented with the help of the project partner SDTools. Then, in order to accomplish the second goal, a post-processing toolbox that uses the Kalman filter theory will be developed. Both for the modeling and evaluation tasks, reference experimental data on which to validate the FEM connector and the post-processing toolbox will be necessary. To accomplish that, there have to be one or more reference structures on which to carry out the experimental tests. During the project, several test benches have been designed and manufactured to explore different joints technologies.

1.5 Project Mock-ups

The design of the mock-ups, directly belonging to the project, allows its members to have a set of structures around which it's possible to create hypotheses, design specific tests, run numerical simulations and share their results. Four mock-ups have been developed for the CLIMA project, three of which are related to metallic joints and used in the present work. The latter will be briefly described in the next paragraphs.

1.5.1 ORION Mock-up

This structure was developed in order to have a simple configuration on which is possible to study and understand the physics behind bolted joints. The mock-up, shown in fig.1.1, consists of two aluminum parts linked together by three M4 bolted joints. The particularity of this mock-up is the fact that, on one of the two parts, a milling process is carried out to obtain three squared raised zones around the holes. This is done in order to let the contact take place only on the areas around the holes and avoid interactions with the rest of the surface. The mock-up it's easy and cheap to reproduce, which makes it easier to use as a reference structure. In addition, it provides a simple case to test newly developed methods and theories.

1.5.2 AERO Mock-up

The second and main mock-up of the CLIMA project is the structure shown in fig.1.2. The objective of this type of design is to reproduce the joints found in aeronautical and aerospace real applications in order to evaluate their influence on the structural dynamics behavior. The mock-up consists of a center caisson which is joined to two wings through a connecting plate and bolted joints. The chosen shape takes inspiration from the Airbus A380 wings, with the intent to make it both a satisfactory test bench and an iconic and representative object for the CLIMA project.
The material used for all of the mock-up components is the aluminum alloy 7075, which has

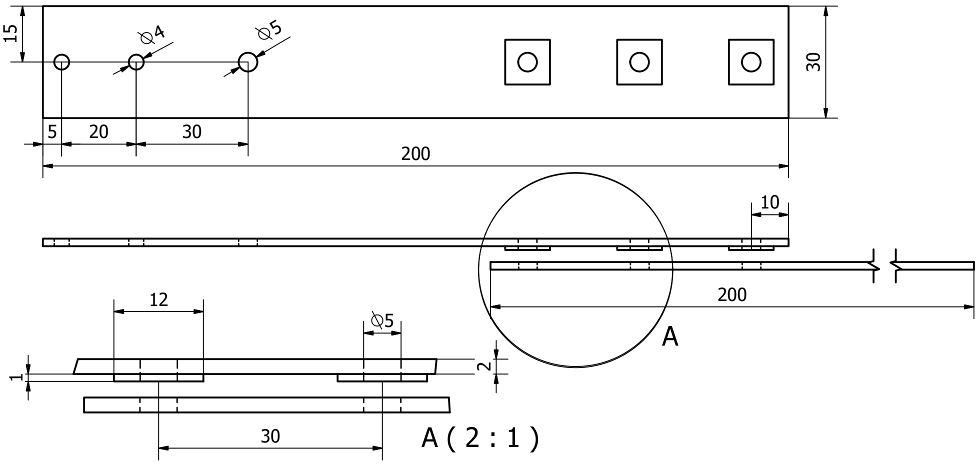

Figure 1.1 – Mock-up ORION (dimensions in millimeters)

the zinc as primary alloy element and it's often used in transport applications (mainly aviation) due to its high strength-to-density ratio.

The connection between the center block and the wings is shown in fig.1.3. The upper part uses a link plate to connect the caisson to the wing. The link plate is mounted on the caisson with a row of eight M10 bolts, directly fitted in steel threaded inserts introduced in the center block. The other side of the link plate is then connected to the wing through a row of twelve titanium close tolerance bolts with a diameter of 6.35mm. The lower part directly connects the center block to the wing, again with a row of twelve titanium bolts. The nominal torque for the titanum bolts is 7Nm. In addition, the wings have been hollowed out, which was done not only to make the final structure lighter but also to be able to mount two metallic covers to test bolted joints mixed with polymers.

The wingspan of the assembly is slightly less than 2m and the total weight is close to 30kg, which makes it quite an imposing structure to test.

Figure 1.2 – Mock-up AERO

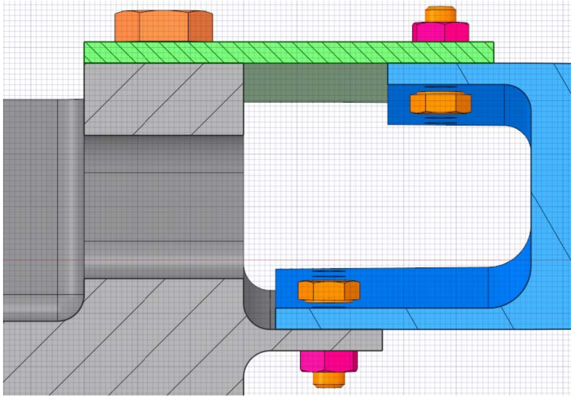

Figure 1.3 – Joint system between center caisson and wing

1.5.3 Mock-up ADR

The last mock-up dedicated to metallic joints is taken from the MAIAS project. The objective is to develop dissipative bolted joints for a system with high-precision ball bearings by operating on the profile of the contact surfaces. The mock-up, shown in fig.1.4, is entirely made of stainless steel X105CrMo17, and it consists of a base, a mass, and a *bearing* ring. The latter is certainly the most interesting part of the structure because it has been designed to have the same stiffness behavior of the ball bearing present in the real system, in order to make it easier to construct a numerical model. In fact, a ball bearing would have been too difficult to correctly mesh and the related simulations too computationally expensive.
The connections studied by the project are the twelve circular bolted joints that fix the ring to the base. The idea is that, by introducing a custom designed ring between the base and the *bearing* ring, is possible to increase the damping of the structure.

Figure 1.4 – Mock-up ADR

1.6 Conclusion

The set of mock-ups described in these sections have been utilized by the project members as a reference to test different types of solutions and to advance in the knowledge of bolted structures and assemblies. After having described the nature of the project in which this thesis is placed, it’s now time to understand how bolted structures behave, what are their common features, what we know and what we don’t know yet, and how their study is approached by the international academic community interested in this subject.

Bolted structures dynamics

2

Contents

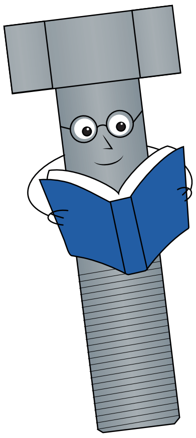

Summary Imagine having to build a car or a plane, or even a simple IKEA® table without any bolts or screws: this is simply impossible or VERY unlikely. This chapter is meant to give the reader a complete overview on the topic of bolted structures. At first, the general behavior and the properties observed till the present days will be described. Then, a review of the main methods for modeling friction in bolted joints will be carried out, since this is how the energy is dissipated and the damping is provided. Finally, a simple bolted structure will be analyzed to consolidate the theoretical knowledge and to show the problems and the challenges in the study of bolted joints.

2.1 General behavior of bolted joints

In most of the mechanical fields and applications it's very likely that at a certain point an engineer will have to decide which type of fastening method to use in order to assemble different components. The most common kinds of fasteners are nails, screws, bolts and rivets. Bolts and rivets have been used extensively in automotive and aviation applications. The difference between them is that, while rivets are permanent joints, bolts and nuts provide a non-permanent way of assembling different components. The concept of using a threaded bolt and a matching nut as a fastener dates back to the 15th century [23], when they were made by hand and, because of that, it was quite difficult to produce matching threaded profiles. Today there is a wide range of bolt types available for general and specific applications and, most of all, their dimensions are standardized. In addition, the design of bolted structures is subject to regulations and directives in order to avoid joints failure and fatal accidents.

However, even if bolted joints are commonly used in all types of engineering structures, their behavior is still a research topic, especially concerning their influence on the dynamics of the assembly.

2.1.1 The monolithic-assembly comparison

The most direct and easy way to understand the effect of bolted joints on the dynamic of a structure is to compare the behavior of a jointed structure with its corresponding monolithic one [9, 37, 47]. An illustrative example is shown in fig.2.1 where, on the left, is possible to see a lap-joint while, on the right, the corresponding monolithic version.

If we were to excite these two structures with an impact hammer, we would obtain a free vibration response like the one shown in fig. 2.2. The decay rate for the jointed model is higher than for the monolithic one, which means that the damping for the lap-joint is higher than the damping of the monolithic version. This is due to the fact that the only source of damping for the monolithic structure is the material damping, which is small for metallic materials—usually less than 0.1% ([35])—while for the jointed structure the additional damping is the result of the energy dissipated by friction at the contact interface.

In the early 1960s Ungar [49] performed a series of tests where he used the dependence between the dissipated energy per cycle and the load amplitude to identify the source of dissipation. The dissipated energy per cycle D can be written in the following power-law form:

$$D \propto A^{\delta} \tag{2.1}$$

where A is the oscillation amplitude and δ is the power-law coefficient. Ungar started to visualize the results of his experiments on a log-log plot with the force or displacement amplitude on the x-axis and the dissipated energy per cycle in the y-axis. In this way, if a power-law behavior is detected, it will be looking like a straight line with a slope δ.

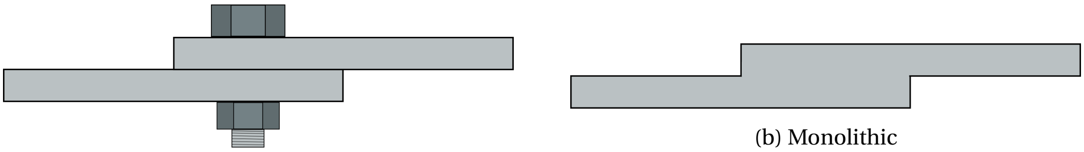

(a) Jointed

(b) Monolithic

Figure 2.1 – Lap-joint and its corresponding monolithic

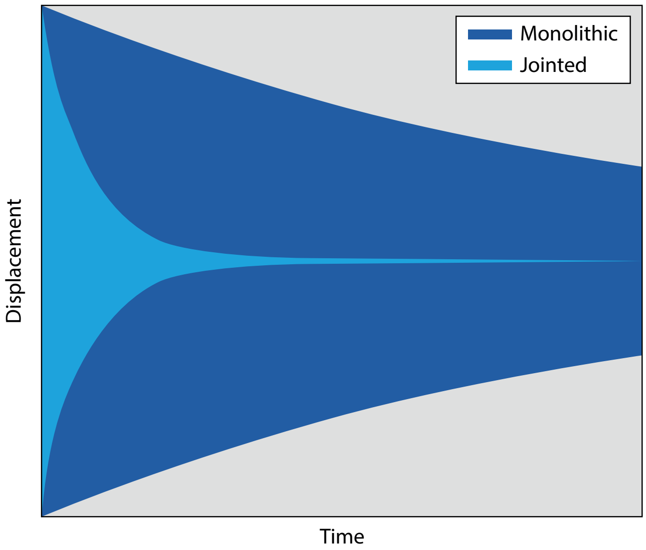

Figure 2.2 – Example of impact response difference between a bolted structure and a monolithic one

If we consider a linear system with viscous damping excited with an harmonic force:

$$m\ddot{x} + c\dot{x} + kx = F_0 \sin(\omega t + \phi) \tag{2.2}$$

the dissipated energy per cycle can be written as

$$D = \pi c \Omega A^2 \tag{2.3}$$

where Ω is the oscillation frequency. Therefore the dissipated energy per cycle is proportional to the oscillation frequency and to the square of the displacement amplitude. In the case of a constant frequency, the power-law coefficient can determined as $\delta = 2$.
If we now consider jointed structures, experiments have found a slope δ between 2.2 and 2.8 [44, 9]. An illustrative example is provided in fig. 2.3, where it can also be observed that in theory, for low force amplitudes, the behavior of the bolted structure is the same as the monolith. The reason for this is that, for very low amplitudes, the contact interface is not excited enough to provide a friction damping. An important aspect to take into account is that the power-law behavior is valid only for a force amplitude lower than the maximum friction force for which the contacting surfaces of the bolted joints would totally slip — more details on that later. The difference in dissipated energy observed between the linear system and the bolted structures indicates that the latter are characterized by a nonlinear behavior. This requires us to understand the physical reasons behind it, in order to proceed in its analysis.
In the next sections, the important concept of bolt preload will be introduced and the role of friction in bolted joints will be discussed.

2.1.2 Bolt preload

The tricky part of having to deal with bolted joints is that even the most trivial operation can hide great uncertainty. This is the case for the bolt preload. Let's consider a typical lap-joint, composed of two plates linked together by a bolt and a nut (see fig. 2.1a). A tightening torque T is applied to the nut while the bolt is kept still, which generates a certain traction force P in the bolt, called *preload*. In this way, the plates are pressed together and the integrity of the joint is

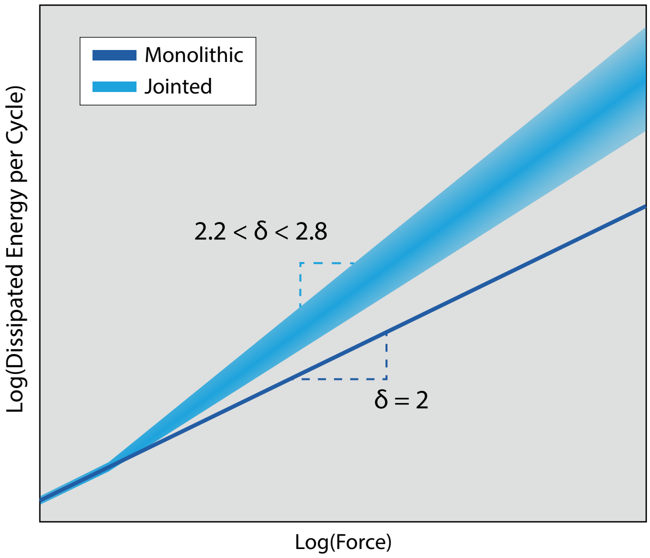

Figure 2.3 – Difference of dissipated energy between a bolted structure and a monolithic one

guaranteed. The desired preload force P is determined from the proof load F_p defined as:

$$F_p = A_t S_p \tag{2.4}$$

where A_t is the bolt tensile-stress area and S_p is the proof strength of the bolt material. The preload P is usually calculated as the 75% of the proof load F_p for non-permanent connections and 90% for permanent fasteners [10]. Once determined the preload value, the challenge is to relate it to the tightening torque to apply. The fundamental difficulty encountered in this task is to evaluate the friction forces exerted between nut and bolt threads, and between the nut and the plate surface. There are two ways of calculating the relationship between the tightening torque and the preload. On the one hand, the relationship can be calculated analytically using the physical properties of the joint, according to Motosh [33] expression:

$$T = P\left(\frac{p}{2\pi} + \frac{\mu_t r_t}{\cos\beta} + \mu_n r_n\right) \tag{2.5}$$

where:

- p is the thread pitch;
- μ_t is the friction coefficient between nut and bolt threads;
- μ_n is the friction coefficient between the face of the nut and the upper surface of the joint plate;
- r_t is the effective contact radius of the threads;
- r_n is the effective contact radius between nut and joint surface;
- β is the threads half-angle.

On the other hand, the relationship can be calculated empirically using the following short-form equation:

$$T = KPD \tag{2.6}$$

where D is the nominal diameter and K is a dimensionless constant called *nut factor*. The latter is experimentally determined and can be found in tables, according to the type of joint, materials and lubrication conditions [5].
It's easy to see from eqs. 2.5-2.6 that a slight error in the choice of parameters can lead to substantial errors in the determination of the tightening torque. Furthermore, there is a set of other aspects to take into account to choose the correct tightening torque, and each one of them adds uncertainty to the final **real** preload value:

- Tools for torque control: depending on the type of wrench chosen for the job, the accuracy on the measured torque can vary between ±2% and ±20%
- Short-term or embedment relaxation: in the minutes following the bolt tightening, preload decreases as much as 10% or 20%
- Long-term relaxation: in the days following the bolt tightening, preload can still decrease up to 10%
- Dynamic phase relaxation: under dynamic excitation, preload can decrease up to 10%. If the necessary measures are not taken against untightening, vibrations can lead to the full loss of tightening torque.
- Multiple bolts tightening: the interactions between different bolts tightened at different times can modify their initial preload. It's extremely important to define a correct tightening routine when dealing with multiple joints.
- Lubricants: their use normally increases preload accuracy, but the dynamic behavior will be affected.
- Operator: where there is human interaction there is error.

Let's notice that from the factors listed above have been removed all the ones related to bad design and faulty components. By considering all the factors, it's easy to understand how complicated is it to accurately determine and apply the preload. This is also a crucial aspect for the determination of dynamic properties of bolted structures, since the real preload determines the contact properties at the joint interfaces.
Once defined the preload and relative tightening torque, it's time to understand what happens at the joint level once the torque has been applied. This will come in handy later to understand the energy dissipation mechanism. In fig. 2.4 is shown a FEM simulation of a preload applied on a simple lap-joint. On the left the stress distribution in the bolt and plates cross-sections is visualized. A frustum shape can be recognized in the plates stress distribution: in bolted joints theory this zone is called Rotscher's cone [42], which is a property used to analytically calculate the joint member stiffness [25, 5, 10, 51, 29].

"If certainty you need in clamp, just make sure those bolts are damp."
J. H. Bickford

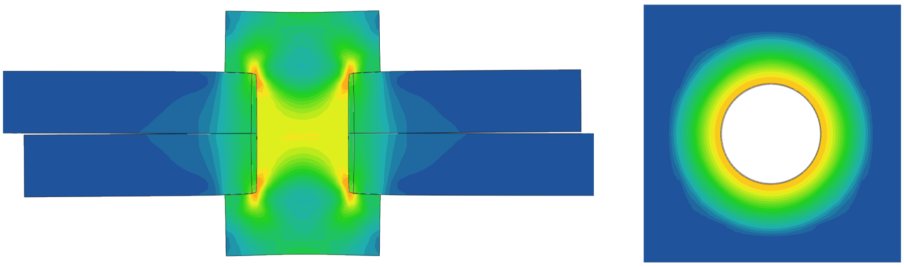

Figure 2.4 – FEM application of preload on a lap joint

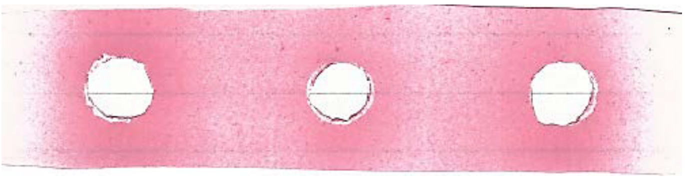

Figure 2.5 – Example of contact pressure measurement with pressure film. Stronger the color, higher the pressure.

On the right is shown the contact pressure distribution at the plates interface: the latter is maximum at the hole edge and it gradually decreases as the radius becomes larger. The radius for which the contact pressure tends to zero theoretically corresponds to the larger radius of the frustum. Experimentally, the contact pressure distribution can be measured thanks to pressure measurement films [3, 36, 1] inserted between the plates before preloading the joint: an example is shown in fig. 2.5.

2.1.3 It's all about friction

As we have seen in section 2.1.1, a jointed structure dissipates more energy than its corresponding monolithic version. This difference in dissipated energy is due to the friction that occurs between the surfaces in contact.

In order to understand the dissipation mechanism, the quasi-static behavior of a simple lap-joint subjected to an increasing traction force applied at the plates extremities will be considered. Fig. 2.6 shows the typical nonlinear force-displacement law. The contact surface is considered as the annular surface around the plates hole. Three phases can be distinguished:

1. **Micro-slip or Partial slip**: in this phase the annular surface can be divided in two different regions:

    - Stick zone, indicated by a dark blue dotted fill, where the contact pressure is higher enough to guarantee that there is no relative displacement between the plates.
    - Slip zone, indicated by a light blue dotted fill, where the tangential force **locally** overcomes the friction limit and a small displacement can take place in this region.

    At the beginning of the force application the stick zone corresponds to the full annular contact surface. As the force becomes larger, an annular slip region grows from the external radius of the contact surface to the inside, gradually replacing the stick region. In some of the literature ([44, 1]), the micro-slip term is reserved for the situation in which the slip region is much smaller than the total contact area, while the partial slip follows this phase. However, the boundaries between micro-slip and partial slip are not clearly defined.

2. **Macro-slip**: the tangential force has reached the friction force limit and the stick zone has been entirely replaced by the slip zone. At this point the force remains constant and a relative macro-displacement occurs between the plates.

3. **Pinning**: this last phase occurs when the displacement between the plates reaches the value of the bolt-hole clearance, which means that the bolt shank comes into contact with the hole wall. The force starts to grow again and a nonlinear bolt-hole contact stiffness is defined.

The evolution described here is a theoretical one. In reality, there are several practical difficulties that can be encountered performing these kind of tests and the curves obtained can

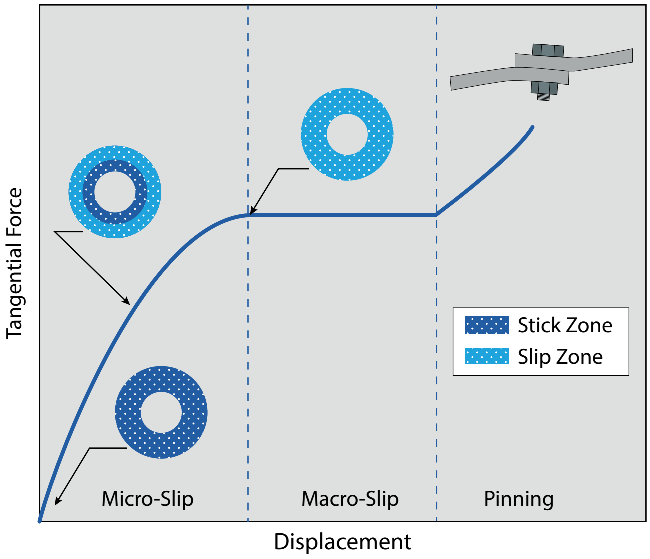

Figure 2.6 – Quasi-static traction loading of a lap-joint

be quite different from the theory. However, the friction energy dissipation mechanism is the same for all types of joints configurations: where there are two surfaces in contact, there can be friction.
Quasi-static load experiments on bolted joints performed by Sandia National Laboratories [1] have observed the curve described in this section. However, since we are interested in their dynamics, in the next section we will discuss the non-linearity generated by friction on modal parameters such as natural frequency and damping.

2.1.4 Dynamic properties of bolted joints

The effect of friction on dynamic properties of built-up structures is an on-going research topic [21, 22, 52, 32]. In fact, friction generates hysteretic effects and stick-slip behaviors, which are complex to model and identify. The goal of this section is to provide the *standard* modal behavior of a bolted structure, as a function of input force or displacement amplitude.
Now, bringing the comparison between a monolithic and a jointed structure to a *modal* level, it will be possible to understand the type of non-linearity affecting the single modes [39]. If the external input effectively excites the joints, the typical nonlinear behavior of the Frequency Response Function (FRF) will be similar to the one of fig. 2.7a. The FRF corresponding to the monolithic linear structure, indicated by the top-right arrow, doesn't depend on the input amplitude. Regarding the jointed structure, the FRFs obtained at increasing levels of input force generally follow the behavior that goes from the dark blue curve to the orange one.
When modal parameters are calculated, it's possible to generate the nonlinear curves for natural frequency and damping as a function of force or displacement amplitude, shown in figs. 2.7b, 2.7c — please note that the scale of their horizontal axes is logarithmic. By keeping in mind the quasi-static behavior previously described in fig. 2.6, it's important to notice that in this case the *pinning* phase is not considered.
Looking at the nonlinear frequency curve of fig. 2.7b, two clear *boundaries* can be distinguished:

- LOW amplitude: the natural frequency of the jointed structure tends to the one of the monolithic structure — or at least to the *linear* one.

- HIGH amplitude: the natural frequency of the jointed structure tends to what we can call

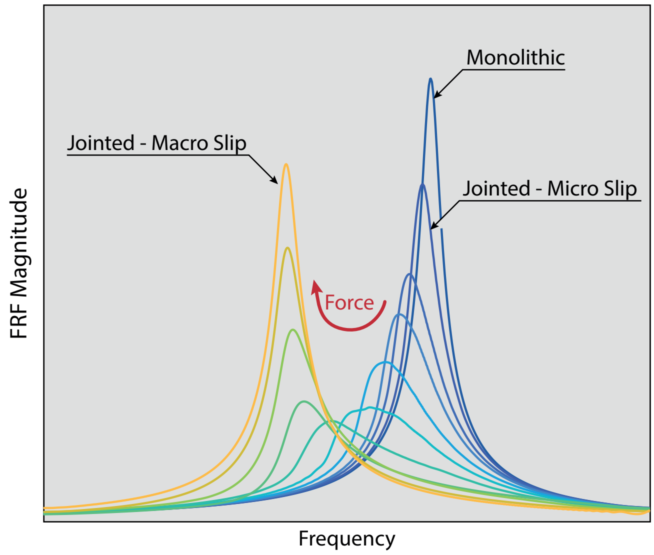

(a) FRF nonlinear behavior for an SDOF system with friction

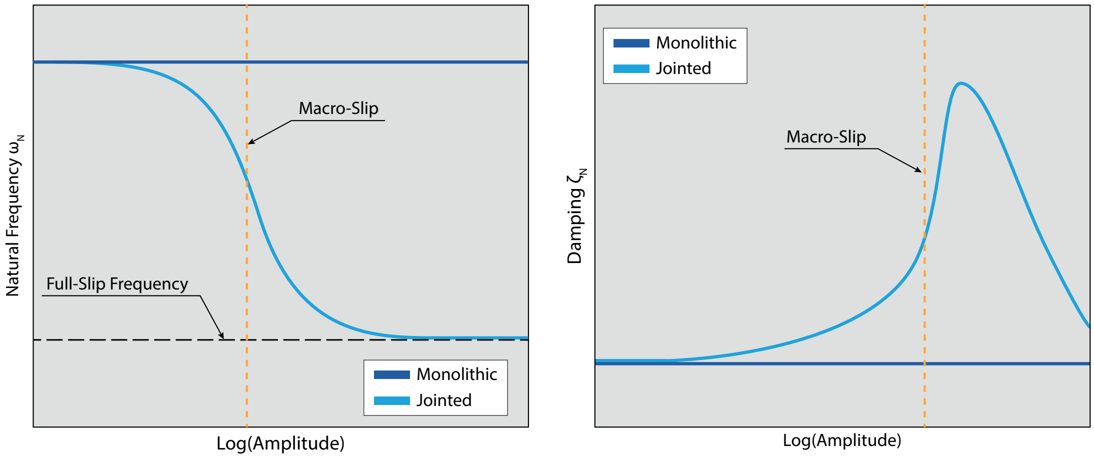

(b) Natural Frequency

(c) Damping Ratio

Figure 2.7 – Modal behavior comparison between monolithic and assembled structures

full-slip frequency, which is lower than the low amplitude *linear* one.

Therefore, the natural frequency shows a *softening* behavior, which means that it decreases with the amplitude of oscillation.

Moving our attention to the nonlinear evolution of the damping ratio, the first aspect that we notice is that there is a value of the amplitude for which the damping ratio is maximum. After its maximum value, the damping ratio tends to the linear value again. This is due to the fact that, in order to keep the macro-slip regime for higher displacements, the ratio between the energy to provide to the system and the dissipated one becomes higher. The damping ratio non-linearity is used, for example, in under-platform damper for turbine blades [43, 36], in order to optimize the energy dissipation and reduce the vibration amplitude, which is the main cause of blade failure. However, for the application in bolted joints, there are some other aspects to take into account. The most important one is the position of the macro-slip limit in the frequency and damping nonlinear curves. It can be observed that the macro-slip limit is placed quite before the maximum damping value. This means that, in order to maximize the damping in bolted joints, they would have to operate in the macro-slip regime. However, a joint operating in macro-slip will normally fail in its structural task. An idea could be to design a series of joints with a structural task and another series that instead have an energy dissipation task. Another factor to take into account is the pinning, which would provide an additional contact stiffness non-linearity—not shown here—in the macro-slip regime.

2.2 Friction Models for bolted structures

Friction plays a very important role in the dynamics of bolted structures. If we consider the equations of motion of a structure with friction nonlinearities we can write:

$$\mathrm{M}\ddot{x} + \mathrm{C}\dot{x} + \mathrm{K}x + \mathrm{F}_f(x, \dot{x}) = \mathrm{F}_e \tag{2.7}$$

where:

- M, C, and K are respectively the linear mass, viscous damping, and stiffness matrices;
- $\ddot{x}$, $\dot{x}$, and x are respectively the acceleration, velocity, and displacement vectors;
- F_e is the external excitation on the system;
- F_f is the vector of internal nonlinear forces due to friction, function of x and $\dot{x}$.

Through the years, many different friction models have been developed. They can usually be divided into two main categories: macro-models and constitutive models. Macro-models are based on empirical and experimental observations, while the constitutive ones are derived from the contact theory in order to physically describe the stress-strain relationship in the contact region. In addition, in macro-models it's possible to make a distinction between three categories: static, dynamic, and hysteretic [34, 22, 4]. Since the role of friction in bolted structures is crucial, in the next section will be provided examples of the most used friction modeling techniques, divided by categories.

2.2.1 Static friction models

Static models are the oldest and simplest approaches to describe friction. The assumption is that the force is a static function of the difference in velocity between the two surfaces in contact.

2.2.1.1 Coulomb

The most representative and iconic friction model of this category is the one developed by Coulomb in the 18th century. The method essentially defines the friction force F_f as a force that opposes to the motion and that can be written as:

$$\mathrm{F}_f = \mu \mathrm{N} \frac{v}{|v|} \tag{2.8}$$

where μ is the friction coefficient, N is the normal force pressing the body surfaces together, and v is the relative velocity between the two surfaces. It's also possible to define the friction limit force $\mathrm{F}_c = \mu\mathrm{N}$. The curve relative to this simple law is shown in fig. 2.8a. Modifications can be applied to this model. For example, it's possible to consider an additional viscous force coefficient F_v, for which the total friction force becomes:

$$\mathrm{F}_f = \mu \mathrm{N} \frac{v}{|v|} + \mathrm{F}_v v \tag{2.9}$$

The name of Coulomb is one of the 72 names carved into the Eiffel tower.

This law is represented in fig. 2.8b. Experiments have shown that the normal force N and the friction coefficient μ depend on the velocity. In particular, it is known that the friction coefficient, when the slip velocity $|v| = 0$, is higher than the friction coefficient when $|v| \neq 0$ [40]. In the first case we refer to the static friction coefficient μ_s, while in the second case we refer to the dynamic friction coefficient μ_d. This behavior is called stiction, which is short for *static friction*, and it's possible to define the stiction force $F_s = \mu_s N$. The relative curve for the Coulomb model with stiction can be observed in fig. 2.8c.

2.2.1.2 Stribeck

In his experiments on roller bearings, Stribeck [48] observed that, after reaching the stiction force F_s, the friction force is not discontinuous, but it has a continuous behavior that can be expressed by the following nonlinear law:

$$F_f = \left[F_c + (F_s - F_c)e^{-(v/v_s)^{\delta_s}}\right]\frac{v}{|v|} + F_v v \tag{2.10}$$

where v_s is a parameter called *Stribeck velocity* that can be identified from experiments. An example of curve described by eq. 2.10 it's shown in fig. 2.8d. Sometimes the curve can be asymmetrical.

Other successful static friction models that have been developed can be found in the works of Karnopp [28] and Armstrong [2].

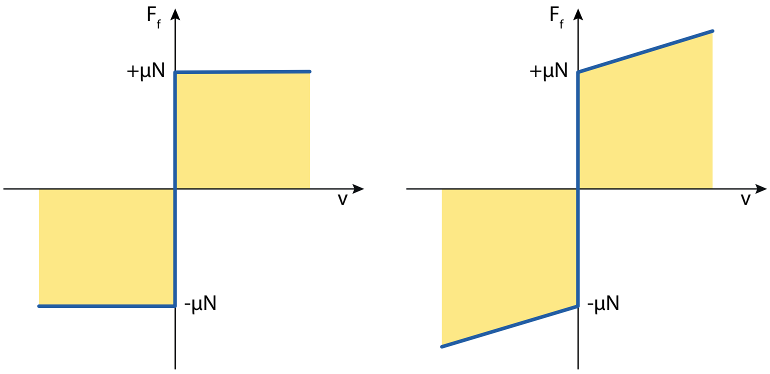

(a) Coulomb

(b) Viscous Coulomb

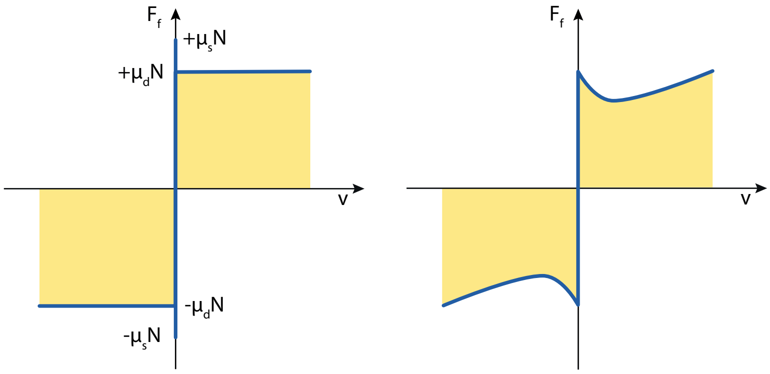

(c) Coulomb with stiction

(d) Stribeck

Figure 2.8 – Static friction models

2.2.2 Dynamic friction models

Dynamic friction models are particularly used in the field of control engineering in order to compensate for the effect of friction in mechanical system, with the goal of designing high-precision servo mechanisms. These models are based on the introduction of internal state variables that can vary in time and they lead to differential equations describing the friction behavior.

2.2.2.1 Dahl

Dahl friction model [16] was introduced in 1968 to study the rolling friction in ball bearings. Dahl's main idea was to use the materials stress-strain curve of classical solid mechanics in order to model friction. Considering T to be the friction force and $T_c = \mu N$ its critical value according to Coulomb's law, Dahl's model general form can be written as:

$$\frac{dT}{dx} = \sigma \left[1 - \frac{T}{T_c} \frac{\dot{x}}{|\dot{x}|} \right]^{\alpha} \tag{2.11}$$

where σ is the stiffness, which represents the slope of the curve at $T = 0$, and α is a parameter that determines the shape of the curve and it's usually taken as $\alpha = 1$ for simplicity.

It's possible to see that in this model the friction force is only function of the displacement x and of the sign of the velocity $\dot{x}$. However, in the general form of eq. 2.11 the friction force T is expressed as a derivative in the displacement x. By dividing both sides of the equation by dt, is possible to obtain an expression that is more useful for time integration:

$$\dot{T} = \sigma \dot{x} \left[1 - \frac{T}{T_c} \frac{\dot{x}}{|\dot{x}|} \right]^{\alpha} \tag{2.12}$$

In fig. 2.9 are shown examples of Dahl hysteresis cycles obtained by imposing a cyclic displacement of amplitude x_{max} for different values of the parameter α. For $\alpha \geq 1$, there are no problems of existence for the term between parentheses of eq. 2.12. However, for $0 < \alpha < 1$, in the event that the term inside the parentheses becomes negative throughout the cycle, the value of the force T is imposed to be the friction limit force T_c.

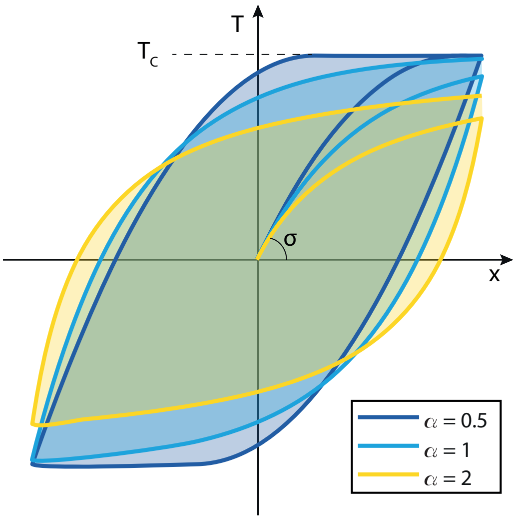

Figure 2.9 – Example of Dahl cycles for different values of the parameter α

2.2.2.2 Valanis

The Valanis model [50] was initially developed to deal with elasto-plastic materials under cycling loading. Then, more in the interest of this work, it has been successfully applied to jointed structures and contact interfaces [21, 36]. The Valanis model is described by the followin non-linear first-order equation:

$$\dot{T} = \frac{E_0 \dot{x}\left[1 + \frac{\lambda}{E_0}\frac{\dot{x}}{|\dot{x}|}(E_t x - T)\right]}{1 + \kappa\frac{\lambda}{E_0}|\dot{x}|(E_t x - T)} \tag{2.13}$$

with:

$$\lambda = \frac{E_0}{\mu N\left(1 - \kappa\frac{\lambda}{E_0}\right)} \tag{2.14}$$

With the help of fig. 2.10, obtained with eq. 2.13 by imposing a cyclic displacement of amplitude x_{max}, it's possible to distinguish the different parameters composing the Valanis model:

- E_0: Stick stiffness. This is the initial stiffness at full stick conditions;
- E_t: Slip stiffness. This is the stiffness at full slip conditions. In fact, experiments on lap-joints observed that, during the macro-slip phase, the force is not constant and equal to the limit friction force but it's characterized by a certain stiffness [21]. The latter can also be easily implemented for the Dahl model by considering an additional stiffness in parallel.
- κ: Micro to macro-slip transition coefficient ($0 < \kappa < 1$). For low values the transition between micro-slip and macro-slip is more gradual. A comparison between two values of κ is shown in fig. 2.10.

With its small set of parameters and its simple implementation in dynamic systems, the Valanis model is a truly versatile tool for the modeling of friction in bolted structures.

Obviously, Dahl and Valanis are not the only dynamics models, but they are the most relevant

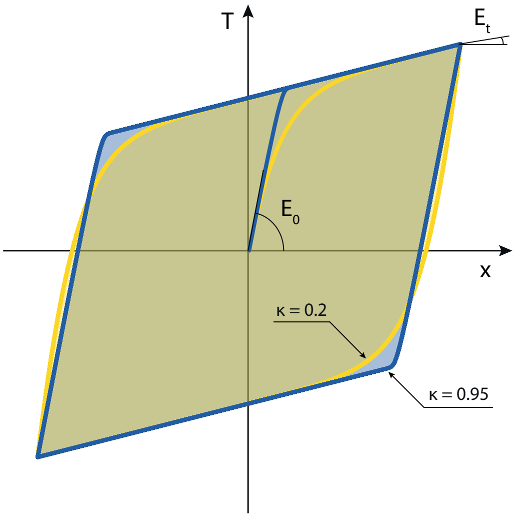

Figure 2.10 – Example of Valanis cycle with its parameters

in the context of bolted structures and in the interest of this work. Most of the other dynamic friction models are extensions of the Dahl's one, in order to overcome its limits. In fact, a drawback of Dahl model is the fact that it's unable to describe the stiction phenomenon. The model developed by Bliman and Sorine [6, 8, 7] and the LuGre model [17] try to reproduce the stiction behavior. In particular, the LuGre model is based on the bristle model of Haessig and Friedland [24], in which each point of contact at the interface is treated as a bond between flexible bristles. In addition, the LuGre model can also be used for lubricated contact.

The name LuGre derives from the collaboration between Lund and Grenoble universities.

2.2.3 Hysteretic friction models

Hysteretic models originate from the theory of elasticity and they derive from the effort of describing the energy dissipation and deformation mechanism in materials. In the previous section we have seen that for dynamic friction model, a differential equation is sufficient to fully describe the friction hysteresis behavior. Concerning the hysteretic friction models — but also constitutive models later — each phase of the cycle will have to be treated separately. The three different phases characterizing an hysteresis cycle are illustrated in fig. 2.11: they are referred to as *loading*, *unloading*, and *reloading*. The transition between the different phases occurs when the sign of the relative velocity $\dot{\delta}$ changes.

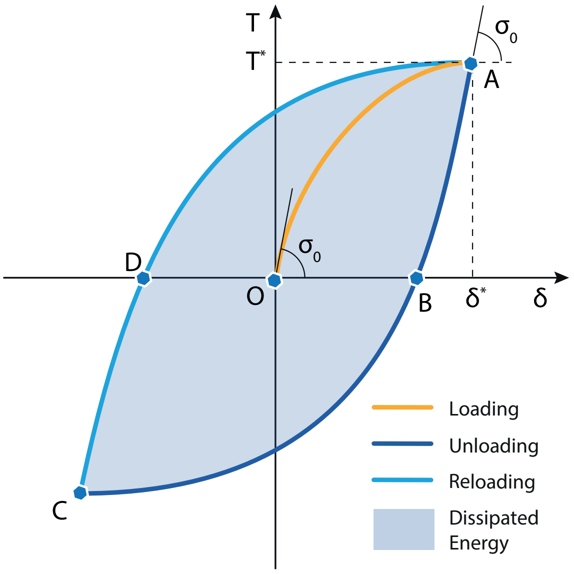

Figure 2.11 – General hysteresis cycle and its phases

2.2.3.1 Masing

Masing models [11] are simple tools used to describe the hysteretic behavior of many systems. The model was firstly introduced to model the Bauschinger effect in materials (see [46]), which is a reduction in compression strength after a plastic deformation in tension.

Masing was the first to create a model for elasto-plastic material during cycle loading. His theory also provides for the so called Masing rule or hypothesis, which states that an hysteresis path during steady-state cycle loading can be obtained from the monotonic initial loading, also called *backbone* curve, with an expansion factor of two.

By keeping the notation shown in Fig. 2.11 the mathematical representation of Masing rule is the following:

$$\delta_1(T) = \delta^* - 2\sigma_0\left(\frac{T^* - T}{2}\right) \tag{2.15}$$

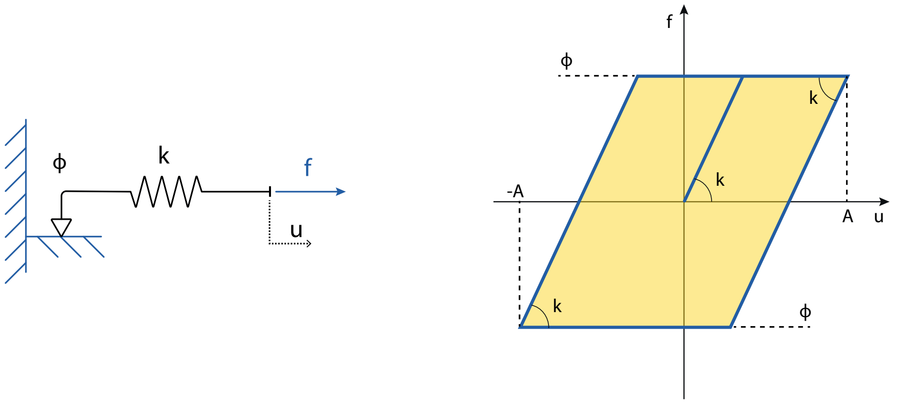

(a) Jenkins Element (b) Jenkins Cycle

Figure 2.12 – Jenkins element and its steady state hysteresis cycle

where δ^* represents the maximum tangential displacement amplitude reached in the last cycle and σ_0 is the function describing the relative displacement in the loading phase.

A practical consequence of this rule, which is also a material property during cycle loading, is that the slope right after the load inversion has the same value of the initial slope during the monotonic initial loading phase.

It's important to clarify that the original Masing hypothesis is only valid for steady-state cycles or loading between fixed limits. The simplest example of Masing model is represented by the Masing or Jenkins element, consisting of a spring with stiffness k, in series with a slider of maximum allowable force, or *yield force* ϕ. The element is represented in fig. 2.12a. When the force reaches the yield force value, the slider starts to slip. The equations related to a steady state cycle of amplitude A applied to this element are divided in three different phases, and the element force f can be written as:

$$\textbf{Initial loading:} \quad \begin{cases} f = ku & ; \quad \dot{u} > 0 \quad ; \quad 0 \le u < \phi/k \\ f = \phi & ; \quad \dot{u} > 0 \quad ; \quad u \ge \phi/k \end{cases} \tag{2.16}$$

$$\textbf{Unloading:} \quad \begin{cases} f = k(u - \mathrm{A}) + \phi & ; \quad \dot{u} < 0 \quad ; \quad \mathrm{A} - 2\phi/k \le u < \mathrm{A} \\ f = -\phi & ; \quad \dot{u} < 0 \quad ; \quad u \le \mathrm{A} - 2\phi/k \end{cases} \tag{2.17}$$

$$\textbf{Reloading:} \quad \begin{cases} f = k(u + \mathrm{A}) - \phi & ; \quad \dot{u} > 0 \quad ; \quad -\mathrm{A} \le u < -\mathrm{A} + 2\phi/k \\ f = \phi & ; \quad \dot{u} > 0 \quad ; \quad u \ge -\mathrm{A} + 2\phi/k \end{cases} \tag{2.18}$$

However, a single Jenkins element can't really describe the complexity of friction phenomena. Therefore, the use of particular distributions of several Jenkins elements have been developed and it has led to the formulation of the Iwan model, treated in the next section.

2.2.3.2 Iwan

In 1966, Iwan [26] developed a model to reproduce the hysteresis behavior observed in materials and structures. The model consists of N Jenkins elements in parallel, with the same stiffness k, and arranged in order of increasing yield force, as shown in fig. 2.13. Each element follows the behavior described in eqs. 2.16-2.18, and the total force F exerted by the model is the sum of all the single contributions f_i. If the *initial loading* is considered, the single elements contributions can be divided into two categories:

1. Yielded: the n elements for which $u \geq \phi_i / k$ and therefore the slider is slipping. Their total contribution F_y can be expressed as:

$$F_y = \sum_{i=1}^{n} \phi_i / N \tag{2.19}$$

2. Non-Yielded: the $N - n$ elements which are not slipping yet. Their total contribution F_{ny} is:

$$F_{ny} = ku(N - n)/N \tag{2.20}$$

The total Iwan force F can therefore be written as:

$$F = F_y + F_n y = \sum_{i=1}^{n} \phi_i / N + ku(N - n)/N \tag{2.21}$$

that, in case the number of Jenkins elements N becomes very high, can be written in its integral form as:

$$F = \int_0^{ku} \phi\rho(\phi) d\phi + ku \int_{ku}^{\infty} \rho(\phi) d\phi \tag{2.22}$$

where $\rho(\phi)$ represents the distribution of the yield forces values and $\rho(\phi)d\phi$ indicates the part of the total elements having $\phi \leq \phi_i \leq \phi + d\phi$.
The situation is slightly more complicated in the *unloading* phase, where the load is reversed. In fact, here the categories of elements become three:

1. Yielded—Yielded: elements that were positively yielded in the previous phase and they are now negatively yielded.
2. Yielded—Non-Yielded: elements that were positively yielded in the previous phase and that are now not negatively yielded.
3. Non-Yielded—Non-Yielded: elements that were not yielded in the previous phase and that are still not yielded now.

The total force for the *unloading* phase therefore becomes:

$$F = \int_0^{\frac{k(A-u)}{2}} -\phi\rho(\phi) d\phi + \int_{\frac{k(A-u)}{2}}^{kA} [k(u - A) + \phi]\rho(\phi) d\phi + ku \int_{kA}^{\infty} \rho(\phi) d\phi; \quad \dot{u} < 0; \quad -A \leq u \leq A \tag{2.23}$$

Finally, the total force for the *reloading phase* can be obtained as:

$$F = \int_0^{\frac{k(A+u)}{2}} \phi\rho(\phi) d\phi + \int_{\frac{k(A+u)}{2}}^{kA} [k(u+A) - \phi]\rho(\phi) d\phi + ku \int_{kA}^{\infty} \rho(\phi) d\phi; \quad \dot{u} > 0; \quad -A \leq u \leq A \tag{2.24}$$

It can be observed that the most important parameter for this kind of models is the distribution function $\rho(\phi)$ of the Jenkins elements limit friction force. Iwan [26] considered the distribution function to be a band-limited function centered about a chosen value ϕ_s, with a width $\Delta\phi$ and an area equal to unity. The distribution is shown in fig. 2.14a.
Almost 50 years later, Segalman [44, 45] decided to adapt an Iwan model to reproduce the dy-

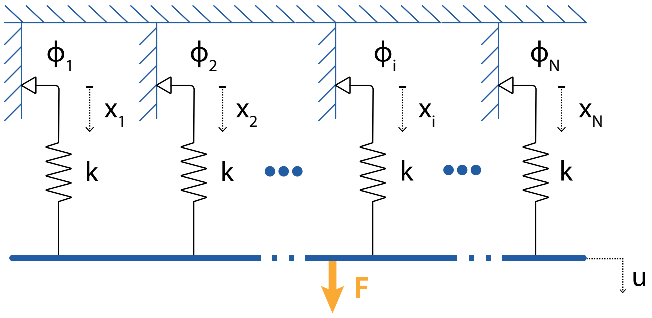

Figure 2.13 – Iwan Element

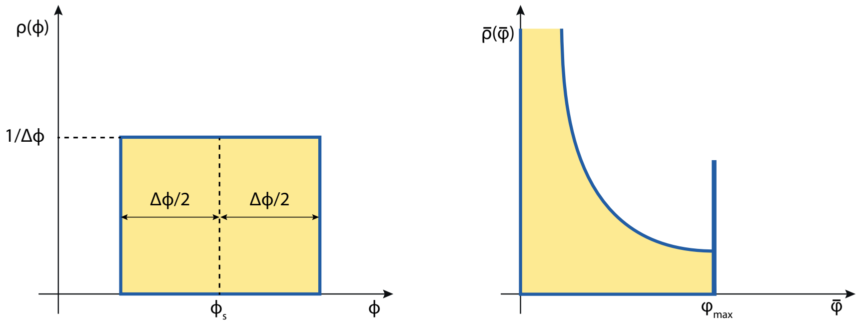

(a) Iwan distribution

(b) Segalman distribution

Figure 2.14 – Jenkins elements friction limit distribution according to Iwan and Segalman

namics of bolted joints. The result of this process is the *Four-Parameter Iwan Model*, which is an Iwan model with a particular elements distribution and that can be identified by only four parameters. Let's see how it can be obtained.
The model is built exactly like the original Iwan model, but in this case, in addition to the global displacement $u(t)$, also the singular slider displacements $x(t,\phi_i)$ is considered, which is a function of time and of the friction force limit of the single slider. In this way, the restoring force can be expressed in the integral form:

$$\mathrm{F}(t) = \int_0^\infty \rho(\phi)k[u(t) - x(t,\phi_i)]d\phi \tag{2.25}$$

with the slider displacement that evolves from the imposed displacement $u(t)$ as:

$$\dot{x}(t,\phi) = \begin{cases} \dot{u} & \text{if} \quad \left\| u - x(t,\phi) \right\| = \phi/k \quad \text{and} \quad \dot{u}\left(u - x(t,\phi)\right) > 0 \\ 0 & \text{otherwise} \end{cases} \tag{2.26}$$

Segalman then removed the parameter k by making a change of variables:

$$\bar{\phi} = \phi/k \ \ [m] \quad ; \quad \bar{\rho}(\bar{\phi}) = k^2\bar{\rho}(k\phi) \ \ [\mathrm{N}/m^2] \quad ; \quad \bar{x}(t,\phi) = x(t,k\phi) \ \ [m] \tag{2.27}$$

Eqs. 2.25-2.26 therefore become:

$$\mathrm{F}(t) = \int_0^\infty \bar{\rho}(\bar{\phi})[u(t) - \bar{x}(t,\bar{\phi}_i)]d\bar{\phi} \tag{2.28}$$

with the slider displacement that evolves from the imposed displacement $u(t)$ as:

$$\dot{\bar{x}}(t,\bar{\phi}) = \begin{cases} \dot{u} & \text{if} \quad \left\| u - \bar{x}(t,\bar{\phi}) \right\| = \bar{\phi} \quad \text{and} \quad \dot{u}\left(u - \bar{x}(t,\bar{\phi})\right) > 0 \\ 0 & \text{otherwise} \end{cases} \tag{2.29}$$

From eqs.2.28 it's possible to define two properties from two limit situations. The first is when all the slider displacements are null. In this case the initial stiffness or stick stiffness K_T can be defined as:

$$K_T = \int_0^\infty \bar{\rho}(\bar{\phi}) d\bar{\phi} \quad \text{when} \quad \bar{x}(t,\bar{\phi}_i) = 0 \quad \forall i \quad \text{and} \quad t = 0 \tag{2.30}$$

The second is when all the slider are slipping. Here the total macro-slip force F_S can be obtained:

$$F_S = \int_0^\infty \bar{\phi}\bar{\rho}(\bar{\phi}) d\bar{\phi} \quad \text{when} \quad u(t) - \bar{x}(t,\bar{\phi}_i) = \bar{\phi} \quad \forall i \tag{2.31}$$

As said previously, the distinguishing feature of the Segalman model is the distribution function $\bar{\rho}(\bar{\phi})$. The latter is shown in fig. 2.14b and it consists of a power-law terminated by a Dirac delta that can be expressed as:

$$\bar{\rho}(\bar{\phi}) = R\bar{\phi}^\chi \left[H(\bar{\phi}) - H(\bar{\phi} - \bar{\phi}_{max}\right] + S\delta(\bar{\phi} - \bar{\phi}_{max}) \tag{2.32}$$

where H is the Heaviside function, $\bar{\phi}_{max}$ corresponds to the global displacement u_S when the force reaches the total macro-slip value F_S, S is the coefficient of the Dirac function, and χ defines the power-law coefficient.
The *original* four-parameter Iwan model is represented by the set $\{\chi, \bar{\phi}_{max}, R, S\}$. However, their physical meaning is not very clear, and a set of more representative parameters is needed. A new set of parameters, and their relations with the original ones are therefore obtained by Segalman. The new set of parameters includes:

- χ: the power law coefficient of the energy dissipation.
- β: the transition behavior coefficient between micro and macro-slip. Its relation with the original parameters is the following:

$$\beta = \frac{S(\chi+1)}{R\bar{\phi}_{max}^{\chi+1}} \tag{2.33}$$

- F_s: the macro-slip friction force. It can be obtained from eq. 2.31 as:

$$F_S = \bar{\phi}_{max} \left(\frac{R\bar{\phi}_{max}^{\chi+1}}{\chi+1} \right) \left(\frac{\chi+1}{\chi+2} + \beta \right) \tag{2.34}$$

- K_T: the interface stick stiffness, which can be obtained from eq. 2.30 as:

$$K_T = \frac{R\bar{\phi}_{max}^{\chi+1}(\beta+1)}{\chi+1} \tag{2.35}$$

The new set of parameter χ, β, F_S, K_T allows for an easier parameter identification procedure and the original set of parameters can be derived from them.

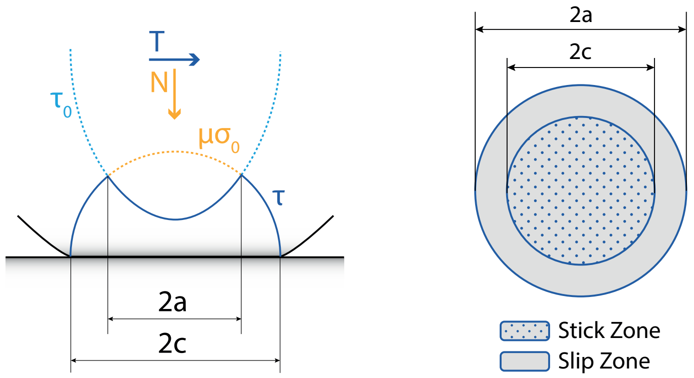

(a) Stress distribution

(b) Contact area

Figure 2.15 – Contact between a plane and a sphere pressed on each other with a normal force N and with sphere subjected to tangential force T

Finally, it's possible to calculate the dissipated energy per cycle D for a steady state cycle of amplitude $u_0 \leq \bar{\phi}_{max}$ as:

$$\mathrm{D} = \int_0^{u_0} 4\left[u_0 - \bar{x}(t,\bar{\phi})\right]\bar{\phi}\bar{\rho}(\bar{\phi})\,d\bar{\phi} \tag{2.36}$$

$$= r^{\chi+3}\frac{4\mathrm{F_S}\bar{\phi}_{max}(\chi+1)}{\left(\beta+\dfrac{\chi+1}{\chi+2}\right)(\chi+2)(\chi+3)} \tag{2.37}$$

with $r = u_0/\bar{\phi}_{max}$.

From eq. 2.37 it's possible to see that the power-law coefficient for the micro-slip phase is represented by $\chi+3$. As we have seen in section 2.1.1, this represents the slope of the log-log curve of the dissipated energy per cycle as a function of displacement. Since it has been experimentally observed that the slope is usually between 2 and 3 for bolted structures, the value of χ will be $-1 \leq \chi \leq 0$.

2.2.4 Constitutive friction models

Constitutive models develop a stress-strain relationship for the contact, that can then be implemented in high-detail FEM simulations. In the following paragraphs the constitutive model derived from Hertz normal contact and Mindlin tangential contact theories will be described. Alternatives of this method exploit the representation of a contact surface through fractals [31, 14] and one of the more successful method is the Weierstrass-Mandelbrot model [30].

Going back to Hertz and Mindlin, Cattaneo [12, 13] studied the problem of the elastic contact between two bodies pressed on each other by a constant normal force $\mathrm{N_0}$, with a tangential load T monotonically growing from zero to a maximum value T^*. Mindlin extended the model for a general oscillatory force of amplitude $\pm\mathrm{T}^*$ and considered the contact between a sphere and a plane (see [27]).

From Hertz theory the radius a of the contact area is defined as:

$$a = \sqrt[3]{\frac{3}{4}\frac{\mathrm{N_0}\rho}{\mathrm{E}^*}} \tag{2.38}$$

where

$$\frac{1}{E^*} = \frac{1-\nu_1^2}{E_1} + \frac{1-\nu_2^2}{E_2} \tag{2.39}$$

and the generalized bending radius ρ is defined as:

$$\frac{1}{\rho} = \frac{1}{R_1} + \frac{1}{R_2} \tag{2.40}$$

being E_1, E_2 the Young moduli; ν_1^2, ν_2^2 the squares of the Poisson ratios and R_1, R_2 the bending radii of the two surfaces in contact.

In order to describe the friction behavior at the contact surface, both Cattaneo and Mindlin used the Coulomb's law. Considering μ the friction coefficient, if the tangential load T reaches the critical value

$$T_c = \mu N_0 \tag{2.41}$$

the two surfaces starts to slide relatively to each other entering in what is usually called the sliding or macro-slip phase, during which the tangential load T will remain constant.

During the monotonic tangential loading phase, Mindlin and Cattaneo demonstrated that the contact area is divided into two parts: a stick zone and a slip zone. The stick zone is a circle of radius c, while the slip zone is the annulus of internal radius c and external radius a. In Fig. 2.15b is possible to see the two regions, while in Fig. 2.15a are shown the normal and tangential stress distribution at the contact interface.

The relationship between the stick zone radius c and the contact radius a was found by Cattaneo to be:

$$\frac{c}{a} = \left(1 - \frac{T}{\mu N_0}\right)^{1/3} \tag{2.42}$$

It's easy to see that, when the tangential load T increases, the stick region becomes smaller, until $T = T_c$, when $c = 0$ and the macro-slip phase takes place. If we consider A_c as the contact area of radius a and A_s as the slip annular area of internal radius c and external radius a, some researchers prefer to divide this phase into a micro-slip phase, where $A_s << A_c$ and a partial slip phase, where $A_s < A_c$.

We now consider an oscillating loading cycle of amplitude $\pm T^*$. The hysteresis cycle has the shape of the one shown in Fig. 2.11, with the tangential displacement δ on the x-axis and the tangential force T on the y-axis.

According to Mindlin model in [27], it's possible to write the tangential displacement δ as a function of the applied tangential force T. During the initial loading the tangential displacement δ_0 can be written as:

$$\delta_0 = \frac{3\mu N_0 G^*}{16a}\left[1 - \left(1 - \frac{T}{\mu N_0}\right)^{2/3}\right] \tag{2.43}$$

where

$$G^* = \frac{2-\nu_1}{G_1} + \frac{2-\nu_2}{G_2} \tag{2.44}$$

in which G_1 and G_2 are the shear moduli of the materials in contact. During the unloading and reloading phases, the respective tangential displacements δ_1 and δ_2 can be written as:

$$\delta_1 = \frac{3\mu N_0 G^*}{16a}\left[2\left(1-\frac{T^*-T}{2\mu N_0}\right)^{2/3}-\left(1-\frac{T^*}{\mu N_0}\right)^{2/3}-1\right] \qquad \text{Unloading} \qquad (2.45)$$

$$\delta_2 = -\frac{3\mu N_0 G^*}{16a}\left[2\left(1-\frac{T^*+T}{2\mu N_0}\right)^{2/3}-\left(1-\frac{T^*}{\mu N_0}\right)^{2/3}-1\right] \qquad \text{Reloading} \qquad (2.46)$$

It's important to point out that, if the tangential force T reaches the critical value $T_c = \mu N_0$, according to Coulomb's friction model, it will remain constant until the load changes direction.

2.2.5 A relation between Dahl and Mindlin

In the previous sections we have described friction models belonging to different categories. Each of these categories carries its advantages and disadvantages. For example, dynamic models can describe the hysteresis cycle with a differential equation, which makes them suitable for dynamic simulations. However, considering the Dahl model, it can be demonstrated that it doesn't satisfy the Masing rule. Other types of models, such as the hysteretic and constitutive ones, try to reproduce the physical behavior at the contact interface. In this case, it can be demonstrated that the Iwan and Mindlin models satisfy the Masing rule.

The question we want to answer in this section is: can we find a link between a dynamic model and a constitutive one?

In particular, a correlation between Dahl dynamic model and the constitutive Mindlin one will be found. This section is part of the journal article [38] published by the author.

Let's start by considering the Mindlin model described in section 2.2.4. The first step is to find the expression of the tangential force T as a function of the displacement δ from eqs. 2.43,2.45,2.46. The equations of the tangential force T during the different phases of the hysteresis cycle can then be written as:

$$T_0 = \mu N_0\left[1-\left(1-\frac{16a}{3\mu N_0 G^*}\delta_0\right)^{3/2}\right] \qquad (2.47)$$

$$T_1 = T^* - 2\mu N_0\left[1-\left[\frac{1}{2}\left(\frac{16a}{3\mu N_0 G^*}\delta+\left(1-\frac{T^*}{\mu N_0}\right)^{2/3}+1\right)\right]^{3/2}\right] \qquad (2.48)$$

$$T_2 = -T^* + 2\mu N_0\left[1-\left[\frac{1}{2}\left(\frac{16a}{3\mu N_0 G^*}\delta+\left(1-\frac{T^*}{\mu N_0}\right)^{2/3}+1\right)\right]^{3/2}\right] \qquad (2.49)$$

At this point the derivatives of Eqs.2.47-2.49 with respect to the variable δ are found as:

$$\frac{dT_0}{d\delta_0} = \frac{8a}{G^*}\left(1-\frac{16a}{3\mu N_0 G^*}\delta\right)^{1/2} \qquad (2.50)$$

$$\frac{dT_1}{d\delta} = \frac{8a}{\sqrt{2}G^*}\left[1+\frac{16a}{3\mu N_0 G^*}\delta+\left(1-\frac{T^*}{\mu N_0}\right)^{2/3}\right]^{1/2} \qquad (2.51)$$

$$\frac{dT_2}{d\delta} = \frac{8a}{\sqrt{2}G^*}\left[1-\frac{16a}{3\mu N_0 G^*}\delta+\left(1-\frac{T^*}{\mu N_0}\right)^{2/3}\right]^{1/2} \qquad (2.52)$$

Finally Eqs.2.43,2.45,2.46 are replaced respectively in Eqs.2.50-2.52, obtaining:

$$\frac{dT}{d\delta_0} = \frac{8a}{G^*}\left(1 - \frac{T}{T_c}\right)^{1/3} \qquad \text{Phase 0} \tag{2.53}$$

$$\frac{dT}{d\delta} = \frac{8a}{G^*}\left(1 - \frac{T^* + T sign(\dot{\delta})}{2T_c}\right)^{1/3} \qquad \text{Phases 1 \& 2} \tag{2.54}$$

If we analyze these last two equations, it's possible to see that they are equivalent to the original Dahl friction model of Eq.2.11 with the two parameters σ and α chosen as:

$$\sigma = \frac{8a}{G^*} \qquad \alpha = \frac{1}{3} \tag{2.55}$$

Two correlated Dahl models are created. The first is called *Full-Dahl* and it consists in the implementation of both the found equations 2.53-2.54, that completely describe the hysteresis. The second is called *Simplified-Dahl* and it only accounts for eq. 2.54, relative to the *unloading* and *reloading* phases. In fig. 2.16 are shown the comparisons between Mindlin and the correlated Dahl models. On the left is shown the comparison for a cycle including macro-slip. The *full-Dahl* model perfectly reproduces Mindlin behavior, while the *simplified-Dahl* shows a substantial error in the *loading* phase, but in the rest of the cycle is superposed to the Mindlin model. On the left, instead, is shown the comparison for a series of cycles in the micro-slip range. Again, the *full-Dahl* perfectly reproduces Mindlin behavior. Concerning the *simplified-Dahl*, it takes some cycles to recover the initial error made on the loading phase.

From the viewpoint of dynamical simulations, where in most of the case it's the steady state cycle that have to be found, the error on the loading phase can be negligible and the *simplified-Dahl* can be used.

The correlation provided here between Mindlin and Dahl models is important because it allows to link a constitutive model derived from the contact physics and which respects the Masing rule, with a dynamic model that allows a faster and easier implementation in dynamic systems. For more details on the correlation please see [38].

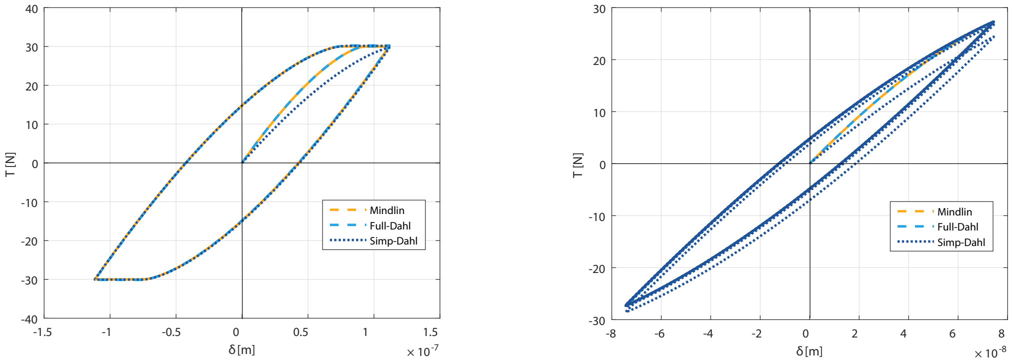

(a) Mindlin and its correlated Dahl models compared for a macro-slip cycle

(b) Mindlin and its correlated Dahl models compared for a macro-slip cycle

Figure 2.16 – Mindlin and its correlated Dahl models compared for a series of micro-slip cycles

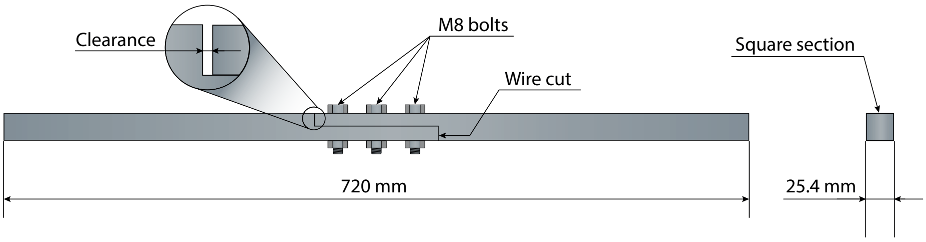

Figure 2.17 – Brake-Reuss Beam (BRB)

2.3 A benchmark test case

In section 1.1 we have seen how an international community, the RMCJS, was created around the issues linked to jointed structures. In the context of this community and in the interest of this work, a period of six weeks was spent taking part at the NOMAD (Nonlinear Mechanics And Dynamics) Research Institute 2016. The latter is a research institute in which a group of 30 graduate students and early career researchers from all over the world are divided into teams and work on a series of projects around the topic of bolted structures. The institute took place at SANDIA National Laboratories in Albuquerque, New Mexico, USA. In the following sections the general behavior of bolted structures described in section 2.1 will be supported by experimental and numerical results obtained with state of the art methods. At the same time, it will be the opportunity to discuss common challenges and problems encountered when studying bolted structures.

2.3.1 Nonlinear Modal Analysis of the Brake-Reuss beam

The Brake-Reuss beam (BRB) [9], shown in fig. 2.17, is a simple test structure consisting of two components obtained by wire-cutting a square-section steel bar, assembled with three M8 bolts. It was designed to provide a common structure for the different projects of a previous edition of the NOMAD Institute. Several specimens are spread out in different laboratories around the world.

Before starting the nonlinear modal analysis, a crucial step when faced to a nonlinear system is to obtain the underlying linear model. This is the very starting point of every modal identification and modeling process, because it allows to create the numerical linear model of the structure. To obtain the dynamic linear properties of a structure (natural frequencies ω_n, damping ratios ζ_n, and the mode shape matrix Φ), a simple modal analysis is performed by using an impact hammer. First an experimental mesh is defined on the structure, so that the mode shapes can be correctly visualized. Then, two main techniques can be used:

1. **Roving Hammer:** low force impacts are carried out at each point of the experimental mesh, and the response is measured by one or more accelerometers. This method requires less accelerometers but the impacts have to be consistent in force and direction, and the testing time is higher.

2. **Roving Accelerometer:** the accelerometers are placed at each point of the experimental mesh and one or more impacts are performed. This method requires less time but a higher number of accelerometers. However, a particular attention has to be paid to the experimental setup, because accelerometers cables can have a substantial influence on the measured damping.

Since the BRB is a small structure and the interest is mainly on the first flexion modes, a roving accelerometer approach is adopted, and ten accelerometers are placed on the beam. The results of the linear modal analysis for the first three flexion modes are shown in fig. 2.18, where an experimental frequency response is plotted, together with the natural frequencies, damping and mode shapes. Afterward a nonlinear modal identification is carried out through a two-step procedure in order to identify the evolution of natural frequency and damping at several excitation levels. The first step consists in a transformation of the physical data into modal coordinates by using a modal filter. In fact, assuming that the mode shapes don't change with the amplitude, it's possible to use the linear mode shape matrix Φ to obtain the modal acceleration $\ddot{q}$ from the time response $\ddot{x}$ as:

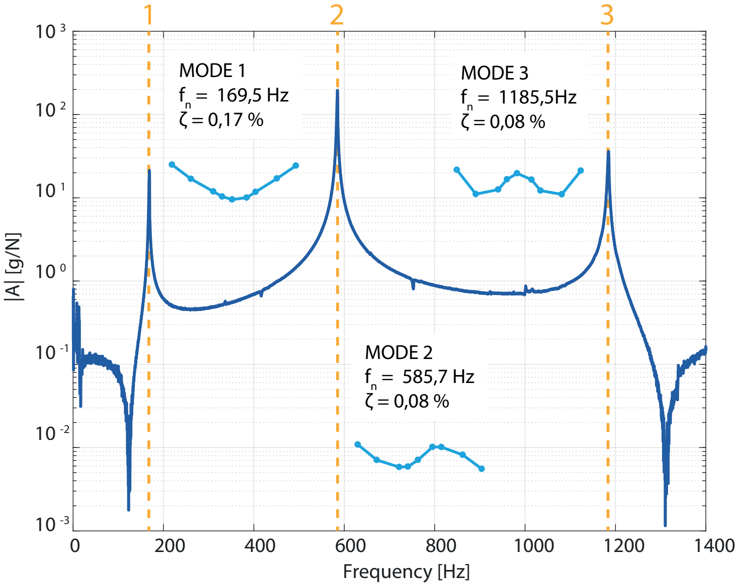

Figure 2.18 – Example of frequency response function for the Brake-Reuss beam and modal parameters for the first three flexion modes

$$\ddot{q} = \Phi^{-1}\ddot{x} \tag{2.56}$$

Each column of $\ddot{q}$ represents the modal acceleration $\ddot{q}_i$ for the i^{th} mode. If needed, on each modal acceleration $\ddot{q}_i$ can be applied a band-pass filter in order to remove other modes interactions and obtain a narrow-band signal for each mode.

The second step consists in the nonlinear modal analysis carried out in the time domain, following the method developed and employed by Deaner et al. [18] and Roettgen et al. [41]. The method uses the Hilbert transform [19] to obtain the analytic signal, with which is possible to calculate the instantaneous oscillating frequency and the signal envelope. On the latter is applied a fourth order spline fit, since the Hilbert transform is very sensitive to signal noise. The nonlinear natural frequency and damping ratio are obtained as a function of modal amplitude and drawn in figs. 2.19b-2.19c. Furthermore, in fig. 2.19a are plotted the frequency response of the BRB at different impact forces, centered on the first mode.

It can be observed that the nonlinear behavior of the jointed beam matches the one described in section 2.1 and qualitatively illustrated by figs. 2.7b, 2.7c, 2.7a. However, they only represent the low amplitude part of the curves. This is due to the fact that impact excitation is limited in the amount of energy that can be conveyed to the structure. In fact, this method can only be applied to small assemblies, but it can provide a good starting point for the non-linearity characterization.

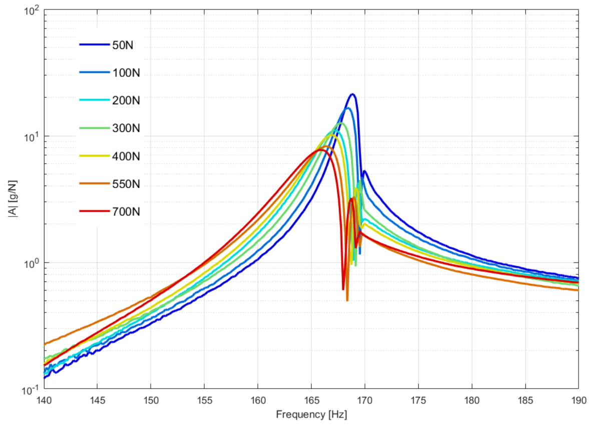

(a) Frequency response centered on the first mode for different levels of impact force

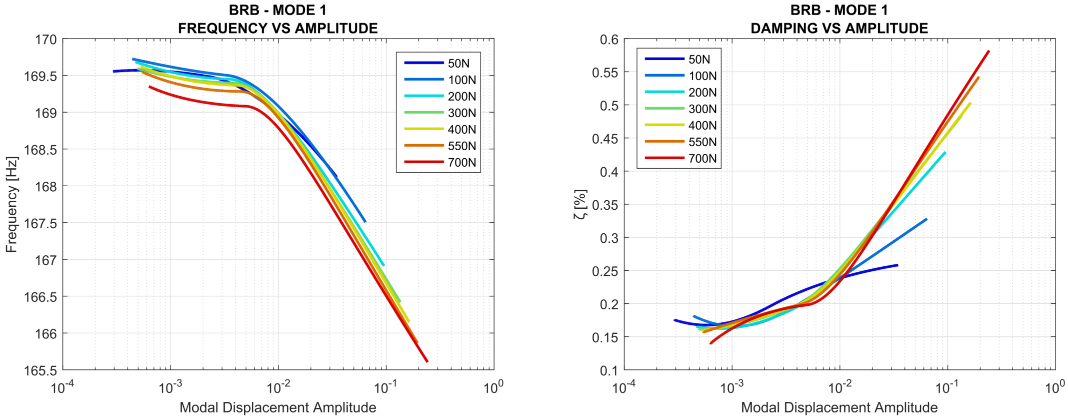

(b) Nonlinear frequency curves for different impact force levels

(c) Nonlinear damping curves for different impact force levels

Figure 2.19 – Nonlinear behavior of the Brake Reuss Beam

2.3.2 The repeatability challenge

As we have seen in section 2.1.2, the uncertainty in the preload application and the mounting of bolted structures can be source of substantial variability. The BRB makes no exception. Even if it's a fairly simple structure, variations of up to 11% on the natural frequencies were found in repeatability tests. Investigation on the phenomenon showed that the dynamics of the BRB is strongly influenced by how the structure is assembled, and in particular by the value of the clearance indicated in fig. 2.17. Several impact tests were carried out for different clearance values and the resulting frequency response around the first flexion mode are shown in fig. 2.20. For each clearance value the structure was disassembled and reassembled three times. It can be observed that, for medium values, the results are consistent and repeatable. On the other hand, for extreme values and in particular for the zero-clearance case, the results show a higher variability. It's possible to find a physical explanation for the last aspect. On the one hand, in the case of zero-clearance, a new contact interface is created, increasing the amount of nonlinearity and uncertainty. On the other hand, for the maximum value of the gap, the bolt shanks come into contact with the bolt holes, which again generates a higher variability. If we consider the natural frequencies relative to the different clearance values, it's possible to observe that the maximum measured one is $\omega_{n,max} \approx 184Hz$, while the minimum is $\omega_{n,min} \approx 166Hz$. The difference between these values is relevant enough to show how important it is, even for a simple structure such as the BRB, to carefully define a mounting procedure in order to have consistent and repeatable results.

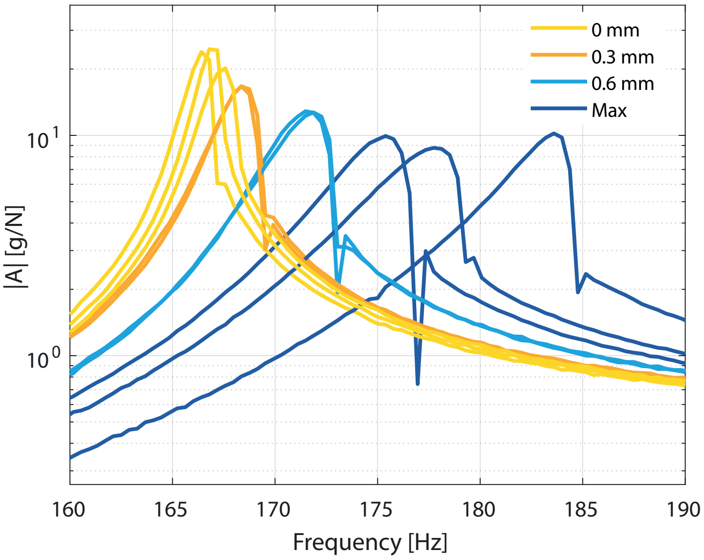

Figure 2.20 – Influence of the clearance value on the BRB frequency response (zoom on the first flexion mode)

2.3.3 The importance of exciting the nonlinearity

Jointed structures usually show the nonlinear behavior described and obtained in previous sections. However, not all the modes of a structure are affected by the non-linearity in the same way. A study on the influence of the far-field structure on the dynamics of the Brake-Reuss beam was carried out at the NOMAD Institute [15]. Three different versions of the BRB, with the same bolted joints, were studied. They are shown in fig. 2.21: the blue one is the original Brake-Reuss Beam (BRB), the green one is the Brake-Reuss beam with spring elements machined on the sides (SBRB), and the red one is a longer version (LBRB). The three structures were tested with the method described in section 2.3.1 and the nonlinear curves for natural frequencies and damping were obtained for the first three flexion modes. The normalized mode shapes of the three beams for the first three flexion modes are shown in fig. 2.22, while the nonlinear damping is displayed in fig. 2.23. The higher variability in the damping values for the third mode is due to the fact that the impact point was close to a node. It can be observed that

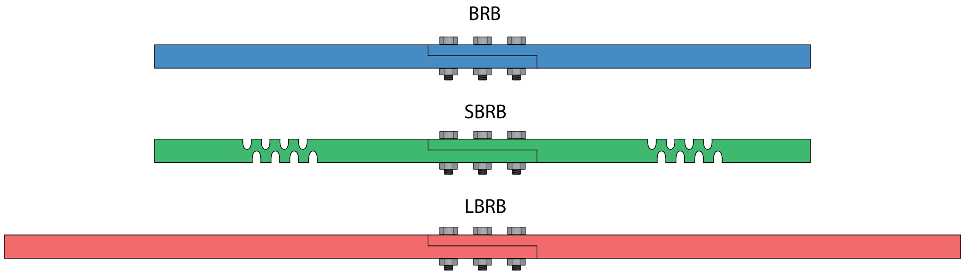

Figure 2.21 – Tested versions of the Brake-Reuss Beam

the BRB and LBRB show the same behavior, with the LBRB characterized by a lower damping for all the three modes. It's possible to justify this feature by comparing the mode shapes: the curvature of the center part, where there are the bolted joints, is always slightly lower for the LBRB than for the BRB. The latter means that the joint region is less excited for the LBRB than for the BRB.

Now, moving our attention to the SBRB, it's interesting to see that for the first two modes it doesn't show any non-linearity, while for the third mode the damping is higher than the other two beams. Again, this aspect can be justified by the curvature of the mode shapes in the bolts region. Since in the SBRB the deformation of the first two modes mainly takes place at the spring elements, the bolts region is almost undeformed, the contacting surfaces don't slide on each other, and dissipation of energy by friction can't be realized. Instead, for the third-mode, the deformation in the jointed region is higher and the damping ratio is slightly greater than for the other beams. Therefore the non-linearity of a mode is closely linked to the mode shape and, since the energy is dissipated through friction, it really depends on how the contact interfaces of a structure are excited.

One could say that this aspect is not clear and that the motivations about the mode shapes can only be perceived visually. For this reason, in the next section, a numerical study on the same beams will be carried out in order to theoretically justify the statement about the importance of mode shapes.

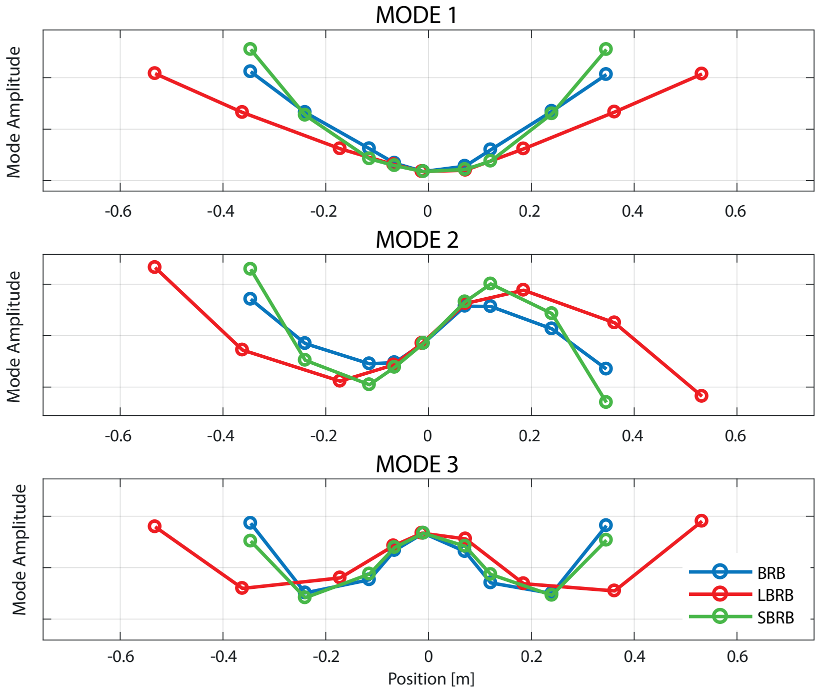

Figure 2.22 – Mode shapes of the three beams for the first three flexion modes

2.3.4 High-detail numerical modeling

The comparison between the BRB and SBRB of the previous section showed a different damping behavior according to the considered mode shapes. Here we'll try to verify the experimental results through high-detail finite element simulations of the two beams using ABAQUS®. The following process has been applied to the BRB and SBRB for the three first flexion modes:

1. Meshing of the structure, including bolts, nuts, and washers.

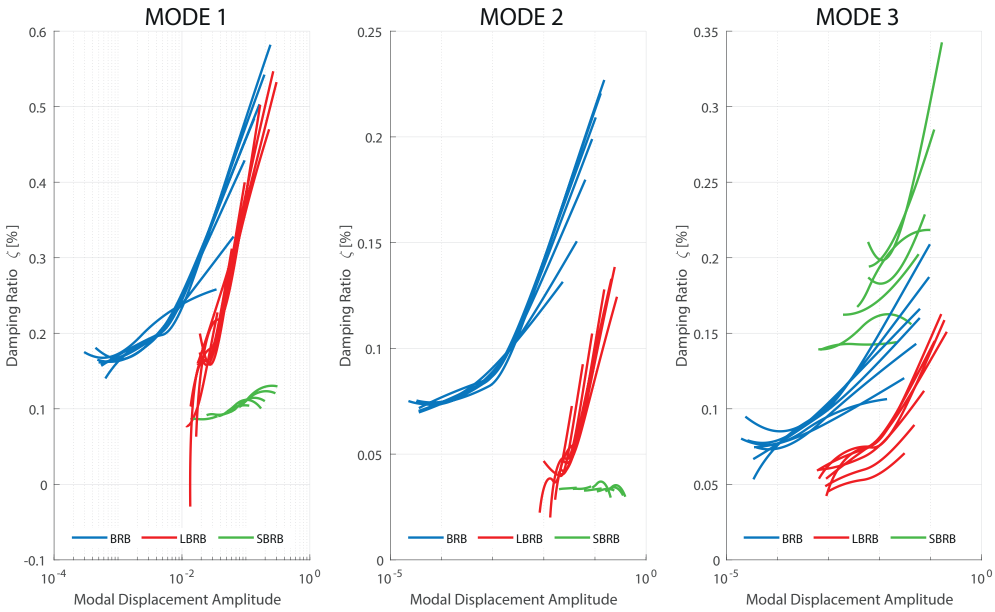

Figure 2.23 – Nonlinear damping ratio of the three beams for the first three flexion modes

2. The contact at the plates interface modeled as an *hard contact* with tangential friction using ABAQUS® *penalty method*

3. Preload the bolts with the *Bolt load* feature.

4. Modal analysis and export of the mass normalized mode shape matrix.

5. Selection of a single mode from the mode shape matrix and imposing the mode displacement to the whole structure, except for the bolted region.

6. Calculation of the friction loss factor η at each displacement step as:

$$\eta = \frac{E_f}{E_s} \tag{2.57}$$

   where E_f is the energy dissipated by friction at the contact interface and E_s is the total strain energy.

The results of this process, compared between the BRB and SBRB, can be shown in figs. 2.24a, 2.24b respectively for the first and third modes. Concerning the first mode, the qualitative behavior of the loss factor is the same as for the experimental results, in which the damping for the BRB shows a non-linearity, while the SBRB is essentially linear. As far as the third mode is concerned, also in this case the numerical results follow the experimental results.
However, high-detail numerical models like the ones analyzed in this section are too computationally expensive for static calculation and practically unemployable for dynamic simulations. Furthermore, convergence problems are often encountered. These disadvantages are due to the probably most important aspect to consider when dealing with bolted structures, which is their multi-scale nature. This important characteristic will be treated in the next section together with another essential aspect of jointed structures: the degree of nonlinearity.

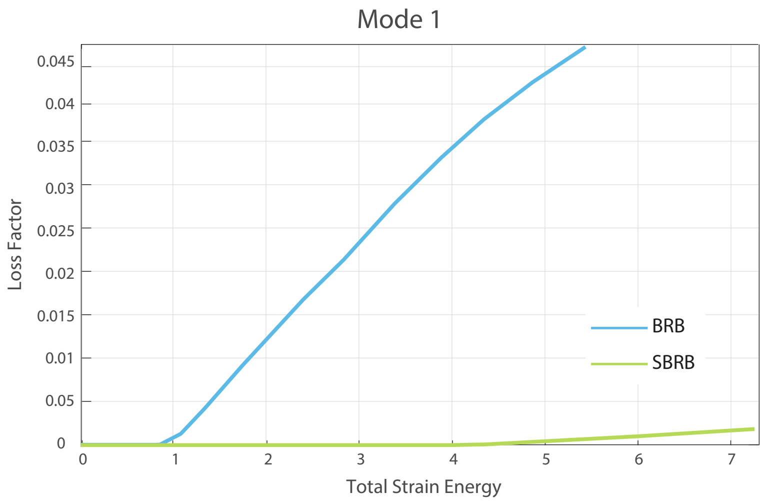

(a) Mode 1

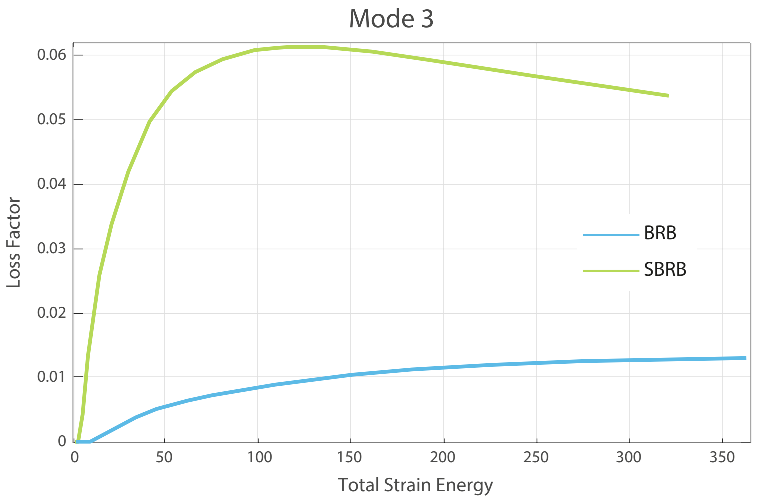

(b) Mode 3

Figure 2.24 – Comparison of friction loss factor η between BRB and SBRB

2.3.5 The multi-scale issue and the weak non-linearity assumption

The title of this section pretty much sums up the essence of bolted structures. Let's take a look at fig. 2.25. In the figure is shown the upper part of the Ariane 5 space launcher, which contains the *SYstème de Lancement Double Ariane* (SYLDA), a system that allows the deployment of two payloads at once. The SYLDA is assembled through bolted joints, which were object of studies during the MAIAS project [20]. However, as it is the case for most structures, the bolted joints only represent a small portion of them. Now, if we think about the friction energy dissipation mechanism, this depends on the properties of the contact interface, such as surface defects and roughness. Therefore, we can distinguish at least three different scales: the whole structure level, the bolted joint level, and the contact interface level that, if we want to be really honest, can still be divided in several levels. The multi-scale character of bolted structures is the reason why it's essentially impossible to correctly model them numerically without getting caught up in unacceptably long simulations. The objective of any researcher or engineer working with bolted structures will then be to minimize the simulation time while being capable of describing their dynamics with an acceptable precision.

Bolted joints are very nonlinear, assemblies only a bit

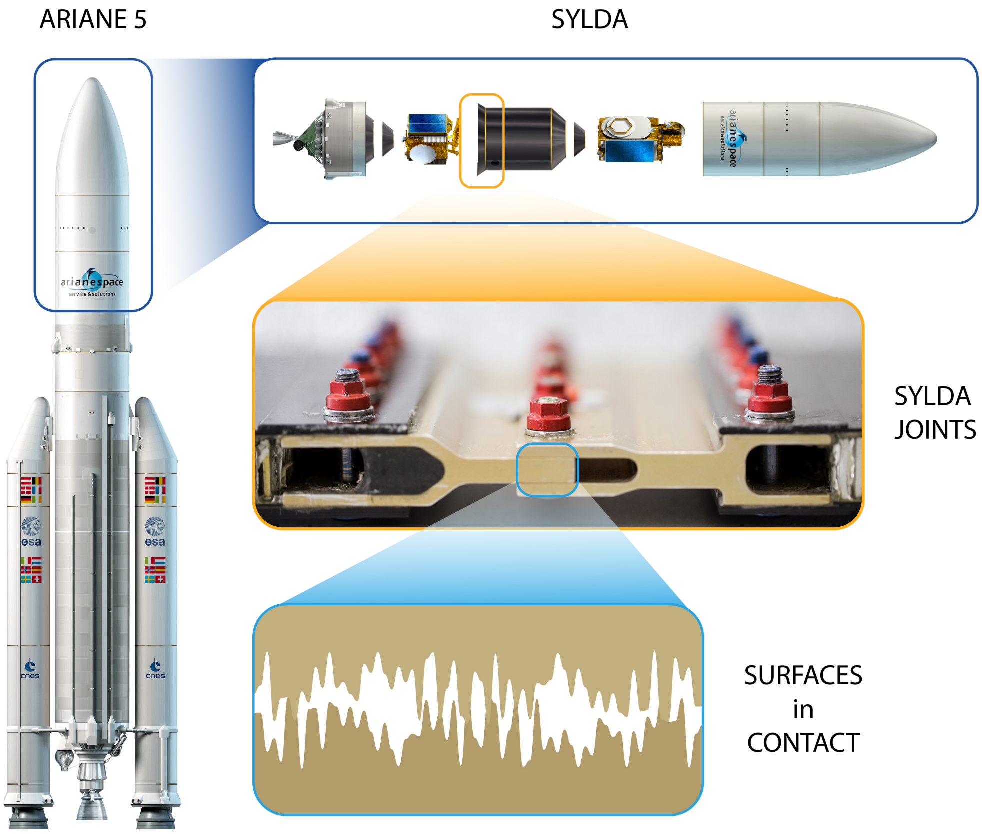

Figure 2.25 – The multi-scale properties of assemblies

In doing so, there is another important aspect to take into account: the degree of non-linearity. In fact, if we consider a single bolted joint, the latter will show a marked nonlinear behavior. However, if the same joint is included in a much larger structure — which is usually the case — then the global non-linearity will be less visible. This is why bolted structures can be considered as weakly nonlinear systems and some assumption from the linear theory can be kept. For example, as we have seen in section 2.3.1, it was assumed that mode shapes don't change significantly with an increasing excitation amplitude. Furthermore, since it's not desirable that bolted joints enter in the macro-slip phase because it could lead to joint failure, the non-linearity is always limited to the micro-slip phase. However, if the degree of non-linearity is larger, there will be the need for fully nonlinear identification and modeling methods.
The current work is oriented towards two main objectives:

1. **MODELING**: provide a tool, specifically a connector, being able to reproduce bolted joints non-linearities.
2. **IDENTIFICATION**: provide a series of methods for the qualitative and quantitative identification of non-linearities caused by bolted joints.

In the development of these tasks, the principle that has always to be kept in mind is the trade-off between the accuracy of results and the effort — time, user-interaction, etc. — to obtain them.

Bibliography

[1] Ames, N. M., Lauffer, J. P., Jew, M. D., Segalman, D. J., Gregory, D. L., Starr, M. J., and Resor, B. R. (2009). Handbook on dynamics of jointed structures. (July). 22, 23

[2] Armstrong-Hélouvry, B., Dupont, P., and De Wit, C. C. (1994). A survey of models, analysis tools and compensation methods for the control of machines with friction. *Automatica*, 30(7):1083–1138. 26

[3] Bachus, K. N., DeMarco, A. L., Judd, K. T., Horwitz, D. S., and Brodke, D. S. (2006). Measuring contact area, force, and pressure for bioengineering applications: Using Fuji Film and TekScan systems. *Medical Engineering and Physics*, 28(5):483–488. 22

[4] Berger, E. (2002). Friction modeling for dynamic system simulation. *Applied Mechanics Reviews*, 55(6):535. 25

[5] Bickford, J. (1990). *An introduction to the design and behavior of bolted joints. Second edition, revised and expanded.* 21

[6] Bliman, P. (1992). Mathematical study of the Dahl's friction model. *European Journal of Mechanics. A/Solids*, 11(September):835–848. 29

[7] Bliman, P. and Sorine, M. (1995). Easy-to-use realistic dry friction models for automatic control. In *Proceedings of 3rd European Control Conference*, pages 262–272. 29

[8] Bliman, P.-A. and Sorine, M. (1993). A system-theoretic approach of systems with hysteresis: application to friction modeling and compensation. *Proceedings of the second European control conference*, 1:1844–1849. 29

[9] Brake, M. R. W. (2018). *The Mechanics of Jointed Structures.* Springer International Publishing, Cham. 18, 19, 38

[10] Budynas-Nisbett (2006). Mechanical Engineering : Shigley's Mechanical Engineering Design 8th Edition. page 1059. McGraw Hill. 20, 21

[11] Chiang, D. Y. (1999). The generalized Masing models for deteriorating hysteresis and cyclic plasticity. *Applied Mathematical Modelling*, 23(11):847–863. 29

[12] Ciavarella, M. (1998a). The generalized cattaneo partial slip plane contact problem. I - Theory. *International Journal of Solids and Structures*, 35(18):2349–2362. 34

[13] Ciavarella, M. (1998b). The generalized cattaneo partial slip plane contact problem. II - Examples. *International Journal of Solids and Structures*, 35(18):2349–2362. 34

[14] Ciavarella, M., Demelio, G., Barber, J. R., and Jang, Y. H. (2000). Linear elastic contact of the Weierstrass profile. *Proceedings of the Royal Society A: Mathematical, Physical and Engineering Sciences*, 456(1994):387–405. 34

[15] Cooper, S. B., Rosatello, M., Mathis, A. T., Johnson, K., Brake, M. R. W., Allen, M. S., Ferri, A. A., Roettgen, D. R., Pacini, B. R., and Mayes, R. L. (2017). Effect of Far-Field Structure on Joint Properties. In *Dynamics of Coupled Structures, Volume 4*, pages 63–77. Springer. 41

[16] Dahl, P. (1968). A Solid Friction Model. *Aerospace Corporation El Segundo, CA*, 158:Tech. Rep. TOR–01 58(3 107–1 8)– 1. 27

[17] de Wit, C. C., Lischinsky, P., Åström, K. J., and Olsson, H. (1995). A New Model for Control of Systems with Friction. *IEEE Transactions on Automatic Control*, 40(3):419–425. 29

[18] Deaner, B. J., Allen, M. S., Starr, M. J., Segalman, D. J., and Sumali, H. (2015). Application of Viscous and Iwan Modal Damping Models to Experimental Measurements From Bolted Structures. *Journal of Vibration and Acoustics*, 137(2):021012. 39

[19] Feldman, M. (2011). Hilbert transform in vibration analysis. *Mechanical Systems and Signal Processing*, 25(3):735–802. 39

[20] Festjens, H. (2014). Contribution à la caractérisation et à la modélisation du comportement dynamique des structures assemblées. 44

[21] Gaul, L. and Lenz, J. (1997). Nonlinear dynamics of structures assembled by bolted joints. *Acta Mechanica*, 125(1-4):169–181. 23, 28

[22] Gaul, L. and Nitsche, R. (2001). The Role of Friction in Mechanical Joints. *Applied Mechanics Reviews*, 54(2):93. 23, 25

[23] Graves, F. E. (1984). Nuts and Bolts. *Scientific American*, 250(6):136–144. 18

[24] Haessig, D. A. and Friedland, B. (1991). On the Modeling and Simulation of Friction. *Journal of Dynamic Systems, Measurement, and Control*, 113(3):354. 29

[25] Ito, Y., Toyoda, J., and Nagata, S. (1979). Interface Pressure Distribution in a Bolt-Flange Assembly. *Journal of Mechanical Design*, 101(2):330–337. 21

[26] Iwan, W. D. (1966). A Distributed-Element Model for Hysteresis and Its Steady-State Dynamic Response. *Journal of Applied Mechanics*, 33(4):893. 30, 31

[27] Johnson, K. L. (1985). *Contact Mechanics*, volume 37. Cambridge University Press, Cambridge. 34, 35

[28] Karnopp, D. (1985). Computer Simulation of Stick-Slip Friction in Mechanical Dynamic Systems. *Journal of Dynamic Systems, Measurement, and Control*, 107(1):100. 26

[29] Lehnhoff, T. F. and Mckay, M. L. (2016). Member Stiffness and Contact. 21

[30] Majumdar, A. and Bhushan, B. (1991). Fractal Model of Elastic-Plastic Contact between Rough Surfaces. *Journal of Tribology-Transactions of the Asme*, 113(1):1–11. 34

[31] Majumdar, A. and Tien, C. L. (1990). Fractal characterization and simulation of rough surfaces. *Wear*, 136(2):313–327. 34

[32] Menq, C. H., Griffin, J. H., and Bielak, J. (1986). The influence of microslip on vibratory response, Part I: A comparison with experimental results. *Journal of Sound and Vibration*, 107(2):295–307. 23

[33] Motosh, N. (1976). Development of Design Charts for Bolts Preloaded up to the Plastic Range. *Journal of Engineering for Industry*, 98(3):849. 20

[34] Olsson, H., Åström, K., Canudas de Wit, C., Gäfvert, M., and Lischinsky, P. (1998). Friction Models and Friction Compensation. *European Journal of Control*, 4(3):176–195. 25

[35] Orban, F. (2011). Damping of materials and members in structures. *Journal of Physics: Conference Series*, 268(1). 18

[36] Pesaresi, L., Armand, J., Schwingshackl, C. W., Salles, L., and Wong, C. (2018). An advanced underplatform damper modelling approach based on a microslip contact model. *Journal of Sound and Vibration*, pages 1–14. 22, 24, 28

[37] Peyret, N., Dion, J. L., and Chevallier, G. (2016). A framework for backbone experimental tracking: Piezoelectric actuators, stop-sine signal and Kalman filtering. *Mechanical Systems and Signal Processing*, 78:28–42. 18

[38] Peyret, N., Rosatello, M., Chevallier, G., and Dion, J. L. (2017). A Mindlin derived Dahl friction model. *Mechanism and Machine Theory*, 117:48–55. 36, 37

[39] Quinn, D. D. (2012). Modal analysis of jointed structures. *Journal of Sound and Vibration*, 331(1):81–93. 23

[40] Rabinowicz, E. (1951). The nature of the static and kinetic coefficients of friction. *Journal of Applied Physics*, 22(11):1373–1379. 26

[41] Roettgen, D. R. and Allen, M. S. (2017). Nonlinear characterization of a bolted, industrial structure using a modal framework. *Mechanical Systems and Signal Processing*, 84:152–170. 39

[42] Rotscher, F. (1927). *Die Maschinenelemente*. Springer, Berlin. 21

[43] Sanliturk, K. Y., Imregun, M., and Ewins, D. J. (1997). Harmonic Balance Vibration Analysis of Turbine Blades With Friction Dampers. *Journal of Vibration and Acoustics*, 119(1):96. 24

[44] Segalman, D. J. (2001). An Initial Overview of Iwan Modeling for Mechanical Joints Acknowledgments. *Control*, (March):3–8. 19, 22, 31

[45] Segalman, D. J. (2005). A Four-Parameter Iwan Model for Lap-Type Joints. *Journal of Applied Mechanics*, 72(5):752. 31

[46] Skelton, R. P., Maier, H. J., and Christ, H. J. (1997). The Bauschinger effect, Masing model and the Ramberg-Osgood relation for cyclic deformation in metals. *Materials Science and Engineering A*, 238(2):377–390. 29

[47] Song, Y., Hartwigsen, C. J., McFarland, D. M., Vakakis, A. F., and Bergman, L. A. (2004). Simulation of dynamics of beam structures with bolted joints using adjusted Iwan beam elements. *Journal of Sound and Vibration*, 273(1-2):249–276. 18

[48] Stribeck, R. (1902). Die Wesentlichen Eigenschaften der Gleit-und Rollenlager [The key qualities of sliding and roller bearings]. *Z. Vereines Seutscher Ing*, 46:1432–1437. 26

[49] Ungar, E. E. (1964). Energy Dissipation at Structural Joints; Mechanisms and Magnitudes.pdf. Technical report, Bolt Beranek and Newman Inc. 18

[50] Valanis, K. C. (1978). Fundamental Consequences of a New Intrinsic Time Measure. Plasticity as a Limit of the Endochronic Theory. 28

[51] Wileman, J., Choudhury, M., and Green, I. (1991). Computation of Member Stiffness in Bolted Connections. *Journal of Mechanical Design*, 113(4):432. 21

[52] Wojewoda, J., Stefański, A., Wiercigroch, M., and Kapitaniak, T. (2008). Hysteretic effects of dry friction: modelling and experimental studies. *Philosophical Transactions of the Royal Society A: Mathematical, Physical and Engineering Sciences*, 366(1866):747–765. 23

A finite element connector system for bolted joints dynamics

3

Contents

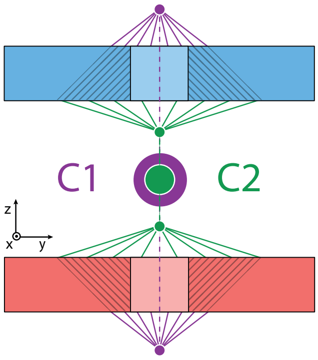

Summary Numerical simulation of bolted structures is not an easy task. The main problem is represented by the fact that usually bolted joints represent a small part of the whole structure. This generates a multi-scale problem, very expensive to solve with finite elements method. On the other hand, the physics behind bolted joints requires a precise modeling, particularly the friction behavior. The aim of this chapter is to develop a connector system to model the bolted joints dynamics, whose parameters are derived from geometrical dimensions and measurable quantities of the physical system, defined in the design phase.

3.1 FEM modeling of bolted joints

The goal of this section is to describe the development of finite element modeling of bolted joints and the most adopted methods that existing in the dedicated literature. The modeling of bolted joints is divided in two big fields, depending on the objectives and requirements. The first one concerns the modeling of the quasi-static behavior of joints, in order to verify the compliance of a structure to the standards. The second concerns the dynamic behavior. For both fields, the goal of the modeling process is to provide a numerical tool that accurately reproduces the behavior of the real structure, while at the same time keeping the computational time compatible with the time constraints of the industrial design process. Usually, for the quasi-static modeling, the degree of detail needed is higher, especially in the local description of stresses and pressure fields. On the other hand, for the dynamic modeling the constraints in simulation time are more strict, so that a lower degree of local details is accepted in order to speed up the calculations.

3.1.1 Quasi-Static modeling

One of the first attempts to numerically model a bolted joint was performed by Wileman et al. [58], in which the authors use the FEM to model the bolt preload and to obtain the stiffness of the jointed components, usually called *member stiffness* (more on that later in section 3.4.3.1), and to compare it with the existing analytical methods. Kim. et al. [25] compared four different ways of modeling bolted joints. The models are shown in fig. 3.1 and they can be named as it follows:

a) Solid bolt model: it's the reference solution, where the bolt is modeled with 3D elements;

b) Coupled bolt model: in this version, the bolt is replaced by a beam element, whose nodes are connected to the respective surfaces through a series of beam elements;

c) Spider bolt model: the same as the coupled bolt model, but in this case the links between the beam representing the bolt and the respective surfaces take place through a DOF coupling;

d) No-bolt model: it is only composed by a pressure load applied on the annular surfaces corresponding to the bolt and nut faces in contact with the upper and lower surfaces.

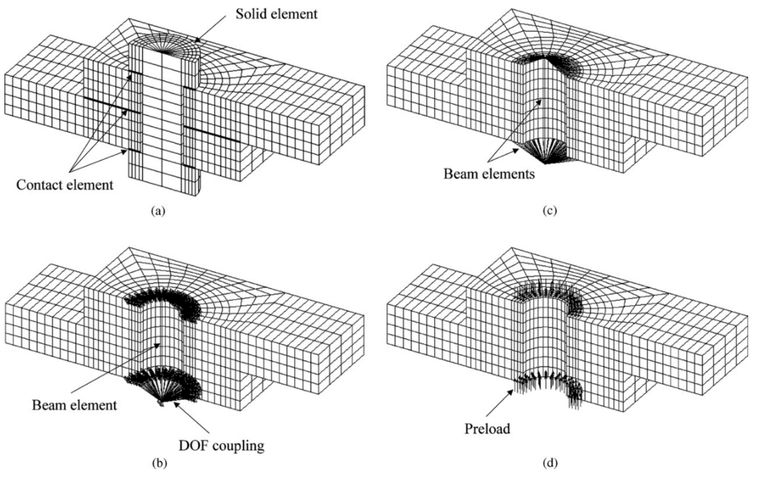

Figure 3.1 – FE models for bolted joints - Source: [25].

Regarding the contact between the plates, in all of the models it's described through detailed contact elements. The listed models include types of connector and elements that can be found in most of the commercial finite element softwares. Kim et al. concluded that, from a computational time and effectiveness point of view, the most recommended models are the coupled and the spider ones.

Beside this simple comparison, more elaborate models are developed. In the field of composite joints, relevant is the work of McCarthy [31, 32, 30]. In [19], Gray and McCarthy developed the Global Bolted Joint Model (GBJM), which is a combination of beam elements, surfaces, and connectors implemented in ABAQUS®. The GBJM is shown in fig.3.2 and it consists of two linear beam elements, representing the bolt, and two rigid surfaces, representing the bolt external surface. Furthermore, the plates of the lap-joint are reduced from 3D elements to shell surfaces. The contact between the assembled components and between the hole and the bolt are modeled with the master-slave approach of ABAQUS®. Friction is considered only for the contact between the plates and is modeled by ABAQUS® penalty method. The results obtained with the GBJM demonstrate accuracy and efficiency in the reproduction of the results from a full 3-D model. In fact, the GBJM allows CPU time saving of up to 97%, based on the number of joints modeled.

Askri et al [4] pointed out that the problem with the GBJM is the identification of the equivalent stiffness to input in the model. They therefore developed a reduced model of fastener using Multi-Connected Rigid Surfaces (MCRS), shown in fig.3.3. It consist of four rigid surfaces and four stiffnesses, determined by looking at the main deformation modes of real bolts. Also in this case, the global behavior of the lap joint is correctly modeled and computation time can be reduced by about 85%.

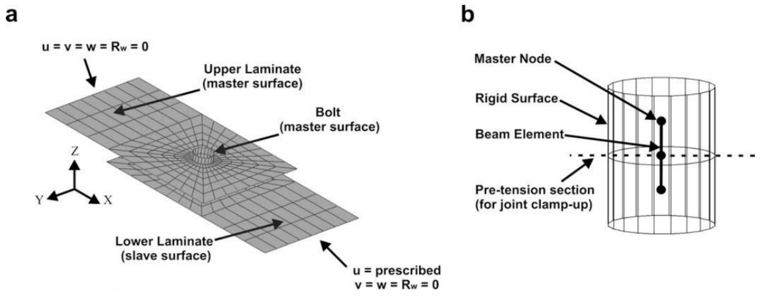

Figure 3.2 – Global Bolted Joint Model (GBJM) - Source: [19].

A recent work on the design of a finite element connector to model bolted joints was issued by Soule de Lafont [56], and it was part of the CARAB project (see section 1.1).

A problem that all the described models have in common is that, while they accurately reproduce the global structure behavior, locally the stresses and pressure fields can be subjected to errors. In addition, the way in which contact and friction are treated is not suitable for dynamic problems, especially if time simulations have to be performed. In the next section the attention will be moved to the main existent approaches for modeling bolted joints dynamics.

3.1.2 Dynamic modeling

The design of a finite element tool being able to reproduce bolted joint dynamics is an ongoing research topic and there exist different ways of approaching the problem. The design depends on the degree of precision needed and the domain — time or frequency — in which the calculation is carried out. In the following sections are described the main existing strategies that have been subject to extensive review and comparison [7, 8, 27]. The differences between the

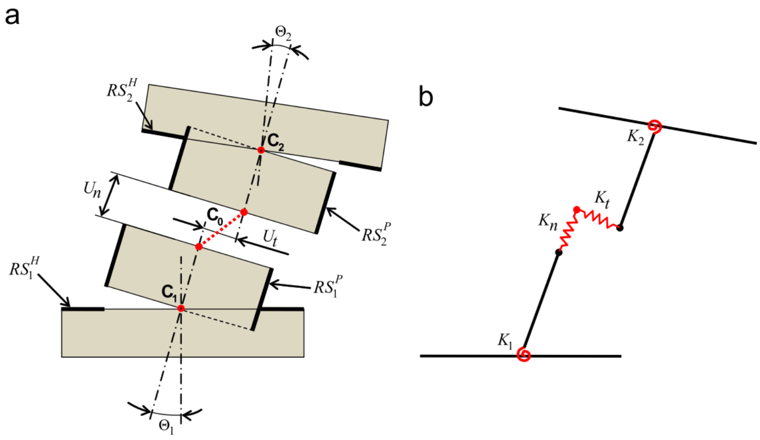

Figure 3.3 – Multi-Connected Rigid Surfaces (MCRS) - Source: [19].

methods mainly lie on the way the contact interfaces are connected to each other.

3.1.2.1 Node-to-node

The node-to-node technique consists in linking single nodes of the first contact surface to the respective single nodes of the second surface with an element in which a linear or nonlinear law can be implemented. The solution for this kind of models is usually computed using the Harmonic Balance Method (HBM), which is a common frequency domain method to compute a system's frequency response, instead of integrating in time.
This method is particularly flexible because it allows the implementation of different nonlinear laws in the node-to-node elements and it is currently used to design turbine blade underplatform dampers [41]. An example of 3D node-to-node element — also called micro-slip element — was developed by Petrov et al. [42] and it is shown in fig. 3.4a. It is composed of two Jenkins slider in the contact plane directions, and of a normal stiffness with gap detection on the normal axis.
Once defined the basic contact element, their number and distribution on the contact interface can be defined. In [49] Schwingshackl et al. tested several distributions in order to model the dynamic behavior of bolted flange joints, which are characterized by the fact of having a particularly non-uniform contact pressure distribution. Examples of 3D elements distributions are shown in fig. 3.4b. The distribution is of crucial importance to correctly model the nonlinear behavior and it depends on aspects such as the type of joints and surface shape imperfections. Another important parameter is the initialization of the normal force and gap in each 3D element, which represents the initial conditions after the bolt preload. Since the contact pressure at the interface is not the same everywhere, the input values for the 3D elements are obtained by applying the preload on a full FE model and by calculating the Voronoi polygons on the resulting contact pressure and gap [27].
In a recent work, Pesaresi et al. [41] used the same 3D contact element, this time including a Valanis friction model (see section 2.2.2.2), and they developed a numerical tuning procedure for their parameters. At the same time, Armand et al. [3] evaluated the effect of surface roughness on the dynamics of bolted joint, again using the same micro-slip element.
The main advantages of the node-to-node technique is that it is possible to accurately describe the local behavior by rearranging the microslip contact elements, and that the reliance on experimental data is minimal, since the parameters of the contact elements depend only on the contact properties. The latter can be theoretically deducted without having to perform experimental tests, which is promising for the prediction of nonlinear dynamic behavior of bolted

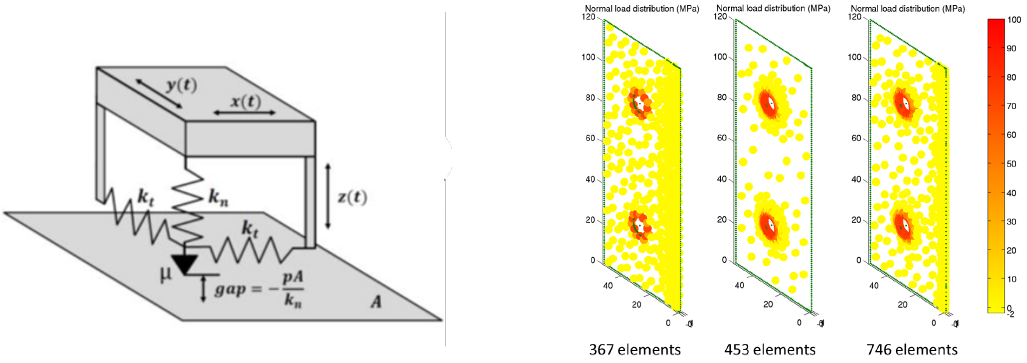

(a)

(b)

Figure 3.4 – 3D contact element (left) and different distributions at the joint interface (right). Source [49].

structures.

Regarding the disadvantages, the first one is the need for coincident mesh between the surfaces in contact, which affects the time for the simulation setup. Then, the selection of the correct contact elements distribution could be difficult to find and it can require a high number of elements, which makes the technique unsuitable for time simulations. In fact, the numerical method normally used for this technique is the multi-harmonic balance method. Finally, because of the said inconvenience to time integration, the simulations are restricted to periodic forcing and the transient behavior of the structure can't be accurately evaluated. In the aerospace field, however, it can be essential sometimes to be able to evaluate the dynamic behavior of a structure subjected to transient or sudden loads.

3.1.2.2 Whole joint

The whole-joint approach was developed by Segalman [51] and the principle is to model each bolted joint through a macro-model. To understand how this is carried out, let's take a look at fig. 3.5. The contact interface is divided into several patches, usually consisting of the surfaces around the bolt-holes. Each one of these patches is rigidly coupled to a single virtual node by Rigid Body Elements (RBE), a type of Multi Point Constraints (MPC), which serves to link one node to a group of nodes. Two types of RBE can be used:

- RBE2: one independent node is linked to several dependent nodes. The relative position between the independent node and the dependent nodes remains constant. This creates a kinematic coupling between selected nodes.
- RBE3: one dependent node is linked to several independent nodes. The position of the dependent node is determine by a weighted average of the independent nodes position. This creates a distributed coupling between selected nodes.

For each contact patch a virtual node is created and linked to the patch through a MPC. Afterward, each virtual node of the first surface is linked to the corresponding virtual node of the second surface by a nonlinear element. The latter is composed of a linear spring in the normal direction to model the bolt stiffness, and of a four-parameter Iwan model [50] in the tangential plane to model the friction behavior. The Iwan model is chosen because of its relatively simple implementation and for its ability to reproduce the nonlinear energy dissipation behavior. Moreover, each Iwan element already represents a particular distribution of Jenkins sliders.

The number of Iwan element needed to model the structure is lower than for the node-to-node

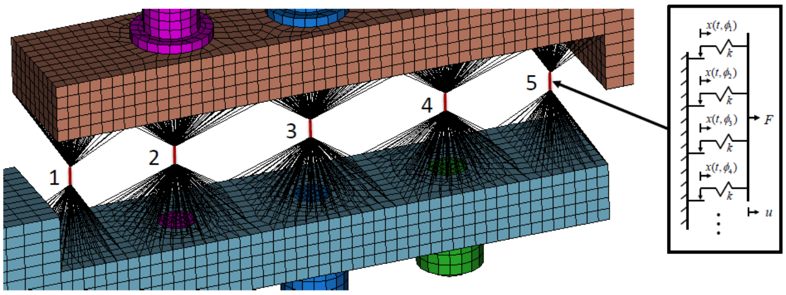

Figure 3.5 – Whole joint approach. Source: [27].

approach. This makes the whole-joint approach more adapted to simulations in the time domain. Furthermore, assuming that the mode shapes of the structure only slightly vary with the non-linearity, it's possible to apply common model order reduction techniques [6] in order to reduce CPU time. A quasi-static modal analysis can then be performed to obtain the modal quantities [59] [52][16] [2].

The whole-joint method is able to closely reproduce the non-linear behavior of natural frequency and damping. However, as demonstrated in a recent study by Lacayo et al. [28], the modal Iwan model is unable to correctly fit natural frequency and damping from experimental results *at the same time*. In fact, there exist a Pareto limit and the choice between closely fitting natural frequency *or* damping has to be made. Considered that the nonlinear frequency shift is very low compared to the damping one, usually the choice falls on the damping, for which in general the error is more pronounced.

The main advantages of the whole-joint model is that it's a relatively simple representation of the joint, and the quasi-static modal analysis is computationally efficient, allowing the calculation of a nonlinear backbone curves in a few seconds [27].

On the other side, there are several disadvantages. Firstly, differently from the node-to-node technique, the whole-joint approach is not able to provide details about the full interface contact mechanics and the determination of parameters heavily relies on experimental data. Furthermore, there are several aspects that can significantly influence the results, such as the choice of contact patches (size, number, position, shape etc.), macro-model, and reduction technique.

3.1.2.3 Other approaches

The node-to-node and whole-joint techniques are the most used, but there exist a certain number of other methods that have been used or that could be rethought to model the dynamics of bolted joints. A brief description will be provided to complete the big picture on the topic.

Thin layer elements This linear modeling method has its origin in the field of geomechanics [15, 53] and it has been used to model soil and rocks structures interactions. It consists of inserting a layer of thin linear elements — with a maximum aspect ratio of 100 — at the contact interface. These elements are characterized by a linear stiffness and an hysteretic damping that is obtained experimentally from an isolated joint. The method provides acceptable results for the modeling of a simple joint but, for multiple joints structures, it shows all its limits [7]. However, the method remains very simple to implement, even in commercial FE software. A different thin layer element formulation for the application on bolted structures has been developed by Ahmadian et al. [1].

Zero thickness elements The principle is the same as the previous thin layer elements, but in this case the elements that are inserted at the contact interface consists of two quadrilateral elements, one for each contact surface, facing each other [17][57]. A nonlinear normal and tangential physical contact law regulates the relative displacement between the top and bottom quadrilateral. The method allows for a detailed simulation of the contact mechanics both in time and frequency domain. However, the substantial drawback is that the simulation time can quickly become unacceptably long. Again, the endless struggle between high details and time consumption takes place.

Structure oriented approaches There are some techniques that are developed for a particular structure or type of joints. For example, Luan et al. [29] designed a nonlinear model for the analysis of bolted flange joints. Another one is the work of Claeys et al.[14], in which they develop a model for a particular test structure. Finally, it is important to mention the Adjusted Iwan Beam Element (AIBE), provided by Song et al. [55], which is a two-dimensional nonlinear element for the dynamic response of beam structures containing bolted joints.

3.1.3 Placing of the new connector system

Once described the different existing approaches, it's time to explain the objective of the bolted joint model developed in this work.

The aim of the current work is to design a connector system that will make it possible to correctly model the *dynamic* behavior of a bolted joint, by following the whole-joint approach. However, in the previous section we have seen that one of the disadvantages of the whole-joint approach is the difficulty in parameter identification, which heavily relies on experimental data. The main and most important aspect of the new connector system is that its parameters **must** be determinable only from physical specification of the joint and surface properties.

The other goal, more practice-oriented, is to make the connector easy to implement. In particular, the geometry won't have to be modified in order to insert the connector system. Furthermore, the connector will be used to perform time simulations. Therefore, the nonlinear laws introduced in the connector system will have to describe the physical phenomena in an acceptable way, while limiting their complexity. Finally, a model order reduction will be applied to perform fast simulations and to obtain the nonlinear evolution of modal parameters.

In the frame of the CLIMA project (see chapter 1), the design of the connector system has been performed by the author of this dissertation, while the implementation and simulation has been carried out by taking advantage of the experience of the structural dynamics toolbox software company SDTOOLS.

Before moving on to the description of the developed connector system, it's important to open a parenthesis on the modeling of normal and tangential contact between rough surfaces, which have a relevant role in the connector design.

3.2 Normal contact of rough surfaces

When two bodies with rough surfaces are pressed together, the *real* contact surface is much lower than the *apparent* contact area. This is an important aspect in many engineering fields. For example, the real contact area can define the thermal and electrical resistance, the wear to expect for a particular application, and it's a key factor for all frictional processes. The most used method to determine the contact area evolution is the Greenwood -Williamson method [20], proposed in 1966.

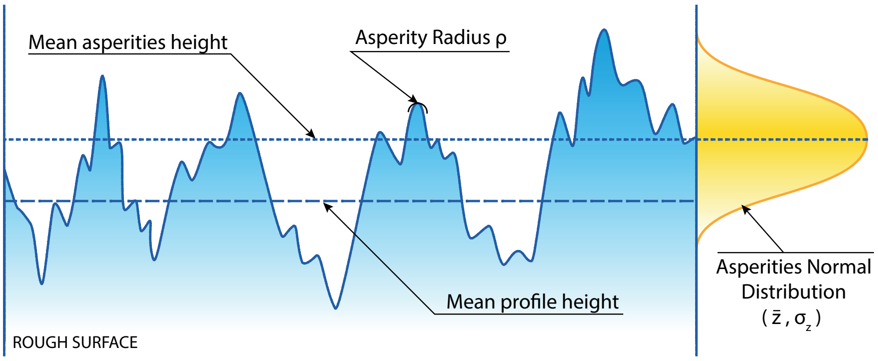

Figure 3.6 – Example of rough profile and its asperity peak-height distribution

3.2.1 Assumptions

The original version of the method considers the static contact of a solid with an undeformable flat and smooth surface, pressed against a solid with a deformable rough surface. The rough surface of the second solid is nominally flat and it's characterized by a large number of asperities. The assumptions made on the asperities are the following:

- The rough surface profile is isotropic;
- The asperities peaks are considered spherical;
- The rough surface is formed by a total of N_0 asperities, which have the same spherical peak radius ρ and their height follows a Gaussian distribution;
- There is no interaction between asperities;
- Only the asperities are deformed, while there is no global surface strain.

The asperity peak height Gaussian distribution can therefore be written as:

$$\phi(z) = \frac{1}{\sigma_z\sqrt{2\pi}} e^{\frac{1}{2}\left(\frac{z-\bar{z}}{\sigma_z}\right)^2} \tag{3.1}$$

where z is the asperity peak height, while $\bar{z}$ and σ_z are respectively the asperity peak-height mean and standard deviation. Fig. 3.6 shows an example of rough surface 1-D profile and its asperity peak-height Gaussian distribution. It's important not to confuse the asperity peak height distribution with the overall roughness profile distribution, which can lead to errors in the contact evaluation.

3.2.2 Equations

After having characterized the rough surface, it's now possible to put it in contact with the perfectly smooth and flat surface. This situation is shown in fig.3.7, where we can define the separation d as the distance between the flat surface and the plane of the rough surface defined by the **average profile height**. By using the distribution found in eq. 3.1 it's possible to calculate, for each value of the distance d, the expected number of asperities in contact N_d as:

$$N_d(d) = \int_d^{\infty} N_0\phi(z)dz \tag{3.2}$$

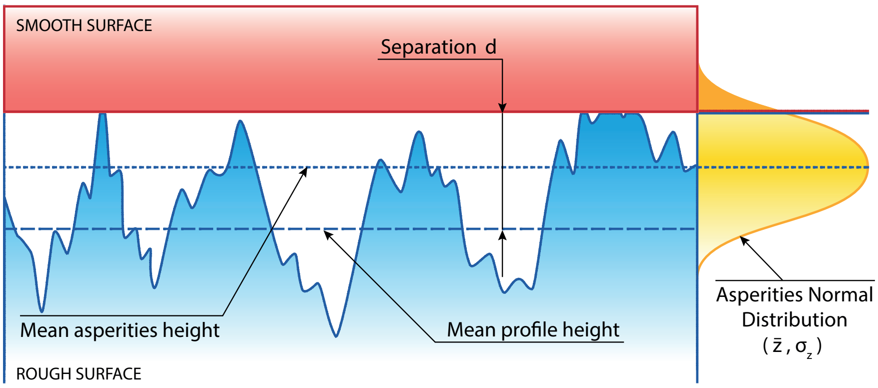

Figure 3.7 – Flat surface in contact with the rough one

Each of the asperity is then treated as an Hertzian contact [22], where the individual contact radius r, contact area a, and normal force F_z are obtained as:

$$
\begin{aligned}
r &= \sqrt{\rho(z-d)} &(3.3)\\
a &= \pi\rho(z-d) &(3.4)\\
F_z &= \frac{4}{3}E^*\sqrt{\rho}(z-d)^{3/2} &(3.5)
\end{aligned}
$$

where

$$E^* = \frac{E}{1-\nu^2} \tag{3.6}$$

is the combined Young's modulus between the sphere and the rigid plane, assuming they are made of the same material. By combining eqs. 3.5 and the statistical description of the rough surface, it's possible to calculate the real contact area A_d as

$$A_d(d) = \int_d^{\infty} N_0\phi(z)\pi\rho(z-d)dz \tag{3.7}$$

and the total normal contact force F_d as:

$$F_d(d) = \int_d^{\infty} \frac{4}{3}N_0\phi(z)E_e\sqrt{\rho}(z-d)^{3/2}dz \tag{3.8}$$

Finally, the nonlinear normal stiffness K_n, function of the separation d, can be obtained as:

$$K_n(d) = \frac{F_d(d)}{d} \tag{3.9}$$

3.2.3 Dimensionless Equations

It's essential to notice that it doesn't exist an analytic solution for eqs. 3.2, 3.7, 3.8, and it's therefore necessary to use a numerical solver. To avoid recurring to a numerical solver at each point, the Greenwood-Williamson method can be written in its dimensionless form. The dimensionless asperity peak height z^* and the dimensionless separation d^* can be expressed as:

$$z^* = \frac{z - \bar{z}}{\sigma_z} \tag{3.10}$$

$$d^* = \frac{d - \bar{z}}{\sigma_z} \tag{3.11}$$

This allows to rewrite eqs. 3.2, 3.7, 3.8 as:

$$\mathrm{N}_d^* = \mathrm{N}_0 f_0(d^*) \tag{3.12}$$

$$\mathrm{A}_d^* = \pi \mathrm{N}_0 \rho \sigma_s f_1(d^*) \tag{3.13}$$

$$\mathrm{F}_d^* = \frac{4}{3} \mathrm{N}_0 \mathrm{E}^* \sqrt{\rho} \sigma^{3/2} f_{3/2}(d^*) \tag{3.14}$$

where

$$f_n(d^*) = \int_d^{\infty} \phi^*(z^*)(z^* - d^*)^n dz^* \tag{3.15}$$

$$\phi^*(z^*) = \frac{1}{\sqrt{\pi}} e^{-\frac{1}{2z^{*2}}} \tag{3.16}$$

An example of a contact case calculated with dimensionless variables is shown in fig. 3.8 where, from left to right, are traced the dimensionless number of asperities N_d^*, contact area A_d^*, and normal contact force F_d^*

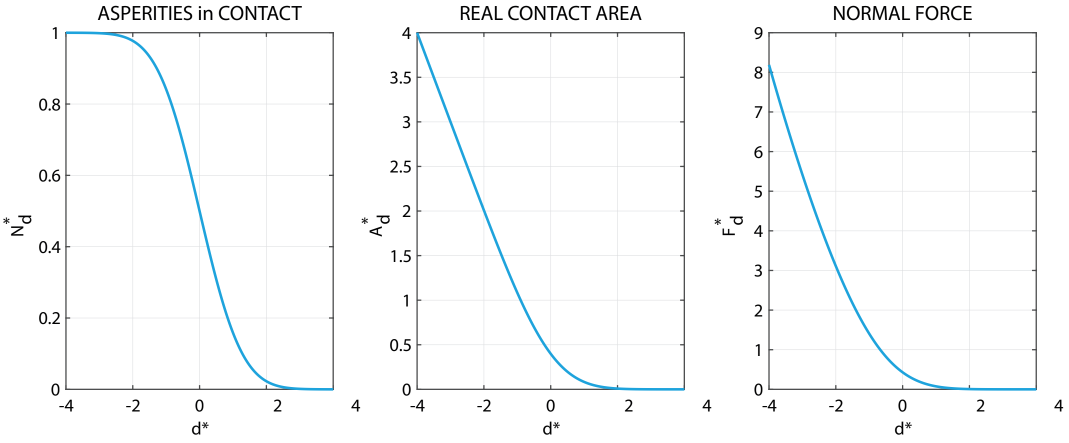

Figure 3.8 – Evolution of dimensionless number of asperities in contact (left), true contact area (center), and normal force (right)

3.2.4 Surface statistical properties determination

The described method requires the knowledge of some surfaces parameters:

- $\bar{z}$: the average asperity peak height;
- σ_z: the standard deviation of the asperity peak height;
- ρ: the average asperities radius;
- N_0: the total number of asperities **or** the asperity peak density η.

Their calculation is subjected to several approaches [48, 34, 38, 43, 23], but for each of them it's necessary to have the height profile of the surface — or at least a part of it — obtained thanks to 2D or 3D topography.

Another aspect to take into account is that the Greenwood-Williamson model assumes that the first surface is perfectly smooth, while the second one is rough, but in reality we have two rough surfaces. Therefore the question is: how do we adapt a rough-rough system to the GW smooth-rough system? The solution is to measure the statistical properties for both the rough surfaces and then combine them in order to obtain the GW model parameters in the following way:

- the average asperity peak height $\bar{z}$ is obtained as the sum of the average of the surfaces

$$\bar{z} = \bar{z}_1 + \bar{z}_2 \tag{3.17}$$

- the asperity peak height standard deviation σ_z is obtained as the quadratic sum of the standard deviation of the two surfaces

$$\sigma_z^2 = \sigma_{z,1}^2 + \sigma_{z,2}^2 \tag{3.18}$$

- The total number of asperities N_0 is chosen as the maximum between the two surfaces:

$$N_0 = max(N_{0,1}, N_{0,2}) \tag{3.19}$$

3.2.5 Extensions and Alternatives

There are two main categories of models for rough contacts: analytical and numerical. The first analytical model is the GW model [20], which is based on the concept of asperities. Since then, researchers have tried to modify it in order to overcome its limiting hypotheses or to find alternative ways to calculate the normal contact between rough surfaces. For example, extensions of the GW model were developed by Bush et al. [10], who considered elliptical paraboloidal asperities; McCool et al. [33], who treated anisotropic surfaces with a random distribution of asperity peak radii; Chang et al. [13], who introduced plasticity.

A particular extension , which is actually a simplification of the GW model, is represented by the work of Polycarpou [44]. It consists in replacing the asperities peak-height normal distribution $\phi(z)$ of eq.3.1 with an exponential one $\phi^*(z)$:

$$\phi^*(z) = ce^{-\lambda z} \tag{3.20}$$

where c and λ are constant coefficients. By using the exponential distribution of eq.3.20, the contact eqs. 3.2, 3.7, 3.8 become the following closed form set of equations:

$$\begin{aligned} N_d &= \frac{c\eta A_n}{\lambda} e^{-\lambda d^*} && (3.21) \\ A_d &= \frac{c\pi\beta A_n}{\lambda^2} e^{-\lambda d^*} && (3.22) \\ F_d &= \frac{c\sqrt{\pi}\beta E^* A_n}{\lambda^{5/2}} \left(\frac{\sigma_z}{\rho}\right)^{1/2} e^{-\lambda d^*} && (3.23) \\ & && (3.24) \end{aligned}$$

where A_n is the nominal contact area and $\beta = \eta\rho\sigma_z$ is a roughness parameter in which η is the asperities density. Fig. 3.9 shows a comparison of the contact force calculated as a function of the dimensionless separation d^* with GW and Polycarpou methods, for different values of c and λ. Based on the choice of parameters, one can choose to better approximate the low, middle or high range of contact normal force.

A new approach was developed by Persson [40], which moved away from the asperity concept.

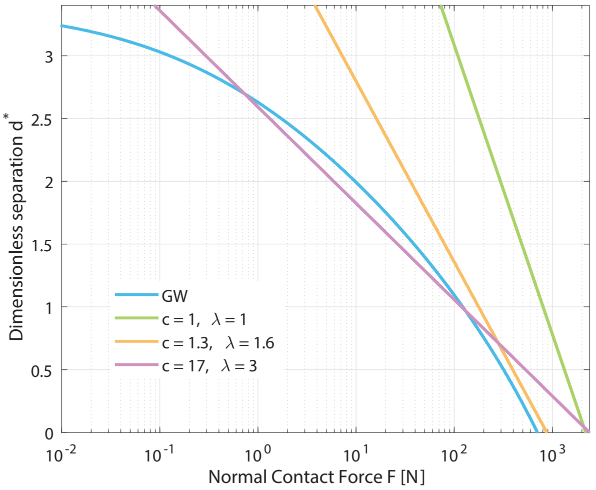

Figure 3.9 – Comparison of Greenwood-Williamson model with Polycarpou approximation for different values of c and λ parameters

Furthermore, an interesting comparison of analytical models is carried out in the work of Carbone and Buttiglione [12].

Moving to numerical models, these are based on FEM simulations and the most successful methods can be found in [21, 39, 11, 45]. An extensive comparison table between the different methods is shown in [60].

The further development of the initial Greenwood model and the contribution of newly developed methods has been crucially important in the task of better understanding the contact between two rough surfaces. However, newer methods are usually theoretically and computationally more expensive. It's universally recognized that, even if the initial Greenwood-Williamson theory makes heavy assumptions, it remains an excellent trade-off between ease of use and results reliability. Therefore, considering that the objective of this chapter is to build a connector system for dynamic time simulations, it's important to have a simple but still reliable method to predict the normal force in the contact between the different components of a bolted joint. Therefore, the Greenwood-Williamson original method is used, with the adaptations of eqs. 3.17, 3.18, 3.19.

3.3 Tangential Stiffness Calculation

In the previous section — in eq. 3.9 — we have seen how to calculate the nonlinear normal contact stiffness K_n as a function of the separation d between the surfaces. The next step is to determine the tangential stiffness, that will be later used as the starting point to model the friction behavior.

Experimentally, the normal and tangential stiffness of the contact between two bodies pressed on each other can be measured by using ultrasonic waves [24, 37]. The idea is that a wave is generated in the first body and the impulse passing in the second body through the contact interface is measured. According to the direction of the ultrasonic impulse, the normal or the tangential stiffness is measured. However, the contact interface stiffness does not only depend on the contact area, which makes it difficult to trace it back to an analytical contact model [24]. Concerning analytical ways to determine the tangential stiffness, the literature on this subject clearly states that it can be calculated from the value of the normal stiffness and that it only depends on the Poisson ratio ν [35, 20, 26]. A series of methods to calculate the tangential stiffness K_t can be summarized by the following expression:

$$K_t = \lambda \left(\frac{1-\nu}{2-\nu} \right) K_n \tag{3.25}$$

where K_n is the contact normal stiffness and λ is a constant coefficient. In Table 3.1 are shown the values of λ according to several authors. Note that for the Baltazar model [18], ξ and κ are correction factors taking into account the geometrical misalignment respectively for shear and longitudinal directions. Experimental measurements performed by Gonzalez et al. [18] have shown that the ratio between normal and tangential contact stiffness is not constant but it depends on the normal pressure, on the surface statistical parameters, and on the number of cycles performed.

Fig. 3.10 shows a comparison between the trends of experimental tests performed in [18], which are used as a benchmark, and the different models listed in Table 3.1, for a Poisson ratio $\nu = 0.3$. Concerning Baltazar model, the two correction factors were taken as $\xi = 0.65$ and $\kappa = 1$. It can be observed that the methods for which the experimental trends are best approximated are the Sherif and Baltazar approaches. Conversely, Mindlin and Yoshioka respectively overes-

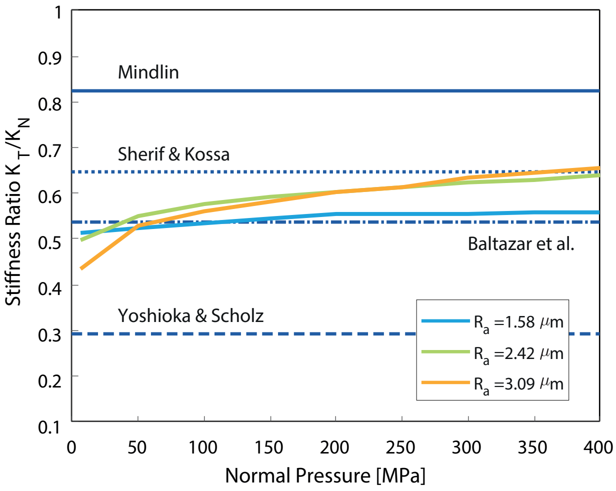

Figure 3.10 – Comparison of different approximation of tangential stiffness with experimental benchmark data

Method	λ
Mindlin (1949) [35]	2
Yoshioka and Scholz (1989) [61]	0.71
Sherif and Kossa (1991) [54]	$\pi/2$
Baltazar et al. (2002) [5]	$2\xi/\kappa$

Table 3.1 – Values of the λ parameter according to different authors

timate and underestimate the stiffness ratio.

It's worth noting that more recently Raffa et al. [46] have developed a spring-like micro-mechanical contact model for normal and tangential stiffness, which successfully follows — for the studied case — the experimental evolution of the stiffness ratio. For our purpose, which is to find the initial tangential stiffness in no-sliding condition in order to insert it in the Dahl friction model, Sherif's method have been considered.

Once having described how the contact is treated, it's now time to illustrate how the bolted joint modeling connector has been built.

3.4 The Connector System

In this section the developed connector system will be defined in its entirety, then carefully broken down and detailed into all of its different components. Fig. 3.11 shows the reference bolted-joint with its general geometrical dimensions that will be used throughout the design process.

Bolt:

- d : nominal diameter
- l : bolt length
- l_d : shank length
- l_t : engaged thread length

Joint:

- t_1 : thickness plate 1
- t_2 : thickness plate 2
- d_h : hole diameter
- $d_{w,e}$: washer ext diameter
- t_w : washer height
- l : grip length
- j : bolt-hole clearance

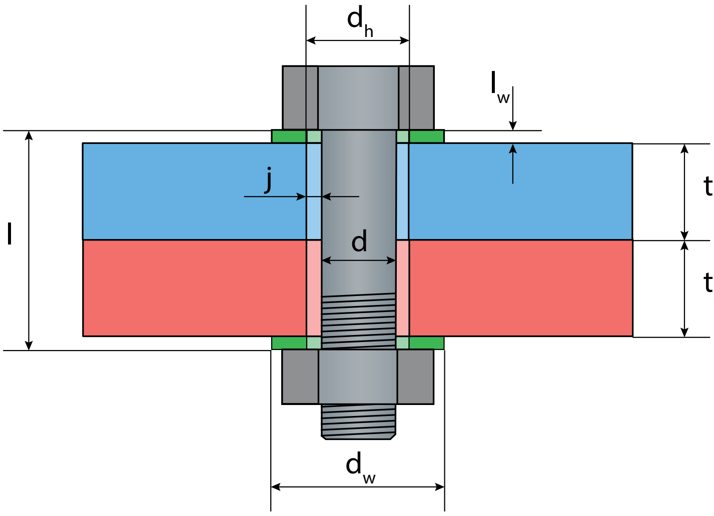

Figure 3.11 – General bolted joint dimensions

3.4.1 Overview

The first step to build the connector system is, of course, to remove all the movable components of the joints which, in a standard case, are bolts, nuts and washers. Once this has been done,

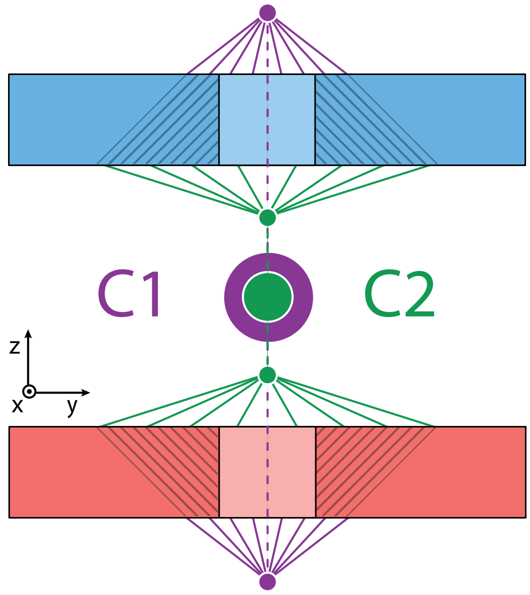

Figure 3.12 – Connector system diagram

the parts can be assembled using the connector system, as shown in Fig. 3.12. It consists of two different connectors: the first one, named C1, links the upper surfaces of the plates. The second, named C2, links the surfaces at the contact interface. The bolted joint interface lies on the x-y plane, while the axial hole direction defines the z-axis. The main features of the two connectors can be summarized as follows:

- **Connector C1**:
    - The two connected virtual nodes are linked to the respective annular surfaces around the upper and lower plates holes.
    - Modeling of the axial stiffness is determined by the bolt, nut, washer and their normal contact with the respective plates.
- **Connector C2**:
    - The two connected virtual nodes are linked to the respective annular surfaces around the plates holes at the contact interface. The size of this area depends on the Rotscher's cone angle α.
    - Modeling of the axial contact stiffness is based on the surface properties.
    - Modeling of the tangential frictional behavior between the two plates in the x-y plane.

It's important to clarify how the C1 and C2 connectors nodes are linked to the respective annular surfaces. In fact, the connection between these virtual nodes and the nodes of the annular surfaces is carried out with an rigid body element RBE3, represented in fig. 3.12 by a series of "spider web" lines. Note that, in reality, the position of the virtual nodes lies on the plane of the respective annular surface: for illustrative reasons was not possible to do that in fig. 3.12. Furthermore, please pay attention to the area filled with a line pattern in fig. 3.12 around the plates holes: this represents the Rotscher cone (see section 2.1.2).

3.4.2 Connector C1

The task of the C1 connector is to model the axial behavior of the movable parts of the joint. This will make it possible to impose the bolt preload in the connector.
Fig. 3.13 shows a diagram of the axial modeling of connector C1. It can be observed that the different components can be represented as series of linear and nonlinear springs. Imagine starting from the upper surface of the blue plate in the bolted joint model of fig. 3.14: the first part in contact with it is a washer, then the washer is in contact with the bolt. If we follow the bolt till the nut, this will be in contact with the second washer and finally this is in contact with the bottom of the red plate. It can therefore be understood how the diagram in fig. 3.13 represents the stiffnesses from the top of the blue plate and the bottom of the red plate, evidenced by the smaller dimensions of the Rotscher cone.
Analyzing the single stiffnesses it's possible to distinguish:

- K_b: Bolt stiffness;
- $\mathrm{K}_{\mathrm{NL},1}$,$\mathrm{K}_{\mathrm{NL},2}$: Nonlinear contact stiffness between plate and washers — or bolt and nut if there are no washers;
- $\mathrm{K}_{w,n}$: stiffness of the n^{th} washer.

The total axial stiffness of C1 connector can then be calculated as:

$$\mathrm{K}_{\mathrm{C1}} = \left(\frac{1}{\mathrm{K}_b} + \sum_{i=1}^{n_w} \frac{1}{\mathrm{K}_{w,i}} + \frac{1}{\mathrm{K}_{\mathrm{NL},1}} + \frac{1}{\mathrm{K}_{\mathrm{NL},2}} \right)^{-1} \tag{3.26}$$

Let's see how each stiffness is calculated.

3.4.2.1 Bolt stiffness calculation

The bolt stiffness K_b is obtained using a traditional linear approach [9], which defines it as the resultant stiffness of two springs in series, representing the threaded and unthreaded part of the bolt shank (see fig.3.14). The total bolt stiffness can be expressed as:

$$\mathrm{K}_b = \frac{k_u k_t}{k_u + k_t} = \frac{\mathrm{A}_u \mathrm{A}_t \mathrm{E}}{\mathrm{A}_u l_u + \mathrm{A}_t l_t} \tag{3.27}$$

where A_u is the unthreaded shank section area, while A_t is the threaded tensile stress area, which can be found in dedicated tables.

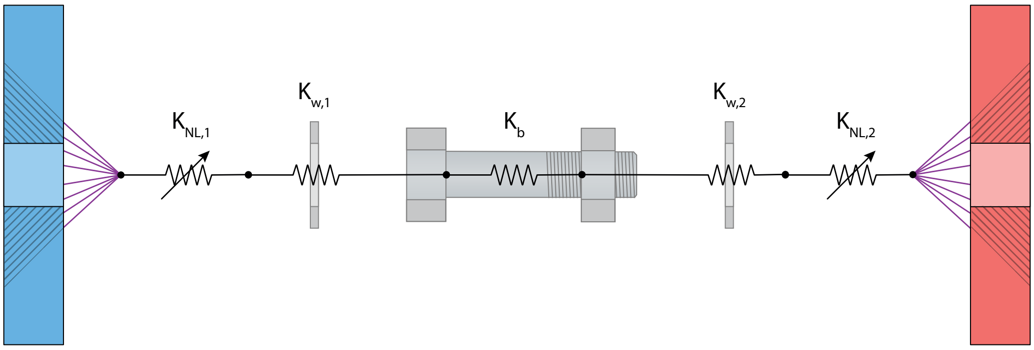

Figure 3.13 – Axial nonlinear stiffness of the connector C1

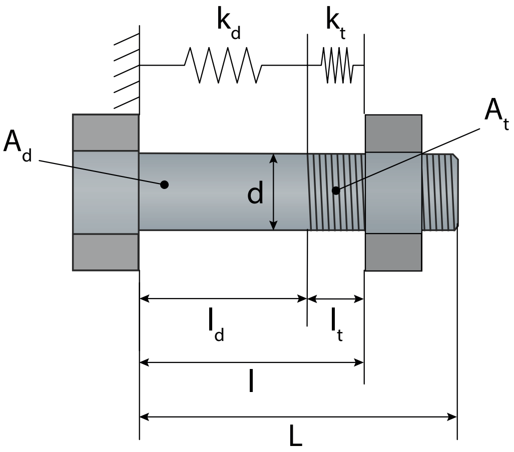

Figure 3.14 – General bolt dimensions

3.4.2.2 Washer stiffness calculation

The washer stiffness K_w, whose dimensions are shown in fig. 3.15, is simply calculated as:

$$K_w = \frac{\pi\left(d_{w,e}^2 - d_{w,i}^2\right)E}{4t} \tag{3.28}$$

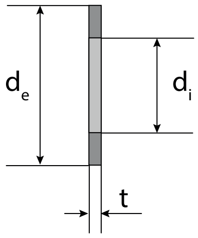

Figure 3.15 – General washer dimensions

3.4.2.3 Contact stiffness calculation

The nonlinear contact stiffnesses $K_{NL,1}$ and $K_{NL,2}$ are obtained with the Greenwood-Williamson method described in section 3.2 by taking into account the surface profile of the plate. On this matter, there is a small detail that has to be clarified. The C1 connector links two virtual nodes that, in turn, are linked to the respective annular surfaces through an RBE3 element. The goal for the C1 connector is to find the nonlinear contact force as a function of the nodes *relative displacement*, but for the Greenwood-Williamson model, the *separation* between the surfaces is used as a parameter. Therefore, it's necessary to determine the separation corresponding to the *zero* relative displacement. This initial separation is chosen as four times the value of the asperity peak-height standard deviation σ_z, for which the normal force can be approximated to zero.

The size of the nominal contact area is determined by the annular area whose smaller diameter is the hole diameter and the larger one is defined by the bolt head or washer.

The obtained nonlinear curves are then used to calculate the resulting total axial stiffness K_{C1} with eq. 3.26. Since there is no closed form for the solution of Greenwood-Williamson model,

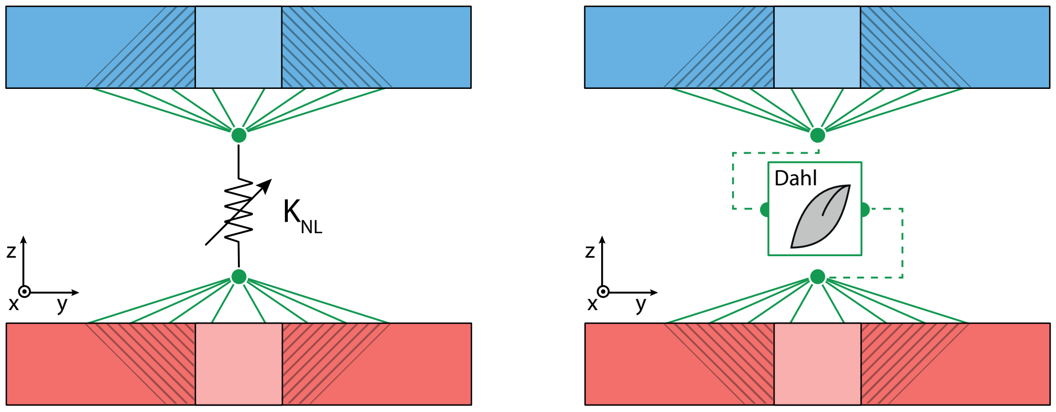

(a) Axial

(b) Tangential

Figure 3.16 – C2 connector axial (right) and tangential (left) diagram

the total nonlinear curve is calculated only once, then discretized and finally entered as a connector input.

3.4.3 Connector C2

The C2 connector is the most interesting part concerning the damping induced by bolted joints. The task here is to model both the normal and tangential contact behavior at the interface of the bolted joint.

3.4.3.1 C2 Axial Stiffness

The normal contact at the interface is again modeled through Greenwood-Williamson. In this case, some details have to be provided in order to determine the nominal contact area A_n. In fact, the latter depends on the angle of the Rotscher's cone, which is usually exploited to analytically determine the joint member stiffness. A small digression is needed in order to give more details about the calculation of the joint stiffness.

Determination of joint stiffness. For our purpose it's not necessary to calculate the joint stiffness, but the process that leads to it it's necessary in order to determine the nominal contact area to use in the GW model. Let's consider a preloaded bolted joint (see the FEM preload simulation in 2.1.2): the jointed components will be subjected to a certain stress in a frustum shaped zone.
Rotscher [47] assumed that the stress in this region is constant, taking a frustum cone angle $\alpha = 45°$ and replacing it by a cylinder with the same sectional area. Then, Shigley and Mischka [9] assumed that the stress inside the frustum varies, but only in the direction perpendicular to the bolt axis, and they used values of the cone angle from $\alpha = 30°$ to $\alpha = 45°$. Also, Motosh [36] derived an analytical solution for the stress varying in both direction. Finally, Wileman et al. [58] performed a series of FEM simulations in order to compare the different models.
Fig. 3.17 shows a comparison of different methods for the calculation of the joint stiffness. It can be observed that the Shigley's method with an angle $\alpha = 30°$ is the one that better approximate the FEM results by Wileman. Therefore an angle $\alpha = 30°$ is the one chosen for the connector. In this way, the external diameter of the annular surface can be obtained as:

$$d_{C2} = d_{w,e} + t \tan\alpha \tag{3.29}$$

with d_w being the washer diameter and t the thickness of the single plate. In case the washer doesn't exist, d_w is replaced by the bolt head or nut radius.
The diameter obtained in eq. 3.29 is used to calculate the nominal contact area for the axial and tangential behavior of the C2 connector.

3.4.3.2 C2 Tangential Behavior

The goal of this part of the connector is to describe the frictional behavior of the bolted joint. A Dahl dynamic friction law, introduced in section 2.2.2.1 is implemented in the two directions x and y. Dahl's model applied to the connector in the x-direction becomes:

$$\frac{d\mathrm{F}_{\mathrm{D},x}}{dx} = \mathrm{K}_t(t)\left(1 - \frac{\mathrm{F}_{\mathrm{D},x}}{\mu\mathrm{F}_z(t)}\frac{\dot{x}}{|\dot{x}|}\right)^{\alpha} \tag{3.30}$$

where:

- $\mathrm{F}_{\mathrm{D},x}$: tangential Dahl force in x-direction;
- $x, \dot{x}$: displacement and velocity between connector nodes in the x-direction;
- $\mathrm{F}_z(t)$: normal force, derived from GW model (see section 3.2);
- $\mathrm{K}_t(t)$: tangential stiffness, deriving from the combination of GW and Sherif (see section 3.3);
- α: coefficient determining the transition between micro-slip and macro-slip, chosen as $0 < \alpha \leq 1$;
- μ: friction coefficient, considered constant.

Considering the range of values of α, the term inside parentheses

$$\mathrm{C} = 1 - \frac{\mathrm{F}_{\mathrm{D},x}}{\mu\mathrm{F}_z(t)}\frac{\dot{x}}{|\dot{x}|} \tag{3.31}$$

can't be negative. When this happens, macro-slip occurs and the force is automatically set to be $\mathrm{F}_{\mathrm{D},x} = \mu\mathrm{F}_z(t)$), which is the friction limit.

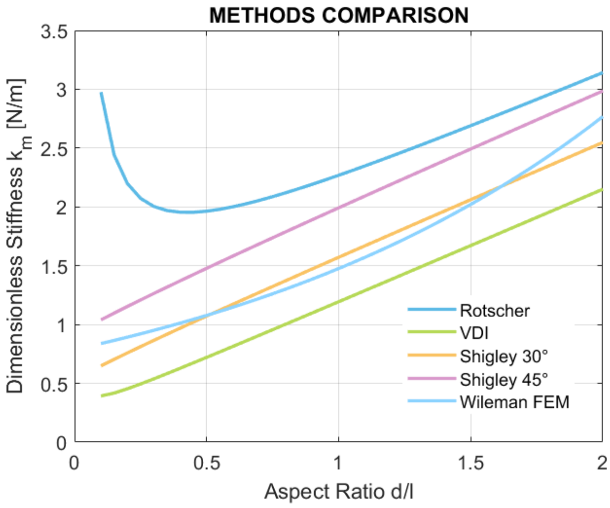

Figure 3.17 – Comparison of dimensionless joint stiffness comparison calculated with different methods

In section 2.1.3 we have seen that, beside the micro-slip and macro-slip phases, there is also a third phase called *pinning*, which takes place when the bolt comes into contact with the bolt-hole. To model this behavior, a control on the connector displacements x and y has been added. Knowing that j is the bolt-hole clearance, if:

$$d = \sqrt{x^2 + y^2} \geq j \tag{3.32}$$

then:

$$\mathrm{F}_x = \mathrm{F}_{\mathrm{D},x} + \mathrm{K}_p \frac{x}{d} \tag{3.33}$$

$$\mathrm{F}_y = \mathrm{F}_{\mathrm{D},y} + \mathrm{K}_p \frac{y}{d} \tag{3.34}$$

where K_p is the pinning or bolt-hole contact stiffness. Hence, if the combined displacement of the two connectors is larger than the clearance, an additional contact force is added to the Dahl forces $\mathrm{F}_{\mathrm{D},x}$ and $\mathrm{F}_{\mathrm{D}_y}$. A sample Dahl cycle with macro-slip limit on the force and pinning is provided in fig. 3.18

3.4.4 Preload Application

After having described all the ingredients inside the connector, it's now time to understand how the bolt preload is applied before performing the time simulations.
Once defined the numerical value of the preload to apply, the initial working point of the connector system is found on the nonlinear axial curves derived for the two different connectors C1 and C2. Fig. 3.19 shows an example of the nonlinear force-displacement curves and their discretization, together with the initial working point found by interpolating the curves with the desired preload value. In the next section the numerical implementation in the SDTools software will be treated and the results obtained with the connectors on the ORION mock-up (see section 1.5) will be compared to experimental tests.

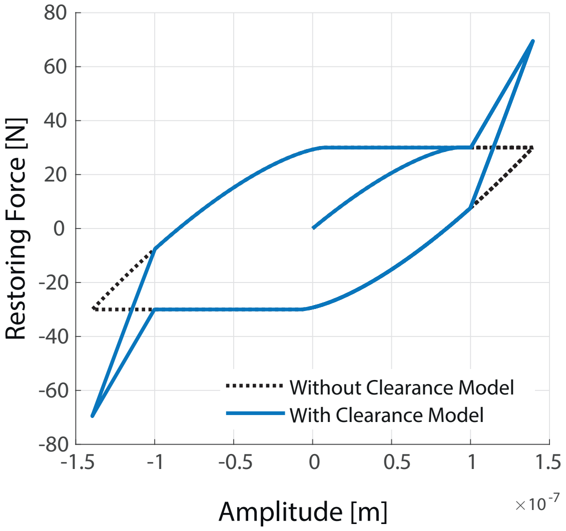

Figure 3.18 – Example of hysteresis cycle implemented in the C2 connector. α=0.3.

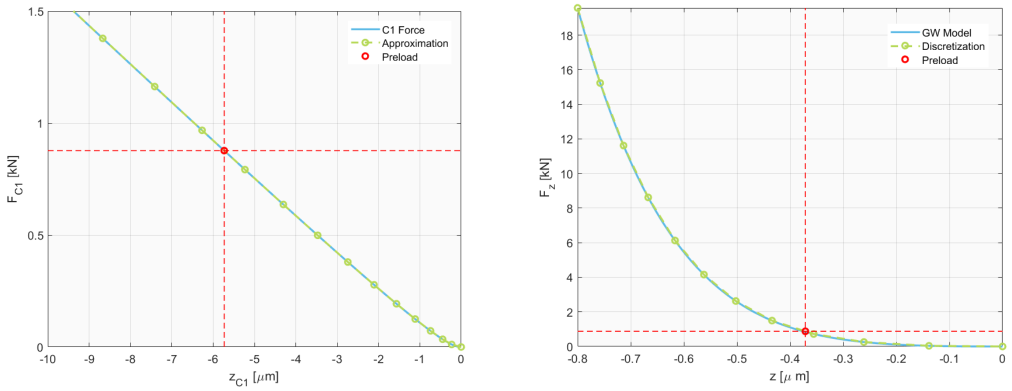

(a) Connector C1

(b) Connector C2

Figure 3.19 – Preload application to the connectors

3.5 Implementation of the connector system

The implementation of the connector has been carried out in the SDTools software, which is a MATLAB® based structural dynamics toolbox. Considered that the implementation task was assigned to the SDTools developers, the methods employed will be described without going into great depth. Then, the obtained results will be commented in order to understand if the connector system can model bolted joints with an acceptable degree of precision and what are its advantages and disadvantages.

3.5.1 Objective

Before starting to describe the implementation of the connector system in SDTools let's take a look to the chosen test case. Considered the practical interest of the connector system, it's important to test it on a real structure of which accurate experimental data are available. In addition, the structure has to be simple enough to be able to focus on the connectors' behavior and to spot possible qualities and flaws. The chosen structure is the ORION mock-up (see section 1.5.1), for which a complete test campaign has been performed by the FEMTO-ST lab.
The ORION mock-up is assembled through three M4 bolts: during the tests the center bolt is pre-loaded with a constant force of 876N, while for the other two bolts the preload is changed between four different values (136N, 261N, 385N, 876N). The preload of the bolts is precisely measured by innovative sensors produced by Texense, directly implemented in the bolts head. A particularly nonlinear flexion mode was identified and studied by exciting the structure with a shaker at several amplitude levels and by testing different bolt preloads.
Figures 3.20b-fig. 3.20a respectively shows the shape of the chosen mode and the experimental FRFs obtained by exciting the structure with a swept sine around its natural frequency. The same line color — and shades — represents the same preload applied to the external bolts, the same line style represents the same excitation amplitude imposed to the structure. The bolt preload is expressed in cNm, while the excitation amplitude in mN. It can be noted that the typical nonlinear behavior of bolted structures outlined in section 2.1.4 is reproduced here by the experimental results. The intention is now to see if the use of the connector system, whose parameters are determined by the physical dimensions and data available from the ORION mock-up, can reproduce the experimental results.

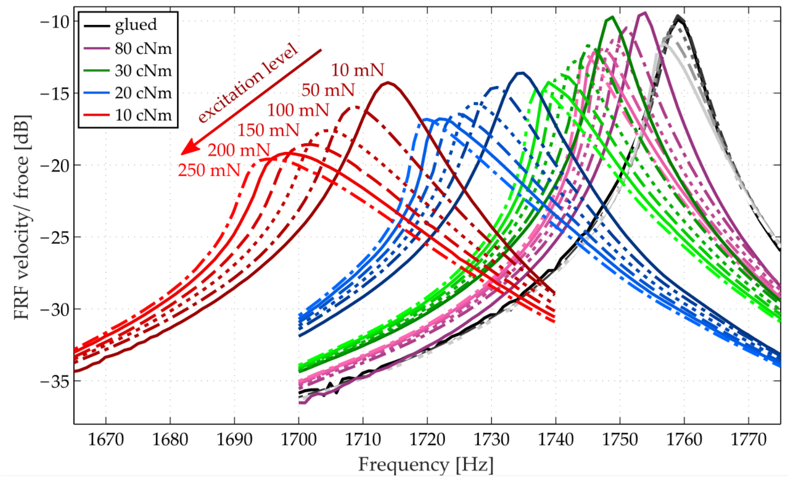

(a) FRF variations according to excitation amplitude and external bolts preload

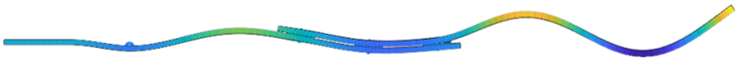

(b) Nonlinear selected flexion mode

Figure 3.20 – Experimental results on the ORION mock-up

3.5.2 Implementation

The connector system developed in this chapter was implemented on the ORION mock-up finite element model, as it's shown in fig. 3.21. The virtual nodes of the different connectors are linked to their respective surface through rigid body elements of type RBE3, that generates a distributed coupling. The RBE3 connections are represented by the yellow spider webs in fig. 3.21.

The connector parameters are determined according to the data available on the structure, and the preload force is applied with the procedure described in section 3.4.4.

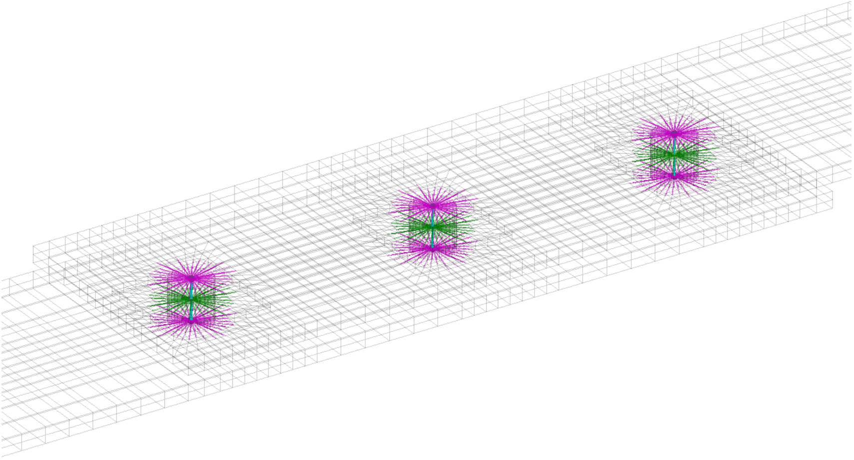

Figure 3.21 – Implementation of the developed connector on the ORION mock-up

As previously stated in this chapter, the simulations are carried out in the time domain. The nonlinear modal Newmark algorithm developed by SDTools allows a fast calculation of the nonlinear FRFs by using the stepped sine technique: at each frequency step the stabilized steady-state response is calculated to obtain amplitude and phase.

3.5.3 Results

The structure with the implemented connectors has been tested with the parameters taken from the physical properties, and the Dahl parameters justified by the relation with the Mindlin contact theory (see section 2.2.5). In particular, Dahl exponent was taken as $\alpha = 0.33$.
The FRF of fig. 3.22 was numerically calculated on the structure with connectors. However, there is a clear problem with this FRF: in fact, the transition between micro-slip and macro-slip is too quick and the result is a flat FRF in the vicinity of the resonance. If we extend this study at several amplitudes it's possible to see that it's impossible to detect a frequency shift as shown by the experimental results. The quick transition is probably due to the fact that the α parameter is less than 1.

In order to investigate this problem, several combination of α parameter and friction coefficient μ are tested, trying to reproduce the frequency and damping shift highlighted by the experimental results. Fig. 3.23 shows some examples of this process: on the left are shown the numerically obtained FRF, while on the right the shapes of Dahl steady-state cycle. These results show that it's indeed possible to obtain a nonlinear evolution of frequency and damping with the excitation amplitude and the bolt tightening torque. However, compared to the real structure, the shift is too weak for the natural frequency and too strong for the damping. It was not possible to find a set of parameters able to reproduce the frequency and damping shift of the experiments.

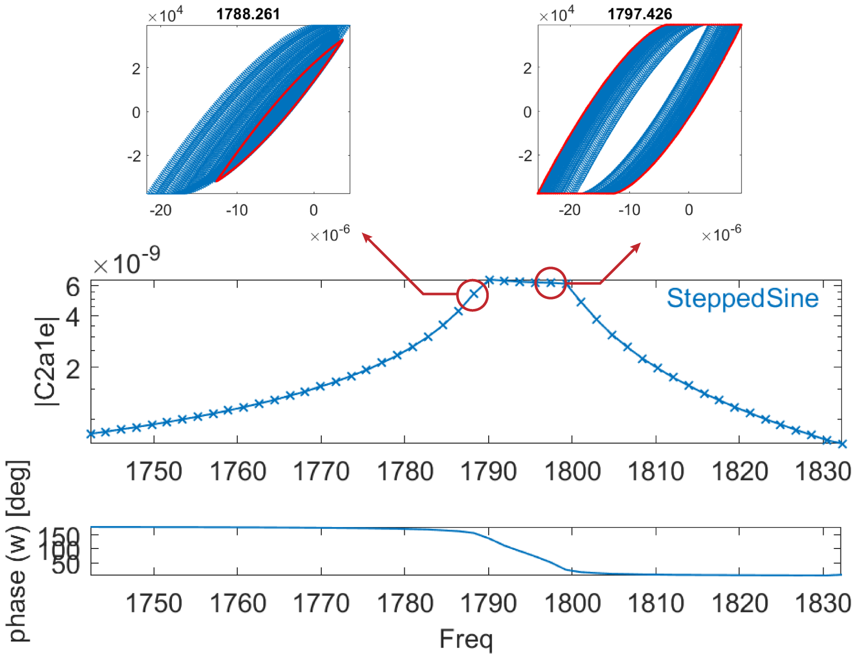

Figure 3.22 – Example of FRF numerically calculated through the stepped sine technique with Dahl parameters deriving from theory

Further investigation on this aspect is provided. Since the frequency and damping shift depends on the contact evolution implemented in the connector system, the necessary evolution will be found in order to fit the experimental data, and to find the flaws in the system. In order to do this, the theoretical evolution of the tangential stiffness K_t — and therefore of the normal stiffness K_n too, since they are related (see section 3.3)— is *reversely engineered* to understand the limits of the connector system. Fig. 3.24 shows the evolution of the natural frequency — on the left — and of the ratio $\log_{10}\left(K_{t,T}/K_{t,80}\right)$ — on the right — as a function of the excitation amplitude and bolt tightening torque. $K_{t,80}$ and $K_{t,T}$ are the values of the tangential stiffness

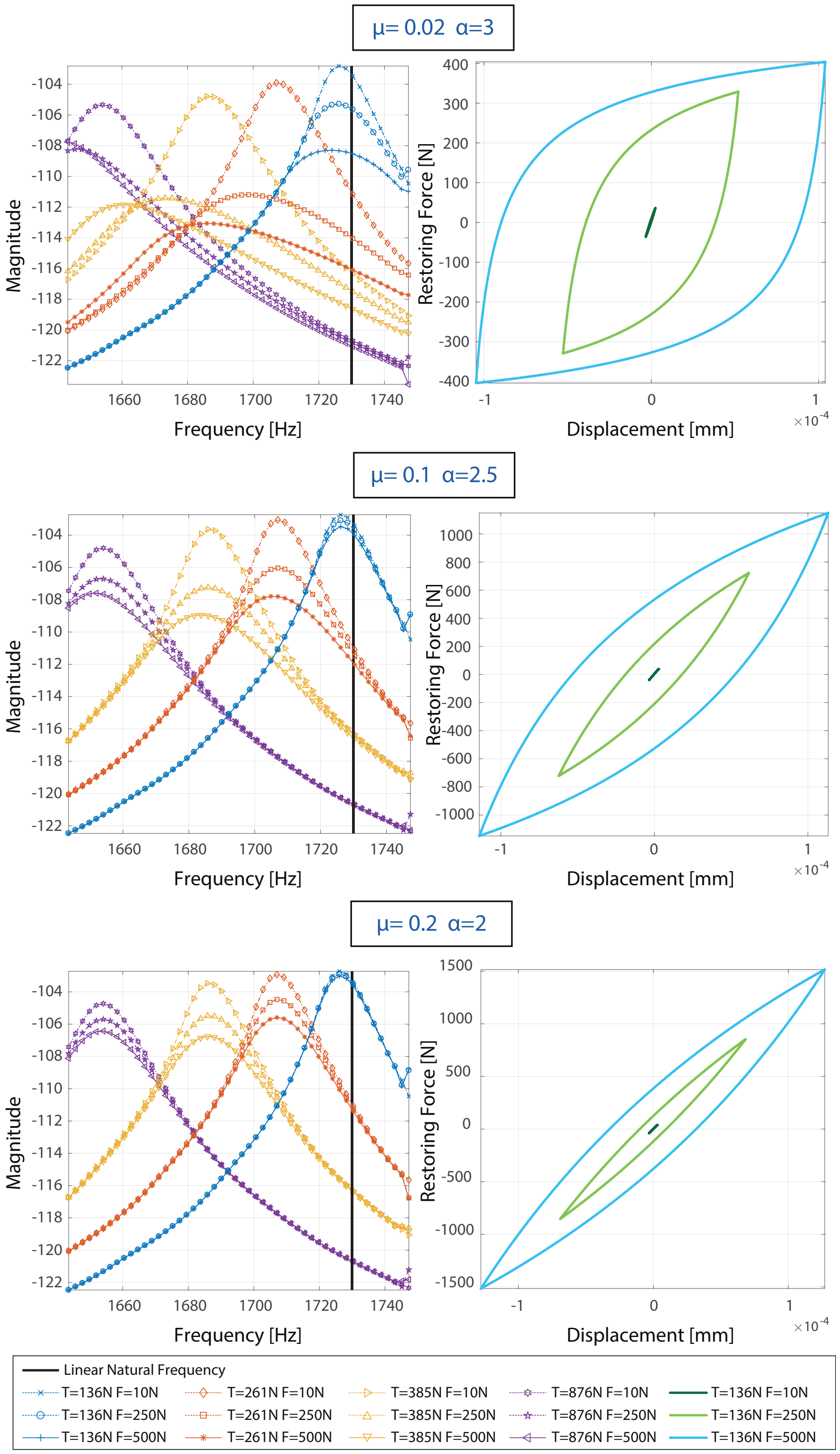

Figure 3.23 – Example of FRF numerically calculated through the stepped sine technique with Dahl parameters derived from theory

for the maximum preload of 80cNm, and for the general tightening torque T. According to the right chart of fig. 3.24, considering for example an excitation amplitude of 150mN, it's necessary for the maximum stiffness $K_{t,80}$ to be about 10^2 times larger than the tangential stiffness at minimum preload $K_{t,10}$.

We can compare the necessary value of the ratio with the actual one by looking at fig. 3.25.

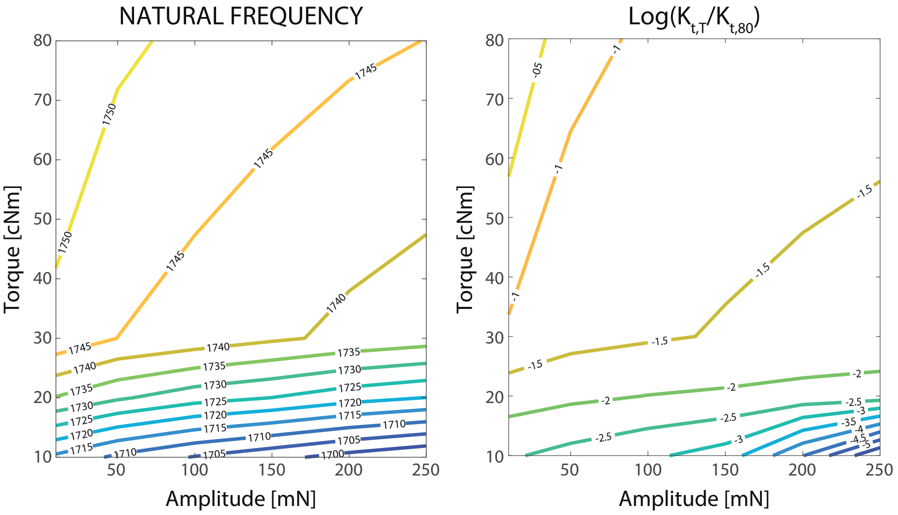

Figure 3.24 – Natural frequency and stiffness ratio contour map as functions of the input force amplitude and tightening torque.

The latter shows that the actual ratio is slightly larger than 2, which is much lower than the necessary one to fit the experimental results. This value is very little influenced by the surface parameters chosen for the Greenwood-Williamson model implemented in the connector.

The root cause of this difference is probably to search in the nature of contact modeling. The proposed approach through the connector is a local approach, in which the contact pressure distribution is constant and managed by the RBE3 elements linking the virtual nodes to their respective surfaces. In addition, the contact law implemented in the connector only considers the areas around the bolt holes. However, when facing a dynamic problem, the contact pressure distribution will change in time and can interest also areas that are far from the bolt.

The large difference between the necessary stiffness ratio and the one provided by the contact model is therefore probably due to the fact that the contact law implemented in the connector can only described a uniformly distributed and static contact situation. Energy dissipation contributions coming from an irregular contact pressure distribution in the designed contact areas and in other areas where no modeling was provided, can't be taken into account with the current model.

3.6 Conclusion and Perspectives

In this chapter a model of bolted joint made of a connector system was developed, and a description of its different components was provided. Then, the nonlinear laws implemented in the connector were described. Finally, the results of the connector system implementation on the ORION mock-up in the SDTools environment were displayed and discussed. It was shown that, even if the developed connector system was able to qualitatively reproduce typical bolted joints nonlinearities, quantitatively the frequency shift was under-estimated and the damping shift was over-estimated.

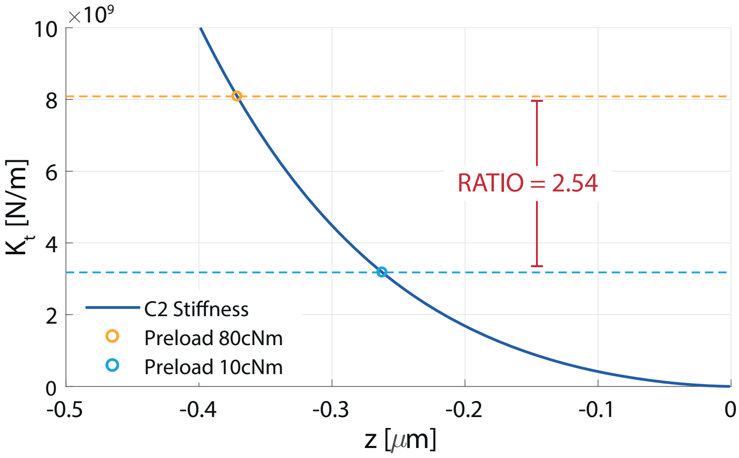

Figure 3.25 – Visualization of the tangential stiffness ratio between maximum and minimum tightening torque

The causes of this inaccuracy can be identified as the following two:

- the assumption of uniform contact pressure distribution in the areas where the contact is modeled with connectors;
- the *dynamic* contact taking place in areas that are not interested by the connectors;

The first one is due the fact that, for an RBE3 connection, the effort on the virtual node is calculated by a weighted average of the efforts in the contact area, which will relate even a non-uniform distribution to a single number. The second one can be demonstrated with the help of high-detail numerical simulations of a contact surface. In section 2.3.4 a method to impose a mode displacement on a structure was developed. If the method is applied on a high-fidelity finite-element model taking into account the normal and tangential friction behavior at the contact interface, it's possible to determine where the energy is dissipated by looking at the relative displacement between the surfaces. Fig. 3.26 shows the location of the slip between surface at the interface of the BRB for the first three flexion modes. It can be observed that, in all of the modes, a considerable part of the energy dissipation takes place at the interface's borders, far from the bolt holes, due to the leverage effect of a plate on the other one.

From this simple example it's clear that knowing the dynamic evolution of the contact can be a big advantage to evaluate the dissipated energy and therefore the damping is of crucial importance.

A quick and instinctive solution could be to implement additional connectors in the areas where dynamic contact is presumed to take place. By using data from a series of high-fidelity model one could find a distribution of connectors and their respective parameters so that the contact can be fully described. Of course, the modeling effort required for such a distribution is much higher than the one required for the connector developed in this chapter.

Even if the latter is not able to precisely reproduce the experimental results of a structure, it remains a practical and versatile tool, thanks to its straightforward parameters determination process. Furthermore, the implementation doesn't require any modification to the structure, and the connector logic works well in the industrial field.

The connector system developed in this chapter can be used for cases in which the tightening torque is significant and where the dynamic excitation doesn't modify substantially the contact pressure distribution. It can also be practical in a preliminary analysis of jointed structure, since it allows the removal of the joints components (nuts, washers, bolts) from the FE model.

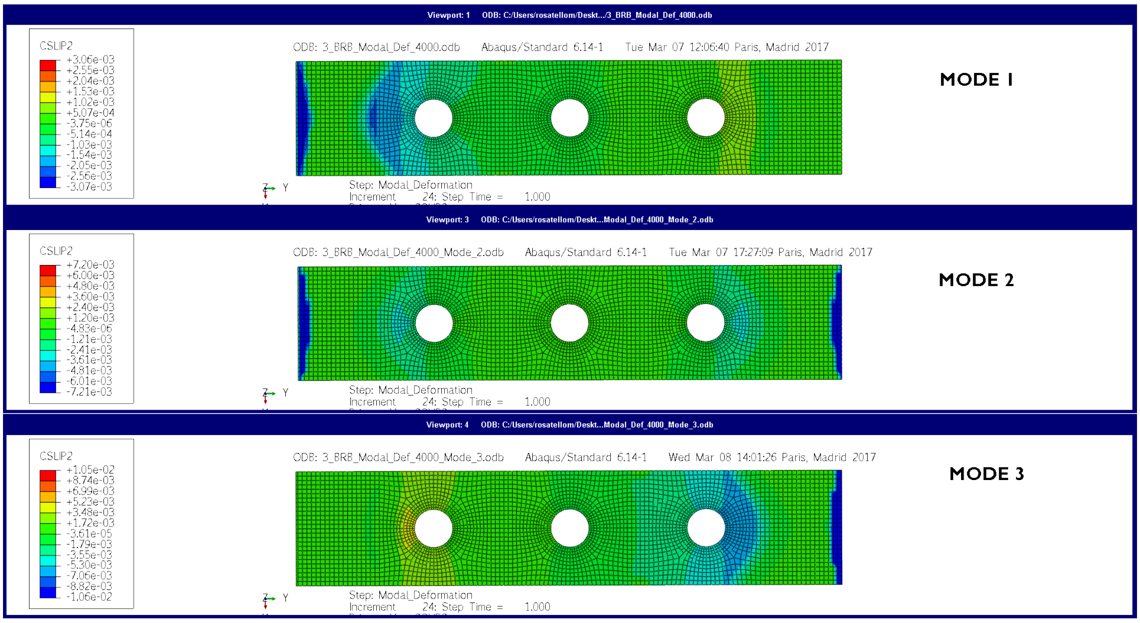

Figure 3.26 – Numerical high-fidelity simulations on the Brake-Reuss Beam imposing modal deformations. Slip at contact interface is maximum in deep blue areas, which are far from the bolt-holes.

Bibliography

[1] Ahmadian, H. and Jalali, H. (2007). Generic element formulation for modelling bolted lap joints. *Mechanical Systems and Signal Processing*, 21(5):2318–2334. 54

[2] Allen, M. S., Lacayo, R. M., and Brake, M. R. (2016). Quasi-static Modal Analysis based on Implicit Condensation for Structures with Nonlinear Joints. *Meccanica*, 51(12):3241–3258. 54

[3] Armand, J., Salles, L., Schwingshackl, C. W., Süß, D., and Willner, K. (2018). On the effects of roughness on the nonlinear dynamics of a bolted joint : A multiscale analysis. *European Journal of Mechanics*, 70(February):44–57. 52

[4] Askri, R., Bois, C., Wargnier, H., and Lecomte, J. (2016). A reduced fastener model using Multi-Connected Rigid Surfaces for the prediction of both local stress field and load distribution between fasteners. *Finite Elements in Analysis and Design*, 110:32–42. 51

[5] Baltazar, A. (2002). On the relationship between ultrasonic and micromechanical properties of contacting rough surfaces. *Journal of the Mechanics and Physics of Solids*, 50(7):1397–1416. 61

[6] Bampton, M. C. C. and Craig, JR., R. R. (1968). Coupling of substructures for dynamic analyses. *AIAA Journal*, 6(7):1313–1319. 54

[7] Bograd, S., Reuss, P., Schmidt, A., Gaul, L., and Mayer, M. (2011). Modeling the dynamics of mechanical joints. *Mechanical Systems and Signal Processing*, 25(8):2801–2826. 51, 54

[8] Brake, M. R. W. (2018). *The Mechanics of Jointed Structures*. Springer International Publishing, Cham. 51

[9] Budynas-Nisbett (2006). Mechanical Engineering : Shigley's Mechanical Engineering Design 8th Edition. page 1059. McGraw Hill. 64, 66

[10] Bush, A. W., Gibson, R. D., and Thomas, T. R. (1975). The elastic contact of a rough surface. *Wear*, 35(1):87–111. 59

[11] Campañá, C. and Müser, M. H. (2006). Practical Green's function approach to the simulation of elastic semi-infinite solids. *Physical Review B - Condensed Matter and Materials Physics*, 74(7):1–15. 60

[12] Carbone, G. and Bottiglione, F. (2008). Asperity contact theories: Do they predict linearity between contact area and load? *Journal of the Mechanics and Physics of Solids*, 56(8):2555–2572. 60

[13] Chang, W. R., Etsion, I., and Bogy, D. B. (1987). An Elastic-Plastic Model for the Contact of Rough Surfaces. *Journal of Tribology*, 109(2):257. 59

[14] Claeys, M., Sinou, J.-J., Lambelin, J.-P., and Todeschini, R. (2016). Experiments and numerical simulations of nonlinear vibration responses of an assembly with friction joints – Application on a test structure named "Harmony". *Mechanical Systems and Signal Processing*, 70-71(7):1097–1116. 55

[15] Desai, C. S., Zaman, M. M., Lightner, J. G., and Siriwardane, H. J. (1984). Thin-layer element for interfaces and joints. *International Journal for Numerical and Analytical Methods in Geomechanics*, 8(1):19–43. 54

[16] Festjens, H., Chevallier, G., and Dion, J. L. (2013). A numerical tool for the design of assembled structures under dynamic loads. *International Journal of Mechanical Sciences*, 75:170–177. 54

[17] Gaul, L. and Mayer, M. (2007). Efficient modelling of contact interfaces of joints in built-up structures. In *Computer Methods and Experimental Measurements for Surface Effects and Contact Mechanics VIII*, volume I of *WIT Transactions on Engineering Sciences, Vol 55*, pages 195–205, Southampton, UK. WIT Press. 55

[18] Gonzalez-Valadez, M., Baltazar, A., and Dwyer-Joyce, R. S. (2010). Study of interfacial stiffness ratio of a rough surface in contact using a spring model. *Wear*, 268(3-4):373–379. 61

[19] Gray, P. J. and McCarthy, C. T. (2010). A global bolted joint model for finite element analysis of load distributions in multi-bolt composite joints. *Composites Part B: Engineering*, 41(4):317–325. v, vi, 51, 52

[20] Greenwood, J. A. and Williamson, J. B. P. (1966). Contact of Nominally Flat Surfaces. *Proceedings of the Royal Society A: Mathematical, Physical and Engineering Sciences*, 295(1442):300–319. 55, 59, 61

[21] Hyun, S., Pei, L., Molinari, J. F., and Robbins, M. O. (2004). Finite-element analysis of contact between elastic self-affine surfaces. *Physical Review E - Statistical Physics, Plasmas, Fluids, and Related Interdisciplinary Topics*, 70(2):12. 60

[22] Johnson, K. L. (1985). *Contact Mechanics*, volume 37. Cambridge University Press, Cambridge. 57

[23] Kalin, M., Pogačnik, A., Etsion, I., and Raeymaekers, B. (2016). Comparing surface topography parameters of rough surfaces obtained with spectral moments and deterministic methods. *Tribology International*, 93:137–141. 59

[24] Kendall, K. and Tabor, D. (1971). An Ultrasonic Study of the Area of Contact between Stationary and Sliding Surfaces. *Proceedings of the Royal Society A: Mathematical, Physical and Engineering Sciences*, 323(1554):321–340. 60, 61

[25] Kim, J., Yoon, J.-C., and Kang, B.-S. (2007). Finite element analysis and modeling of structure with bolted joints. *Applied Mathematical Modelling*, 31(5):895–911. v, 50

[26] Królikowski, J. and Szczepek, J. (1993). Assessment of tangential and normal stiffness of contact between rough surfaces using ultrasonic method. *Wear*, 160(2):253–258. 61

[27] Lacayo, R., Pesaresi, L., Groß, J., Fochler, D., Armand, J., Salles, L., Schwingshackl, C., Allen, M., and Brake, M. (2019). Nonlinear modeling of structures with bolted joints: A comparison of two approaches based on a time-domain and frequency-domain solver. *Mechanical Systems and Signal Processing*, 114:413–438. vi, 51, 52, 54

[28] Lacayo, R. M., Deaner, B. J., and Allen, M. S. (2017). A numerical study on the limitations of modal Iwan models for impulsive excitations. *Journal of Sound and Vibration*, 390:118–140. 54

[29] Luan, Y., Guan, Z. Q., Cheng, G. D., and Liu, S. (2012). A simplified nonlinear dynamic model for the analysis of pipe structures with bolted flange joints. *Journal of Sound and Vibration*, 331(2):325–344. 55

[30] McCarthy, C. and McCarthy, M. (2005). Three-dimensional finite element analysis of single-bolt, single-lap composite bolted joints: Part II—effects of bolt-hole clearance. *Composite Structures*, 71(2):159–175. 51

[31] McCarthy, C. T., McCarthy, M. A., Stanley, W. F., and Lawlor, V. P. (2005a). Experiences with modeling friction in composite bolted joints. *Journal of Composite Materials*, 39(21):1881–1908. 51

[32] McCarthy, M. A., McCarthy, C. T., Lawlor, V. P., and Stanley, W. F. (2005b). Three-dimensional finite element analysis of single-bolt, single-lap composite bolted joints: Part I - Model development and validation. *Composite Structures*, 71(2):140–158. 51

[33] McCool, J. I. (1986). Comparison of models for the contact of rough surfaces. *Wear*, 107(1):37–60. 59

[34] McCool, J. I. (1987). Relating Profile Instrument Measurements to the Functional Performance of Rough Surfaces. *Journal of Tribology*, 109(2):264. 59

[35] Mindlin, R. D. (1949). Compliance of Elastic Bodies in Contact. *J. Appl. Mech.* 61

[36] Motosh, N. (1976). Determination of Joint Stiffness in Bolted Connections. *Journal of Engineering for Industry*, 98(3):858–861. 66

[37] Nagy, P. B. (1992). Ultrasonic classification of imperfect interfaces. *Journal of Nondestructive Evaluation*, 11(3-4):127–139. 60

[38] Pawlus, P., Zelasko, W., and Michalski, J. (2012). Surface Topography Parameters Important in Contact Mechanics. *Journal of Automation, Mobile Robotics & Intelligent Systems*, 6(4):4–7. 59

[39] Pei, L., Hyun, S., Molinari, J. F., and Robbins, M. O. (2005). Finite element modeling of elasto-plastic contact between rough surfaces. *Journal of the Mechanics and Physics of Solids*, 53(11):2385–2409. 60

[40] Persson, B. N. (2001). Elastoplastic contact between randomly rough surfaces. *Physical Review Letters*, 87(11):116101–1–116101–4. 60

[41] Pesaresi, L., Armand, J., Schwingshackl, C. W., Salles, L., and Wong, C. (2018). An advanced underplatform damper modelling approach based on a microslip contact model. *Journal of Sound and Vibration*, pages 1–14. 52

[42] Petrov, E. P. and Ewins, D. J. (2003). Analytical Formulation of Friction Interface Elements for Analysis of Nonlinear Multi-Harmonic Vibrations of Bladed Disks. *Journal of Turbomachinery*, 125(2):364. 52

[43] Pogačnik, A. and Kalin, M. (2013). How to determine the number of asperity peaks, their radii and their heights for engineering surfaces: A critical appraisal. *Wear*, 300(1-2):143–154. 59

[44] Polycarpou, A. A. and Etsion, I. (1999). Analytical approximations in modeling contacting rough surfaces. *Journal of tribology*, 121(2):234–239. 59

[45] Putignano, C., Afferrante, L., Carbone, G., and Demelio, G. (2012). A new efficient numerical method for contact mechanics of rough surfaces. *International Journal of Solids and Structures*, 49(2):338–343. 60

[46] Raffa, M. L., Lebon, F., and Vairo, G. (2016). Normal and tangential stiffnesses of rough surfaces in contact via an imperfect interface model. *International Journal of Solids and Structures*, 87:245–253. 62

[47] Rotscher, F. (1927). *Die Maschinenelemente*. Springer, Berlin. 66

[48] Sayles, R. S. and Thomas, T. R. (1979). Measurements of the Statistical Microgeometry of Engineering Surfaces. *Journal of Lubrication Technology*, 101(4):409. 59

[49] Schwingshackl, C. W., Di Maio, D., Sever, I., and Green, J. S. (2013). Modeling and Validation of the Nonlinear Dynamic Behavior of Bolted Flange Joints. *Journal of Engineering for Gas Turbines and Power*, 135(12):122504. vi, 52, 53

[50] Segalman, D. J. (2005). A Four-Parameter Iwan Model for Lap-Type Joints. *Journal of Applied Mechanics*, 72(5):752. 53

[51] Segalman, D. J. (2006). Modelling joint friction in structural dynamics. *Structural Control and Health Monitoring*, 13(1):430–453. 53

[52] Segalman, D. J. (2010). A Modal Approach to Modeling Spatially Distributed Vibration Energy Dissipation. (August). 54

[53] Sharma, B. K. G. and Desai, C. S. (1993). Analysis and implementation of thin-layer element for interfaces and joints. 118(27005):2442–2462. 54

[54] Sherif, H. A. and Kossa, S. S. (1991). Relationship between normal and tangential contact stiffness of nominally flat surfaces. *Wear*, 151(1):49–62. 61

[55] Song, Y., Hartwigsen, C. J., McFarland, D. M., Vakakis, A. F., and Bergman, L. A. (2004). Simulation of dynamics of beam structures with bolted joints using adjusted Iwan beam elements. *Journal of Sound and Vibration*, 273(1-2):249–276. 55

[56] Soule de Lafont, M. (2017). *Conception d ' un connecteur élément fini pour la simulation des assemblages boulonnés*. PhD thesis, Universitè Paris-Saclay. 51

[57] Süß, D. and Willner, K. (2015). Investigation of a jointed friction oscillator using the Multiharmonic Balance Method. *Mechanical Systems and Signal Processing*, 52-53(1):73–87. 55

[58] Wileman, J., Choudhury, M., and Green, I. (1991). Computation of Member Stiffness in Bolted Connections. *Journal of Mechanical Design*, 113(4):432. 50, 66

[59] Witteveen, W. and Irschik, H. (2009). Efficient Mode Based Computational Approach for Jointed Structures: Joint Interface Modes. *AIAA Journal*, 47(1):252–263. 54

[60] Yastrebov, V. A., Anciaux, G., and Molinari, J. F. (2015). From infinitesimal to full contact between rough surfaces: Evolution of the contact area. *International Journal of Solids and Structures*, 52:83–102. 60

[61] Yoshioka, N. and Scholz, C. H. (1989). Elastic properties of contacting surfaces under normal and shear loads: 2. Comparison of theory with experiment. *Journal of Geophysical Research*, 94(B12):17691. 61

4

A post-processing toolbox based on Kalman Filter

Contents

Summary Kalman Filter is a powerful tool created in 1960 by Rudolf Kalman. Since then it has been used for a wide range of applications, such as guidance, navigation, control and trajectory optimization of vehicles, in particular aircrafts and spacecrafts, but also robots, followed by applications to time-series analysis, particularly useful in signal processing and econometrics. The purpose of this chapter is to apply the Kalman filter methodology to perform modal analysis on the most common types of tests in the field of structural dynamics, which are impact, sweep sine and random tests. The developed methods are capable of dealing with nonlinearities that are usually found in bolted structures.

4.1 Kalman Filter

The Kalman filter is a recursive optimal state estimator algorithm whose purpose is to follow the evolution in time of a dynamic system. A brief history of the Kalman filter evolution is carried out in order to explain the basic concepts and provide the reader with the necessary knowledge to understand the proposed methods.

4.1.1 Linear Kalman Filter

The original formulation of the Kalman filter [14] is limited to linear systems, but it's important to understand the basic concepts, assumptions and functioning of the filter. Let's assume we have a linear dynamic system that can be described by the following discrete time state-space form:

$$x_k = \mathrm{F}x_{k-1} + \mathrm{B}u_k + w_k \tag{4.1a}$$

$$y_k = \mathrm{H}x_k + v_k \tag{4.1b}$$

where:

- x_k = state vector at step k;
- x_{k-1} = state vector at step $k-1$;
- u_k = input vector at step k;
- y_k = output vector at step k;
- w_k = model noise at step k;
- v_k = measurement or observation noise at step k;
- F = system matrix;
- B = input matrix;
- H = observation matrix;

For the linear case, matrices F, B and H are constant. The most important assumption of the Kalman filter is that the system properties at the step k, which are the state vector x_k, the model noise w_k and the measures noise v_k can be described by normal distributions as:

$$x_k = \mathcal{N}(\hat{x}_k, \mathrm{P}_k) \tag{4.2a}$$

$$w_k = \mathcal{N}(0, \mathrm{Q}_k) \tag{4.2b}$$

$$v_k = \mathcal{N}(0, \mathrm{R}_k) \tag{4.2c}$$

where P_k, Q_k and R_k are the respective covariances at step k, while $\hat{x}_k$ is the estimated state vector. The Kalman filter algorithm is divided in two steps:

- **Prediction**: the state vector and its covariance are predicted from the previous step according to the provided state-space model:

$$\hat{x}_k^- = \mathrm{F}\hat{x}_{k-1} + \mathrm{B}u_k \tag{4.3a}$$

$$\mathrm{P}_k{}^- = \mathrm{F}\mathrm{P}_{k-1}\mathrm{F}^\mathsf{T} + \mathrm{Q}_{k-1} \tag{4.3b}$$

  This step is also referred to as *a priori estimate*.

- **Update**: the *a priori estimates* are compared with observations y_k in order to correct the previous estimation:

$$\hat{x}_k = \hat{x}_k^- + \mathrm{K}_k(y_k - \mathrm{H}\hat{x}_k^-) \tag{4.4a}$$

$$\mathrm{P}_k = (\mathrm{I} - \mathrm{K}_k\mathrm{H})\mathrm{P}_k^- \tag{4.4b}$$

where the K_k is the optimal Kalman gain calculated as:

$$\mathrm{K}_k = \frac{\mathrm{P}_k^-\mathrm{H}^\mathsf{T}}{\mathrm{H}\mathrm{P}_k^-\mathrm{H}^\mathsf{T} + \mathrm{R}} \tag{4.5}$$

This step is also referred to as *a posteriori estimate*.
From Eq. 4.4a and Eq. 4.5 is also possible to define two quantities, which are the observation innovation $\tilde{y}_k$ and the covariance innovation S_k, that are going to be useful when we will talk about Kalman initialization.

$$\tilde{y}_k = y_k - \mathrm{H}\hat{x}_k^- \tag{4.6a}$$

$$\mathrm{S}_k = \mathrm{H}\mathrm{P}_k^-\mathrm{H}^\mathsf{T} + \mathrm{R} \tag{4.6b}$$

The described steps summarize the philosophy behind Kalman filter: it combines two different pieces of information, one from the state model given by the user and one from the measures, in order to find the optimal system state estimation at each step k. Of course this doesn't happen automatically, because convergence is not guaranteed and depends on the initialization provided by the user. The initialization part is probably the reason why Kalman filter hasn't had the success that it deserved, because it needs a lot of experience from the user and sometimes it can be quite a frustrating task. We will talk about Kalman filter initialization and how is it possible to make it partially automated and quicker in section 4.1.3. If the assumptions made for the linear Kalman filter are satisfied, it can be demonstrated that the estimator is optimal. However, the assumptions are rarely met because of the presence of nonlinearities, and divergence occurs. A set of Kalman filter applications capable of handling nonlinearities has been developed and they will be treated in the next section.

In 2008 Kalman receives the National Medal of Science from the USA president Barack Obama

4.1.2 Nonlinear Kalman Filters

Considering that the world where we live is rarely linear, Kalman filter has been adapted over the years in order to be able of handling nonlinear dynamic models. Before diving into the solutions, it's important to understand why the "basic" Kalman filter doesn't work in the presence of nonlinearities in the system. Essentially, if a gaussian distribution undergoes a linear transformation, the output will still be a gaussian distribution. However, if the same gaussian distribution undergoes a nonlinear transformation, the output won't be a gaussian distribution anymore, but it will be deformed. Therefore, different techniques has been developed to overcome this problem and then combined with the original Kalman filter. In the first place we shall define the general nonlinear state-space formulation of a system as:

$$x_k = f(x_{k-1}) + w_k \tag{4.7a}$$

$$y_k = h(x_k) + v_k \tag{4.7b}$$

where $f(x_{k-1})$ is the nonlinear state-transition function and $h(x_k)$ is the nonlinear observation function. In the dedicated literature there is a plethora of different adaptations of the Kalman filter for nonlinear systems but in this work we will focus on the ones that are most used nowadays and which obtained the best results. In particular the Extended Kalman Filter (EKF) and Unscented Kalman Filter (UKF) will be treated in the following sections.

4.1.2.1 Extended Kalman Filter (EKF)

The firsts to understand the capabilities of the Kalman filter were NASA engineers [22] when, in the midst of the *Space Race*, they developed an extended version to use in the Apollo program. The latter eventually brought Neil Armstrong and Buzz Aldrin to land on the moon. Since then it has been recognized as a powerful and practical tool in the aerospace industry [18]. The principle on which the method is found is to consider the system described in eq. 4.7 locally linear. The method requires the state-transition functions $f(x_{k-1})$ and $h(x_k)$ to be differentiables twice. We thereby define the Jacobian matrices F_k and H_k, respectively from $f(x_{k-1})$ and $h(x_k)$, calculated at each step k from the state vector x_k. Furthermore, the assumptions made are the same than for the original Kalman filter. The EKF algorithm can be written as:

Prediction

$$\begin{cases} \hat{x}_k^- = f(\hat{x}_{k-1}) \\ \mathrm{P}_k^- = \mathrm{F}_k \mathrm{P}_{k-1} \mathrm{F}_k^\mathsf{T} + \mathrm{Q}_{k-1} \end{cases} \tag{4.8}$$

Innovation

$$\begin{cases} \tilde{y}_k = y_k - h(\hat{x}_k^-) \\ \mathrm{S}_k = \mathrm{H}_k \mathrm{P}_k^- \mathrm{H}_k^\mathsf{T} + \mathrm{R} \end{cases} \tag{4.9}$$

Kalman gain

$$\mathrm{K}_k = \mathrm{P}_k^- \mathrm{H}_k^\mathsf{T} \mathrm{S}_k^{-1} \tag{4.10}$$

Correction

$$\begin{cases} \hat{x}_k = \hat{x}_{k-1}^- + \mathrm{K}_k y_k \\ \mathrm{P}_k = \mathrm{P}_k^- - \mathrm{K}_k \mathrm{H}_k \mathrm{P}_k^- \end{cases} \tag{4.11}$$

As it can be observed, the EKF uses the same scheme of the Kalman filter, but linearizing around the step k. The problem is that, if the nonlinearity becomes too important, the algorithm won't be able to cope with it. That's why the EKF is suitable only for weakly nonlinear system. Moreover, the algorithm is more expensive from the computational point of view because of the Jacobian calculation, especially if it can't be analytically calculated and it has to be obtained numerically at each time step. Furthermore, even if the Jacobian can be calculated, it can a be a very long and error-prone process, producing pages of algebra that has to be converted into code afterwards.

4.1.2.2 The Unscented Revolution

The EKF limitations made clear that a new and more complex approach was needed to ameliorate the Kalman filter performances for a nonlinear case. The revolution came with the development of the unscented transform (UT) and its application to the Kalman filter [13, 24].

The Unscented Transform (UT) The idea is, literally quoting [12], that *"it is easier to approximate a probability distribution than it is to approximate an arbitrary nonlinear function or transformation"*. It's possible to describe the functioning of the unscented transform in three points:

Uhlmann chose the term *unscented* after noticing a deodorant on a desk.

1. Take a set of $p+1$ points (called *sigma points*) on the starting Gaussian distribution so that the mean and covariance are the same as the distribution. The sigma points are not chosen randomly and there are different ways of choosing them;

2. Choose the way in which the sigma points are weighted. The weights w_i assigned to the sigma points can be positive or negative but, to produce an unbiased estimate, the following condition has to be satisfied:

   $$\sum_{i=0}^{p} w_i = 1 \tag{4.12}$$

   The set of sigma points S can be defined by a $p+1$ array and their associated weights as $\mathrm{S} = \{i = 0, 1, \dots, p : \chi^{(i)}, w_i\}$. A particular set S which satisfies the condition and works well is one in which $2\mathrm{N}_x$ points are chosen symmetrically on the gaussian distribution of depart plus the middle point which represent its mean. The latter allows for a better control of some aspects of the distribution higher moments. Therefore, there will be $2\mathrm{N}_x + 1$ sigma points for each component of the state vector x. This symmetric set can be obtained by:

   Sigma points

   $$\chi^{(0)} = \bar{x} \tag{4.13a}$$

   $$\chi^{(i)} = \bar{x} + \left(\sqrt{\frac{\mathrm{N}_x}{1-w_0}\Sigma_x}\right)_i \tag{4.13b}$$

   $$\chi^{(i+\mathrm{N}_x)} = \bar{x} - \left(\sqrt{\frac{\mathrm{N}_x}{1-w_0}\Sigma_x}\right)_i \tag{4.13c}$$

   Weights

   $$w_0 = w_0 \tag{4.14}$$

   $$w_i = \frac{1-w_0}{2\mathrm{N}_x} \tag{4.15}$$

   $$w_{i+\mathrm{N}_x} = \frac{1-w_0}{2\mathrm{N}_x} \tag{4.16}$$

   The sigma points are collected in the matrix $\chi = [\chi^{(0)}, \chi^{(1)}, \dots, \chi^{(p)}]$, while the weights in the column vector $w = [w_0, w_1, \dots, w_p]^\mathsf{T}$.

3. Apply the nonlinear transformation directly on the weighted *sigma points*. The nonlinear functions is directly applied on the sigma points as:

   $$y_i = f(x_i) \tag{4.17}$$

   Then, the mean $\bar{y}$ and covariance matrix Σ_x of the transformed gaussian distribution are calculated as:

   $$\mathrm{E}_w(\chi) = \sum_{i=0}^{p} w_i \chi^{(i)} \tag{4.18a}$$

   $$= \chi \cdot w \tag{4.18b}$$

$$P_w = \sum_{i=0}^{p} w_i \left\{\chi^{(i)} - E_w(\chi)\right\} \left\{\chi^{(i)} - E_w(\chi)\right\}^{\mathsf{T}} \tag{4.19a}$$

$$= \chi \cdot W \cdot \chi^{\mathsf{T}} \tag{4.19b}$$

with

$$W = [I - w] \times \begin{bmatrix} w_0 & & 0 \\ & \ddots & \\ 0 & & w_p \end{bmatrix} \times [I - w]^{\mathsf{T}} \tag{4.20}$$

It's also important to note that it is possible to calculate the correlated covariance between two distributions $x = \mathcal{N}(\hat{x}, P^x)$ and $y = \mathcal{N}(\hat{y}, P^y)$, represented by the respective sigma points collection χ and ζ, as:

$$P_{xy} = \sum_{i=0}^{2n+1} [\chi_i - \bar{x}] [\zeta_i - \bar{y}]^{\mathsf{T}} \tag{4.21a}$$

$$= \chi \cdot W \cdot \zeta^{\mathsf{T}} \tag{4.21b}$$

To understand how the unscented transform has a great performance advantage compared to the simple linearization, an example of nonlinear transform is considered. The chosen nonlinear function is the transformation of polar coordinates (r, θ) into 2D cartesian coordinates (x, y) :

$$\begin{pmatrix} x \\ y \end{pmatrix} = \begin{pmatrix} r\cos\theta \\ r\sin\theta \end{pmatrix} \tag{4.22}$$

The *Gaussian distribution* is named after Carl Friedrich Gauss, who introduced it in 1809 as the least-square method rationalization.

At this point we consider a target, whose true position in the 2D plane is $(0, 1)$; however, the polar coordinates are affected by an amount of uncertainty, represented by a gaussian distribution. In particular, we consider their mean values to be $\bar{r} = 1$, $\bar{\theta} = 90°$, and their respective standard deviations $\sigma_r = 0.02$m, $\sigma_\theta = 15°$. A set of 1000 pair of polar coordinates with the chosen normal distribution properties were generated. Then, these polar coordinates were transformed into cartesian coordinates by direct application of the nonlinear function of eq.4.22 in order to have the "true" solution. At the same time, the linearized function was applied to the same points, obtaining the linearized solution. In fig. 4.1a it's possible to see in blue the "true" results of the nonlinear function and in green the linearized results. If the linearization can be acceptable for the points close to $x = 0$, it's definitely unacceptable for further points. The blue and green filled dots represent the mean of the true and linearized results, while the ellipses around them represent the 1σ contour of the resulting distribution. It's obvious that, in this case, the linearization approach is not acceptable. Now we apply the unscented transform with the procedure explained previously and by taking $N_x = 2$ and $w_0 = 1/3$. In fig. 4.1b are shown the mean and the 1σ locus of the true results, the linearized transform and the unscented transform respectively in blue, green and orange. Here it's possible to see all the power of the Unscented Transform (UT). The output mean and covariance are very well estimated, while the linearized transformation has already a consistent error on the mean.

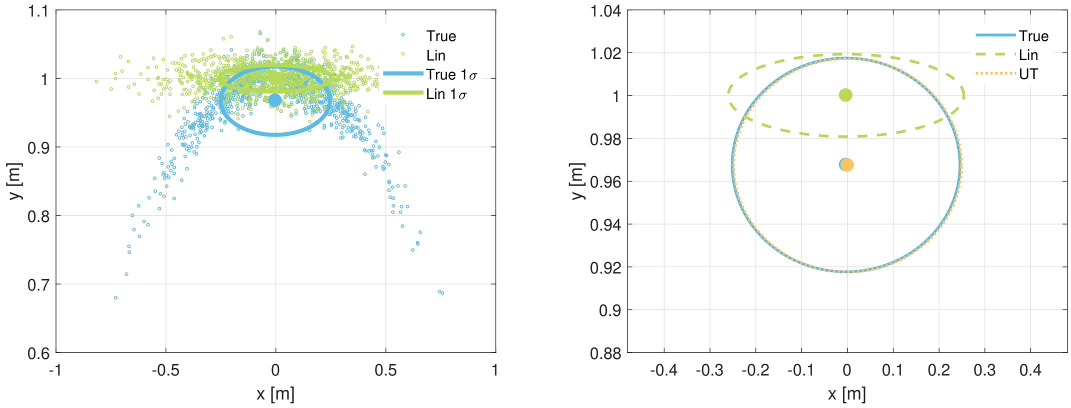

(a) True and linearized polar to cartesian transformation. (b) Comparison between linearized transform and UT

Figure 4.1 – Example

The Unscented Kalman Filter (UKF) At this point it's necessary to find the way of implementing the UT in the Kalman filter algorithm. Following the same standard steps, the latter can be represented as:

Prediction

$$\chi_{k-1} = \mathrm{UT}(\hat{x}_{k-1}, \mathrm{P}_{k-1}) \tag{4.23}$$

$$\begin{cases} \hat{x}_k^- = f(\chi_{k-1}) \cdot w \\ \mathrm{P}_k^- = f(\chi_{k-1}) \cdot \mathrm{W} \cdot f(\chi_{k-1})^{\mathsf{T}} + \mathrm{Q} \end{cases} \tag{4.24}$$

Innovation

$$\chi_k^- = \mathrm{UT}(\hat{x}_k^-, \mathrm{P}_k^-) \tag{4.25}$$

$$\zeta_k^- = h(\chi_k^-) \tag{4.26}$$

$$\hat{y}_k^- = \zeta_k^- \cdot w \tag{4.27}$$

$$\begin{cases} \tilde{y}_k = y_k - \hat{y}_k^- \\ \mathrm{S}_k = \zeta_k^- \cdot \mathrm{W} \cdot (\zeta_k^-)^{\mathsf{T}} + \mathrm{R}; \end{cases} \tag{4.28}$$

Correlation

$$\mathrm{P}_{xz_k}^- = \chi_k^- \cdot \mathrm{W} \cdot (\zeta_k^-)^{\mathsf{T}} \tag{4.29}$$

Kalman gain

$$\mathrm{K}_k = \mathrm{P}_{xz_k}^- \cdot \mathrm{S}_k^{-1} \tag{4.30}$$

Correction

$$\begin{cases} \hat{x}_k = \hat{x}_k^- + \mathrm{K}_k \tilde{y}_k \\ \mathrm{P}_k = \mathrm{P}_k^- - \mathrm{K}_k \mathrm{S}_k^{-1} \mathrm{K}_k^{\mathsf{T}} \end{cases} \tag{4.31}$$

Comparing the UKF algorithm with the EKF one, we can say that the computational cost of the two filters is of the same order, but with the UKF offering a higher degree of precision on the filter performances. Furthermore, the two algorithms have the same order of magnitude of computational cost but, while the UKF can be applied as a "black box" filtering to any probability distribution, the EKF requires the calculation of the Jacobian matrices, which depend on the model. Inside the unscented transform, the most expensive operation is the calculation of the covariance matrix square root for the sigma-points definition (eqs. 4.13a-4.13c), which requires a numerically efficient and stable method such as the Cholesky decomposition. Moreover, an important element to take into account is the fact that for each elements in the state vector x, the UT is applied to $2\mathrm{N}_x + 1$ sigma points, in respect of which the computational cost is proportional.

UT improvements The unscented transform has been object of many attempts to improve its performances. The majority of them are related to the way of choosing the sigma-points and their weights. In fact, it's on these factors that depends the ability of the UT to capture second order or higher statistical moments. For example, [25] has proposed to use different weights for the empirical mean and covariance, that can be modified through the choice of different parameters. The weights are calculated as follows:

where:

Mean weights

$$w_0^m = \frac{\lambda}{\mathrm{N}_x + \lambda} \tag{4.32}$$

$$w_i^m = \frac{1}{2(\mathrm{N}_x + \lambda)} \tag{4.33}$$

Covariance weights

$$w_0^c = \frac{\lambda}{\mathrm{N}_x + \lambda} + (1 - \alpha^2 + \beta) \tag{4.34}$$

$$w_i^c = \frac{1}{2(\mathrm{N}_x + \lambda)} \tag{4.35}$$

$$\lambda = \alpha^2(\mathrm{N}_x + \kappa) - \mathrm{N}_x \tag{4.36}$$

Depending on the choice of α and κ, the sigma points are shifted further or closer to the gaussian average, while β is introduced trying to capture the higher order statistical moments. Based on this method, other authors have developed different ways of selecting the parameters, such as Masoumnezhad et al. [17], where a genetic algorithm is employed. In order to speed up the algorithm, Julier [11] proposed the simplex sigma points set, where only $\mathrm{N}_x + 1$ sigma points are chosen, after having demonstrated that it's the minimum number of points necessary to describe a gaussian distribution. In addition, a family of methods called NSUT are developed [15], which consider an asymmetric set of sigma points in order to capture higher order statistical moments with more precision.

The first to use the statistical term *variance* was Ronald Fisher, in a seminal paper from 1918.

4.1.2.3 Particle Filter (PF)

The methods discussed until now are all related by the fact that they assume the probability distribution to be gaussian, which of course is not always true. The particle filter [1], instead, can treat any kind of probability distribution and it also handles nonlinear functions. The way in which it works it's very similar to the unscented transform, but in this case the sigma points are called *particles* and their number has to be much higher. The latter aspect obviously slows down the algorithm, thus narrowing its usage to cases where the probability distribution can't be approximated by a gaussian one. A thorough review on particle filters is offered in Jouin et al. [10].

4.1.2.4 Methods comparison

With the intent of summarizing the methods covered in the previous sections, Table 4.1 compares the main features of the different filtering techniques. The goal of this thesis chapter is to develop a set of tools for the analysis of different kind of testing data on structures assembled mainly with bolted joints. These kind of structures are usually weakly nonlinear but for high excitation level and low values of tightening torque, the degree of nonlinearity can become relevant. Therefore, the method chosen for this work is the Unscented Kalman Filtering with a symmetric set of $2N_x + 1$ sigma points and the system of weights described in Eqs. 4.32-4.36.

4.1.3 Initialization of the Kalman Filter

The Kalman filter is without any doubt a very powerful tool for prediction, tracking and many other applications, but there is quite a big **BUT**: the initialization of the filter and their covariances. From the algorithms described in the previous sections, its easy to see that there are four quantities to provide to the filter, listed here in ascending order of the difficulties that they pose:

- $\hat{x}_0, P_0$: initial state and its covariance;
- R: measurements covariance;
- Q: model covariance.

Their good estimation is necessary for the algorithm convergence and proper functioning. The main problem is that their tuning can take a very long time and can be quite frustrating, based on the user experience (and sometimes luck) with Kalman filter. In order to partially automate the task, we will take them one by one and we will try to find a correct initialization technique.

4.1.3.1 Initial state and its covariance P_0

These two quantities are treated together because they both concern the initial state of the system and also because they can be linked between each other. The initial state x_0 is simply the state of the system at the first time step, while the user estimate is $\hat{x}_0$. Basically, the initial covariance P_0 represents the confidence in the user estimate $\hat{x}_0$ of the initial state. In order for the Kalman filter to work properly, the initial state vector estimate $\hat{x}_0$ has to be close enough to the actual value x_0. A more difficult task is to choose the initial state covariance P_0, for which we can use fig. 4.2a to help us out. Assuming an acceptable initial state vector estimate $\hat{x}_0$, in the fig. 4.2a are shown three cases of P_0 initialization, where $\sigma_P = \sqrt{P_0}$ is the standard deviation chosen for the initial state estimate $\hat{x}_0$. The colored areas represent the incertitude envelop for three different cases of initialization: the range area shows a very large incertitude envelope, the light blue area shows a correct initialization, while the yellow area shows a very small incer-

ESTIMATOR	MODEL	ASSUMPTION	CPU COST
Kalman Filter (KF)	Linear	Gaussian	Low
Extended Kalman Filter (EKF)	Locally Linear	Gaussian	Low (Analytical J) Medium (Numerical J)
Unscented Kalman Filter (UKF)	Nonlinear	Gaussian	Medium
Particle Filter (PF)	Nonlinear	none	High

Table 4.1 – Comparison of main Kalman filtering methods features

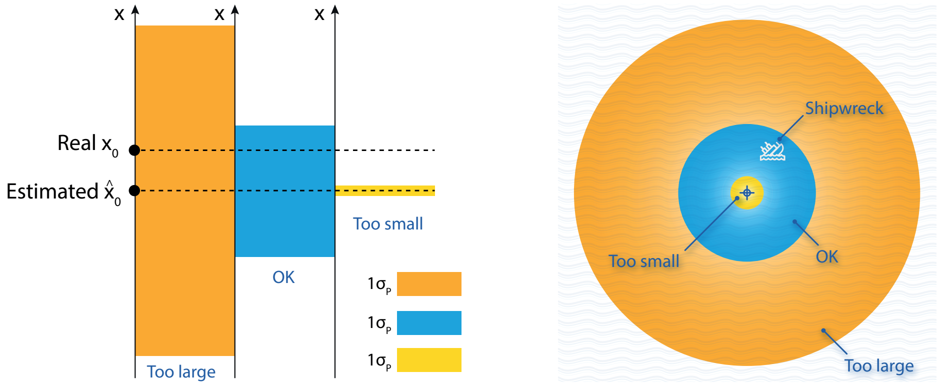

(a) Examples of good and bad initializations of initial state covariance P_0

(b) The shipwreck search comparison

Figure 4.2 – Initial state parameters initialization

titude envelope, which doesn't include the real initial state x_0. To be crystal clear on the subject we can compare the initialization task to a shipwreck hunt, as illustrated in fig. 4.2b. When searching for a shipwreck in the ocean, an estimation of the sinking spot (our $\hat{x}_0$) and a circular research area around it (our P_0) is provided. The higher the error on the initial estimation of the sinking spot, the lower the probability of finding the shipwreck. Assuming a decent estimation of the sinking spot, let's now focus on the research area. On one hand, if the latter is set too large, the search could take a long time and there is the possibility that the shipwreck will never be found. . On the other hand, if the research area is set too small (as in the third case of fig. 4.2a), the shipwreck could be lying outside it and, again, never be found.

The Titanic sank in 1912, but its wreck was located only in 1985.

With the purpose of avoiding a frustrating shipwreck hunt, an initialization procedure to correctly and consistently choose the initial state has been developed. The *optimal* initial covariance P_0 can be calculated as:

$$P_0 = (\hat{x}_0 - x_0)^\top (\hat{x}_0 - x_0) \tag{4.37}$$

If some of the variables are directly observed, then the values are known, but if that is not the case, they need to be estimated. It's usually difficult to estimate them with precision, but it's possible to provide an upper bound value x_u and a lower bound value x_l, with which is then possible to obtain the initial state estimation $\hat{x}_0$ as the bounds' average:

$$\hat{x}_0 = \frac{x_u + x_l}{2} \tag{4.38}$$

Then, it can be conservatively assumed that the difference between the initial state estimate and the true one can be obtained as:

$$\hat{x}_0 - x_0 = k_p \frac{x_u - x_l}{2} \tag{4.39}$$

where k_p is a coefficient that can increase or decrease the confidence in the estimate (by default $k_p = 1$). P_0 can then be calculated using eq. 4.37.

Experience shows that in most cases the filter won't be fatally affected by $\hat{x}_0$ — unless the chosen upper and lower bounds are very wrong — while it will diverge if P_0 is not properly chosen. In conclusion, the user will only be requested to input the lower and upper bounds of the initial state vector, and the values of $\hat{x}_0$ and P_0 will be automatically calculated.

4.1.3.2 Measurements Covariance R

The parameter R represents the measurements covariance, which, practically speaking, is the confidence that we have in the experimental data. The dimension of R is equal to the number of observed experimental measures that we compare with Kalman predictions in the *innovation* phase.

The main question here is: can R be treated as an additive noise or does it change in time and has to be estimated at each time step? It usually depends on the data, but for the applications treated in this work it can be considered time-invariant. In fact, vibration test data usually consist of accelerations — gathered by accelerometers positioned on the testing structure — and they consist of two parts: the part that we actually want to track, and the part that pollute the main signal, which is usually referred as sensor noise. Considering this case, the measurement covariance can be estimated as:

$$\mathrm{R} = k_r \sigma_r^2 \tag{4.40}$$

where k_r is a coefficient that can increase or decrease the confidence in the estimate (by default $k_r = 1$), while σ_r is the sensor noise standard deviation. The latter it's very difficult to estimate from measurements, but the problem can be bypassed by registering an accelerometer time series without any external input. In this way σ_r can be estimated by directly calculating the standard deviation on the registered time series. This method has proven to be working well in the cases treated in the next sections.

4.1.3.3 Model Covariance Q

Concerning the model covariance Q, it represents the confidence we have in the model — described by $f(x_{k+1})$ — with which we want to track the signal. If we think the numerical model is accurate enough to reproduce the real behavior, then we will trust the model by setting a low covariance value. Otherwise a larger value will be adopted. Of course, each state vector variable will have its own covariance value.

The model covariance Q is probably the most difficult parameter to choose. The reason is that, as for R, it can't be usually considered as an additive noise and it depends on the state of the system. In Schneider and Georgakis [21], the authors propose a method to calculate the model noise covariance Q thanks to the principle of the maximum likelihood and it can be calculated at each time step, but it's valid only for the EKF. In [27], instead, the authors propose an augmented version of the UKF, in which the model noise covariance Q can be tracked as an additional state space variable. However, to the best of the author's knowledge, a reliable and accurate method for the calculation of this crucial parameter has not been found yet.

"Statistics is the grammar of science."
K. Pearson

All along this chapter, the model noise covariance Q will be treated as a gaussian additive noise and manually tuned. This can be a delicate and time consuming task. However, considering that it's the only set of parameters whose choice is not automated, with some expertise they can be easily tuned.

4.1.4 Tracking of a generic sine signal with a Kalman filter

Before jumping into the model formulations for different types of vibration testing signals, a small introduction on the tracking of a general sine signal with Kalman filter is needed. In [2], the authors found a method to track and remove modulated sinusoidal components using the EKF. The method's principle is to reconstruct the sine signal as an analytic signal, which is a complex signal whose imaginary part is the Hilbert transform of the real part, written as follows:

$$x(t) = x_1(t) + j x_2(t) \tag{4.41}$$

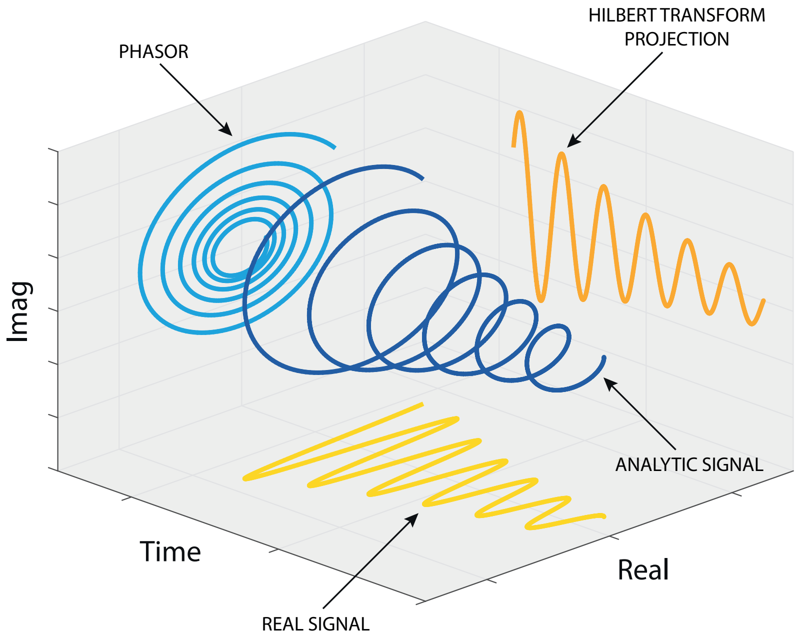

Figure 4.3 – Illustration of the analytic signal (inspired by Feldman [5]).

where $x_2(t)$ is the Hilbert transform of $x_1(t)$. The choice of real and imaginary parts notation is going to be functional for the next steps. The analytic signal can be clearly visualized in the 3D plot of fig. 4.3. The analytic signal can also be represented in the trigonometric or exponential form as:

$$x(t) = \mathrm{A}(t)e^{j\phi(t)} \tag{4.42}$$

where the instantaneous amplitude $\mathrm{A}(t)$ and the instantaneous phase ϕ can be obtained as:

$$\mathrm{A}(t) = \sqrt{x_1^2(t) + x_2^2(t)} \tag{4.43a}$$

$$\phi(t) = \arctan\frac{x_2(t)}{x_1(t)} \tag{4.43b}$$

In order to use the Kalman filter, a discrete state space form of the signal is necessary. Eq. 4.42 represents a generic amplitude and frequency modulated sine signal. At a generic time step $t_k = k\Delta t$ the signal becomes:

$$x_k = \mathrm{A}_k e^{j(\omega_k k\Delta t)} \tag{4.44}$$

where $\omega_k = 2\pi f_k$ is the instantaneous angular frequency. At this point, assuming that the parameters A_k and ω_k only slowly vary over time, they can be considered equal between two time steps. The signal at t_{k+1} can be approximated as:

$$x_{k+1} \approx \mathrm{A}_k e^{j(\omega_k(k+1)\Delta t)} = \mathrm{A}_k e^{j(\omega_k k\Delta t)} e^{j(\omega_k \Delta t)} \tag{4.45}$$

Then, it's possible to obtain the real and imaginary parts of x_{k+1} as a function of the real and imaginary parts of x_k as:

$$x_{1,k+1} = x_{1,k}\cos(\omega_k\Delta t) - x_{2,k}\sin(\omega_k\Delta t) \tag{4.46a}$$

$$x_{2,k+1} = x_{1,k}\sin(\omega_k\Delta t) + x_{2,k}\cos(\omega_k\Delta t) \tag{4.46b}$$

We can define the state space variable array $\mathrm{X}_k = (x_{1,k}, x_{2,k}, \omega_k)^\mathsf{T}$. It's possible to see that, instead of ω_k, we could have created a new variable $x_{3,k} = \omega_k\Delta t$, but the reason why we didn't do that it's because we want the chosen variables to be independent from the time step Δt. This allows, for example, to perform a downsampling process without having to change the initialization parameters.

At this point we can write the nonlinear state space formulation as:

$$\mathrm{X}_{k+1} = f(\mathrm{X}_k) + \mathrm{Q}_k \tag{4.47}$$

$$\mathrm{Y}_{k+1} = h(\mathrm{X}_k) + \mathrm{R}_k \tag{4.48}$$

where Q_k and R_k are respectively the model noise and the measurements noise, assumed to be described by a gaussian distribution. Concerning the nonlinear transition part $f(\mathrm{X}_k)$, it can be written as:

$$f(\mathrm{X}_k) = \mathrm{F}_k\mathrm{X}_k = \begin{bmatrix} \cos(\omega_k\Delta t) & -\sin(\omega_k\Delta t) & 0 \\ \sin(\omega_k\Delta t) & \cos(\omega_k\Delta t) & 0 \\ 0 & 0 & 1 \end{bmatrix} \begin{pmatrix} x_{1,k} \\ x_{2,k} \\ \omega_k \end{pmatrix} \tag{4.49}$$

The observation function $h(\mathrm{X}_k)$ is actually linear and the only state variable observed is the signal real part. Therefore the observation can be obtained as:

$$h(\mathrm{X}_k) = \mathrm{H}\mathrm{X}_k = \begin{bmatrix} 1 & 0 & 0 \\ 0 & 0 & 0 \\ 0 & 0 & 0 \end{bmatrix} \begin{pmatrix} x_{1,k} \\ x_{2,k} \\ \omega_k \end{pmatrix} \tag{4.50}$$

Eqs. 4.47-4.50 describe the basic state space model that can be used by a Kalman filter to track a sine signal **slowly** modulated in frequency. We will see that this condition is met for the impact and sweep applications, while for the random tests a new formulation will have to be developed.

In the next section the basic formulation will be further modified and adjusted for the impact test signal type.

4.2 Kalman Filter for impact tests

Let's suppose that a component or a structure is built and a basic dynamic characterization is needed: the fastest and most common type of test that it's possible to do is an impact test. The latter consists of hitting the test structure with a sensor-equipped (or not) hammer and registering the system time response. The most common procedure used the Fourier transforms of the time histories of hammer input force and system response to calculate the Frequency Response Function (FRF), followed by a frequency domain modal identification procedure on the calculated FRF to obtain the natural frequencies and damping values.

An alternative to this technique is a time domain method which uses the Hilbert Transform [5]. The original method is called FREEVIB [3]: it calculates natural frequencies and damping by following the system response envelope. The advantage of this method is that it's suitable for nonlinear system. However, the main disadvantage is that the signal on which the method is applied has to be a single-frequency signal. The latter means that the time response signal has to be filtered around each mode, a task that is not always easy or doable. A solution to this problem was proposed by Huang et al. [7] with their empirical mode decomposition, but the implementation of the method on real data is not straightforward.

The approach proposed in this section is a time domain method which uses the Unscented Kalman Filter described in section 4.1.2.2 to track the instantaneous natural frequencies and damping values of a structure excited by a shock.

4.2.1 Model Formulation

In section 4.1.4, we developed the basic state space model formulation. The latter is going to be adapted to impact vibration testing.

First of all we need to provide the general form of impact data. The main feature of a system response to an impact is the decrease of amplitude in time. In the case of purely linear systems, the envelope of the signal decreases in a perfect exponential way, since the system damping is the same at every oscillation amplitude. Considering that the impact excites a certain number of modes M and assuming the superposition principle to be valid, the total system response can be written as the sum of all modes contributions as it follows:

$$\sum_{m=1}^{\mathrm{M}} \mathrm{A}_m(t) e^{j\omega_m(t)t} e^{-\zeta_m(t)\omega_m(t)t} \tag{4.51}$$

Each mode is characterized by an amplitude $\mathrm{A}_m(t)$, a natural frequency $f_m(t) = 2\pi\omega_m(t)$, and a damping ratio $\zeta_m(t)$ that vary in time when the system is nonlinear and their behavior is directly related to the oscillation amplitude. Now we need to derive the discrete state-space system as it has been done in section 4.1.4. For the sake of clarity we consider a single mode, whose position at a certain time step $t_k = k\Delta t$ can be written as:

$$x_k = \mathrm{A}_k e^{j\omega_k k\Delta t} e^{-\zeta_k \omega_k k\Delta t} \tag{4.52}$$

while the position at the next time step $t_{k+1} = (k+1)\Delta t$ is:

$$x_{k+1} = \mathrm{A}_{k+1} e^{j\omega_{k+1}(k+1)\Delta t} e^{-\zeta_{k+1}\omega_{k+1}(k+1)\Delta t} \tag{4.53}$$

At this point, in order to be able to write the position x_{k+1} as a function of x_k we need to make the following assumptions:

- $\mathrm{A}_{k+1} \approx \mathrm{A}_k \rightarrow$ Slow varying signal amplitude;
- $\omega_{k+1} \approx \omega_k \rightarrow$ Slow varying nonlinear frequency;
- $\zeta_{k+1} \approx \zeta_k \rightarrow$ Slow varying nonlinear damping ratio.

The position x_{k+1} can now be approximated as:

$$x_{k+1} \approx \mathrm{A}_k e^{j\omega_k(k+1)\Delta t} e^{-\zeta_k\omega_k(k+1)\Delta t} \tag{4.54}$$

After some math it's possible to find the relations like in eq. 4.46 between the real and imaginary part of x_{k+1} and x_k:

$$x_{1,k+1} = x_{1,k}\cos(\omega_k\Delta t)e^{-\zeta_k\omega_k\Delta t} - x_{2,k}\sin(\omega_k\Delta t)e^{-\zeta_k\omega_k\Delta t} \tag{4.55a}$$

$$x_{2,k+1} = x_{1,k}\sin(\omega_k\Delta t)e^{-\zeta_k\omega_k\Delta t} + x_{2,k}\cos(\omega_k\Delta t)e^{-\zeta_k\omega_k\Delta t} \tag{4.55b}$$

It's interesting to note that the only difference is the presence of the exponential decreasing term.

We define the state space variable vector $\mathrm{X}_k = (x_{1,k}, x_{2,k}, \omega_k, \zeta_k)$, the state-space transition part can be written as:

$$f(\mathrm{X}_k) = \mathrm{F}_k\mathrm{X}_k = \begin{bmatrix} \cos(\omega_k\Delta t)e^{-\zeta_k\omega_k\Delta t} & -\sin(\omega_k\Delta t)e^{-\zeta_k\omega_k\Delta t} & 0 & 0 \\ \sin(\omega_k\Delta t)e^{-\zeta_k\omega_k\Delta t} & \cos(\omega_k\Delta t)e^{-\zeta_k\omega_k\Delta t} & 0 & 0 \\ 0 & 0 & 1 & 0 \\ 0 & 0 & 0 & 1 \end{bmatrix} \begin{pmatrix} x_{1,k} \\ x_{2,k} \\ \omega_k \\ \zeta_k \end{pmatrix} \tag{4.56}$$

Now we need to adapt this system to a set of data which includes a certain number of sensors or measurement points N and M modes. First, for a mode m, we can write the generic block:

$$\mathrm{F}_{m,k} = \begin{bmatrix} \cos(\omega_{m,k}\Delta t)e^{-\zeta_{m,k}\omega_{m,k}\Delta t} & -\sin(\omega_{m,k}\Delta t)e^{-\zeta_{m,k}\omega_{m,k}\Delta t} \\ \sin(\omega_{m,k}\Delta t)e^{-\zeta_{m,k}\omega_{m,k}\Delta t} & \cos(\omega_{m,k}\Delta t)e^{-\zeta_{m,k}\omega_{m,k}\Delta t} \end{bmatrix} \tag{4.57}$$

Secondly, considering the measure point n, we can define:

$$x_{nm,k} = (x_{1,k}^{nm},\, x_{2,k}^{nm})^{\mathsf{T}} \tag{4.58}$$

In this way it's possible to write the full state space transition part as:

$$f(\mathrm{X}_k) = \mathrm{F}_k\mathrm{X}_k = \begin{bmatrix} \mathrm{F}_{1,k} & & & & & & & & & & \\ & \ddots & & & & & & & & & \\ & & \mathrm{F}_{1,k} & & & & & & & & \\ & & & 1 & & & & & & & \\ & & & & 1 & & & & & & \\ & & & & & \ddots & & & & & \\ & & & & & & \mathrm{F}_{m,k} & & & & \\ & & & & & & & \ddots & & & \\ & & & & & & & & \mathrm{F}_{m,k} & & \\ & & & & & & & & & 1 & \\ & & & & & & & & & & 1 \end{bmatrix} \begin{pmatrix} x_{11,k} \\ \vdots \\ x_{n1,k} \\ \omega_{1,k} \\ \zeta_{1,k} \\ \vdots \\ x_{1m,k} \\ \vdots \\ x_{nm,k} \\ \omega_{m,k} \\ \zeta_{m,k} \end{pmatrix} \tag{4.59}$$

For each mode there are N basic blocks representing each measure points. The more the measure points, the better the Kalman filter works, since it has more measures to compare between each other to determine natural frequencies and damping ratios. As it's possible to note, the natural frequency ω_m and the damping ratio ζ_m are tracked at each time step. It's also possible to say that the length L of the state variable vector X_k can be calculated as $\mathrm{L} = (2\mathrm{N}+2)\mathrm{M}$, where N is the number of time measurements and M is the number of modes that we want to follow.

The only aspect left to declare is the observation function $h(\mathrm{X}_k)$ (see eq. 4.47). As we have seen in section 4.1.4, the only observed dimension is the measured signal real part, which has to be compared to the predicted real part by the UKF. The contributions of each mode has to be added up for every measure point. Therefore, the observation function is obtained as:

$$h(\mathrm{X}_k) = \begin{pmatrix} \sum_{m=1}^{\mathrm{M}} x_{1,k}^{1m} \\ \sum_{m=1}^{\mathrm{M}} x_{1,k}^{2m} \\ \vdots \\ \sum_{m=1}^{\mathrm{M}} x_{1,k}^{\mathrm{N}m} \end{pmatrix} \tag{4.60}$$

It can be seen that, differently from the transition part, the observation function is linear.
Eq. 4.60 describes the observation function in the case where the measured signals are displacements. However, the most common data from a vibrating structure are measured by accelerometers, therefore giving accelerations as outputs. In this case the observation function has to be modified in order to obtain an acceleration to compare with the data. The displacement x_k is derived twice:

$$x_k = \mathrm{A}_k e^{j\omega_k t_k} e^{-\zeta_k \omega_k t_k} \tag{4.61}$$

$$\dot{x}_k = \omega_k \mathrm{A}_k e^{j\omega_k t_k} e^{-\zeta_k \omega_k t_k} (j - \zeta_k) \tag{4.62}$$

$$\ddot{x}_k = \omega_k^2 \mathrm{A}_k e^{j\omega_k t_k} e^{-\zeta_k \omega_k t_k} (\zeta_k^2 - 2j\zeta_k - 1) \tag{4.63}$$

The real and imaginary parts of the accelerations are then obtained as:

$$\ddot{x}_{1,k} = \omega_k^2 \left[x_{1,k}(\zeta_k^2 - 1) + 2\zeta_k x_{2,k} \right] \tag{4.64}$$

$$\ddot{x}_{2,k} = \omega_k^2 \left[x_{2,k}(\zeta_k^2 - 1) - 2\zeta_k x_{1,k} \right] \tag{4.65}$$

Finally, the observation function in case of acceleration data becomes:

$$h(\mathrm{X}_k) = \begin{pmatrix} \sum_{m=1}^{\mathrm{M}} \omega_{m,k}^2 \left[x_{1,k}^{1m}(\zeta_{m,k}^2 - 1) + 2\zeta_{m,k} x_{2,k}^{1m} \right] \\ \sum_{m=1}^{\mathrm{M}} \omega_{m,k}^2 \left[x_{1,k}^{2m}(\zeta_{m,k}^2 - 1) + 2\zeta_{m,k} x_{2,k}^{2m} \right] \\ \vdots \\ \sum_{m=1}^{\mathrm{M}} \omega_{m,k}^2 \left[x_{1,k}^{\mathrm{N}m}(\zeta_{m,k}^2 - 1) + 2\zeta_{m,k} x_{2,k}^{\mathrm{N}m} \right] \end{pmatrix} \tag{4.66}$$

4.2.2 Test Case

In order to provide an example of the identification method described for impact tests, a simple nonlinear system is studied. The latter is shown in fig. 4.4, and is represented by a Single-Degree-Of-Freedom (SDOF) system consisting of a mass, a viscous damper, a spring, and a 4-parameter Iwan model in parallel. The system dynamic equation can be written as:

$$m\ddot{x} + c\dot{x} + kx + f_{iwan}(x, \dot{x}, \mathrm{PAR}) = \mathrm{F}(t) \tag{4.67}$$

where m is the mass, c is the viscous damping coefficient, k is the spring stiffness, $\mathrm{F}(t)$ is the excitation force applied on the system, and f_{iwan} is the force developed by the Iwan element. The latter is a function of the mass displacement x, the mass velocity $\dot{x}$, and of the set of parameter $\mathrm{PAR} = \{\mathrm{K}_t, \mathrm{F}_s, \chi, \beta\}$. An impact on the system is numerically simulated and the time response is shown in blue in the left plot of fig. 4.5. On this signal is applied the nonlinear identification process previously described, which utilizes the UKF. The reconstructed time signal and the calculated amplitude are shown in the same graph respectively in green and orange. On the right of fig. 4.5 are presented the natural frequency and the damping ratio as a function of time. It's possible to observe that at the beginning, when the amplitude of the signal is higher, the natural frequency is lower and the damping ratio is higher. However, in order to obtain the so-called *backbone*, the evolution of the natural frequency is plotted against the corresponding instantaneous signal amplitude. This process is carried out for the nonlinear frequency and damping and the result can be observed in fig. 4.6. At the same time, the theoretical nonlinear behavior due to the implemented Iwan Element is plotted. It's possible to see that post-processing technique using Kalman follows the theoretical curves. The straight line at an amplitude of $x \approx 0.11$ represents the discontinuity at the transition between micro-slip and macro-slip for the analytic expression of the Iwan model.

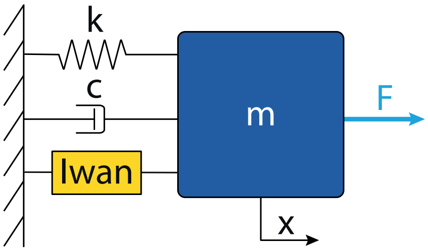

Figure 4.4 – SDOF nonlinear test case. $m = 1\mathrm{Kg}$, $c = 1\mathrm{Nms}^{-1}$, $k = 3947.8\mathrm{Nm}^{-1}$. Iwan: $\mathrm{F}_s = 10\mathrm{N}$, $\mathrm{K}_t = 1500\mathrm{Nm}^{-1}$, $\chi = -0.3$, $\beta = 0.5$.

As a conclusion to the analysis of the test case, an investigation on the values of model and measurement covariances Q and R is carried out. The goal is to qualitatively show the relationship that exists between these two parameters an the importance of their correct choice. For this study a larger gaussian noise was added to the measures, in order to show in a better way the influence of the measurement covariance R.

At first, the initial state vector estimate $\hat{x}_0$ and its covariance P_0 were determined with the method shown in section 4.1.3.1. Then, the measurement covariance R was calculated with the method given in section 4.1.3.2. Finally, the components of the model covariance vector Q were tuned to find an acceptable solution.

At this point, the values of Q and R have been varied to show how the UKF reacts in terms of provided results of its nonlinear identification task. The results of this process can be observed in fig. 4.7, where the nonlinear frequency backbone identification is shown for nine different combinations of Q and R. The dark blue dotted lines represent the Iwan model implemented in the test case, the light blue lines represent the raw results from Kalman identification procedure and the yellow dotted lines are the splines that fit the raw results. The center plot shows the results obtained with the base set of parameters. The values of the model covariance Q become larger from left to right, while the values of measurement covariance R become larger from bottom to top. In section 4.1.3.3 it was explained that the covariance vector Q represents the confidence that we have in the model: the **lower** its value, the **higher** the trust we place in implemented model.

The results show three interesting behaviors:

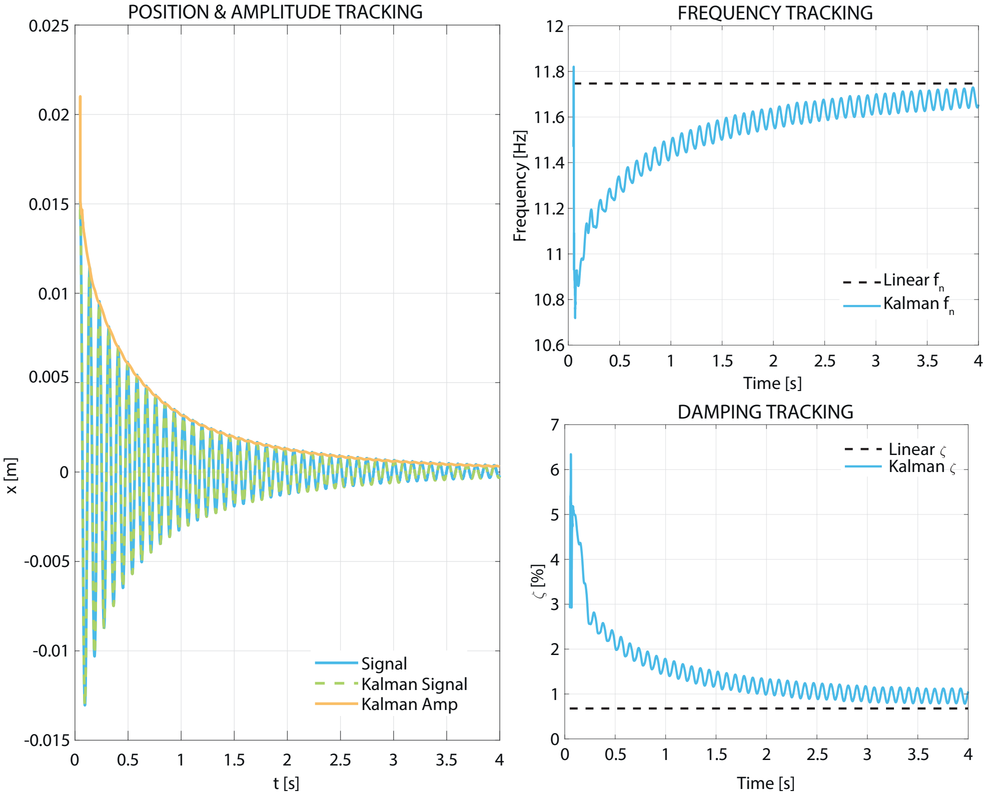

Figure 4.5 – Example of Kalman filter application for impact tests.

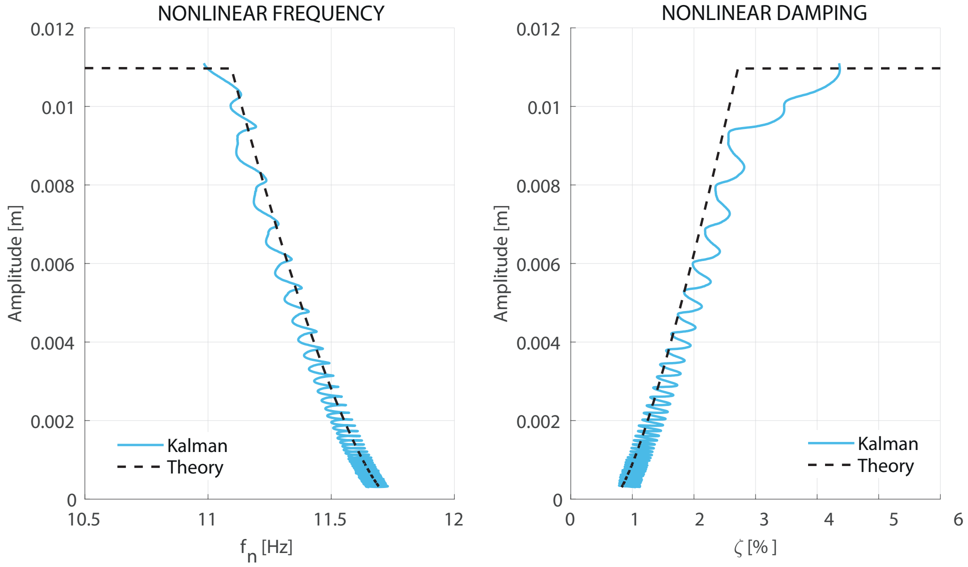

Figure 4.6 – Comparison between Kalman nonlinear identification and theory

1. **Unaltered diagonal:** the results obtained on the diagonal are very similar to each other in terms of raw results and practically equivalent regarding the spline fits. This shows that an important aspect between model and measurements covariances is their ratio.

2. **Incorrect upper diagonal:** when Q gets relatively small compared to R, meaning that we trust more the model implemented in the Kalman filter, the latter provides cleaner but incorrect results. In fact, as it can be well observed in the top left corner plot, the Kalman filter underestimates the nonlinearity by providing an almost vertical identified backbone. This happens because the Kalman filter *follows* too much the model, which in itself is linear.

3. **Noisy lower diagonal:** when R gets relatively small, meaning that we underestimate the amount of signal that we are not interested in tracking, the oscillation around the correct solution is larger. The phenomenon can be well observed in the bottom right corner plot. However, the spline fit gives pretty much the same results as for the reference center plot.

An important takeaway of this study is the fact that is usually better to have noisier results rather than a cleaner trend, which could simply means that the Kalman filter is *following* too much the model, even if it's not correct. This behavior have been observed not only for the impact test post-processing method, but also for other methods and applications.
In the next section a post-processing method for sweep sine tests will be developed and applied to this same test case.

4.3 Kalman Filter for sweep sine tests with harmonics tracking

If impact testing is the most common type of test to quickly characterize a structure in general, sweep sine testing is the most common choice when a further degree of precision in modal identification is needed. In fact, if correctly implemented, it's a very good alternative to the reliable but time consuming phase resonance test.

4.3.1 Sweep sine testing

Sweep tests are carried out exciting a structure with a sine signal in a certain frequency range, between a start frequency f_0 and an end frequency f_1, in a certain amount of time t_s. The sweep rate v_s is the speed with which the frequency range is covered, and it can be linear — expressed in Hz/min — or logarithmic — expressed in oct/min. The latter is useful when the lower frequencies in the chosen frequency range, where modes are usually less damped, have to be covered in a slower way than the higher frequencies. Sometimes the sweep rate can also be manually controlled. Sweep test can be controlled following one of these two rules:

- Input force control: the input force amplitude is kept constant throughout the whole frequency range;

- Output displacement control: the input force is regulated in order to keep the system response constant throughout the whole frequency range.

The frequency range is chosen to include one or more natural frequencies, in order to perform on them a modal identification. There are guidelines in order to perform a correct sweep test and they are found in the ISO 7626 norm: for example, there is a recommended maximum sweep rate that depends on the frequency range and the structure. For linear sweep test the

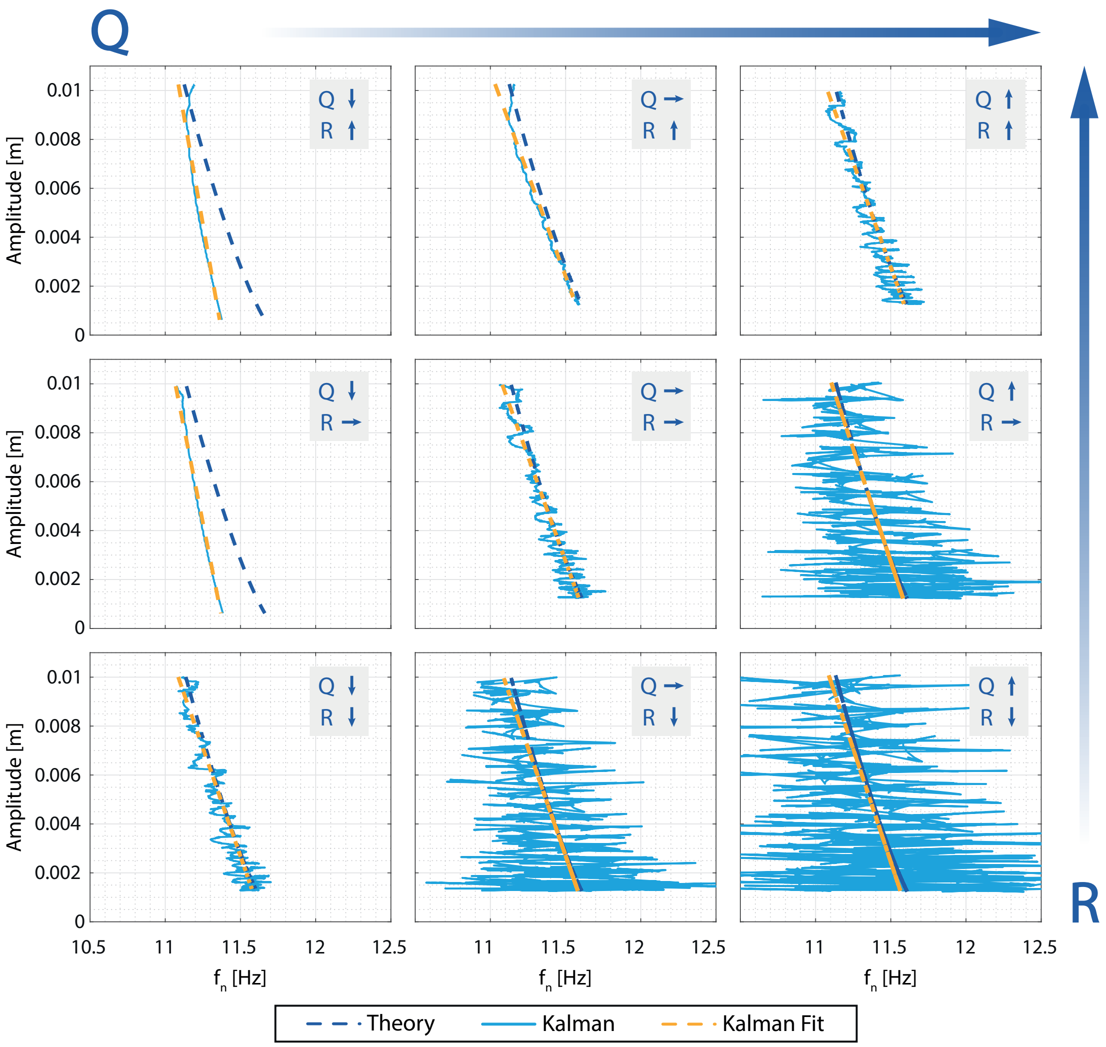

Figure 4.7 – Natural frequency identification on the test case as function of Q and R covariances.

maximum recommended sweep rate is:

$$v_{s,max} = \frac{54 f_r^2}{\mathrm{Q}^2} \quad [\mathrm{Hz/min}] \tag{4.68}$$

while for logarithmic sweep:

$$\mathrm{V}_{s,max} = \frac{77.6 f_r^2}{\mathrm{Q}^2} \quad [\mathrm{oct/min}] \tag{4.69}$$

where f_r is the natural frequency of each mode crossed by the sweep and Q is the mode dynamic amplification that can be calculated as $\mathrm{Q} = 1/2\zeta_r$, where ζ_r is the mode damping ratio. In order to estimate the mode natural frequency and its damping ratio for the maximum sweep rate calculation, a modal identification is usually carried out on impact test data. It can be noted that the maximum sweep rate can be very low for weakly damped low frequency modes, which can notably extend the sweep duration. This problem is particularly known in the Ground Vibration Testing (GVT) environment, where very large structures (planes, helicopters, etc) with very weakly damped natural frequencies lower than 1Hz are tested.

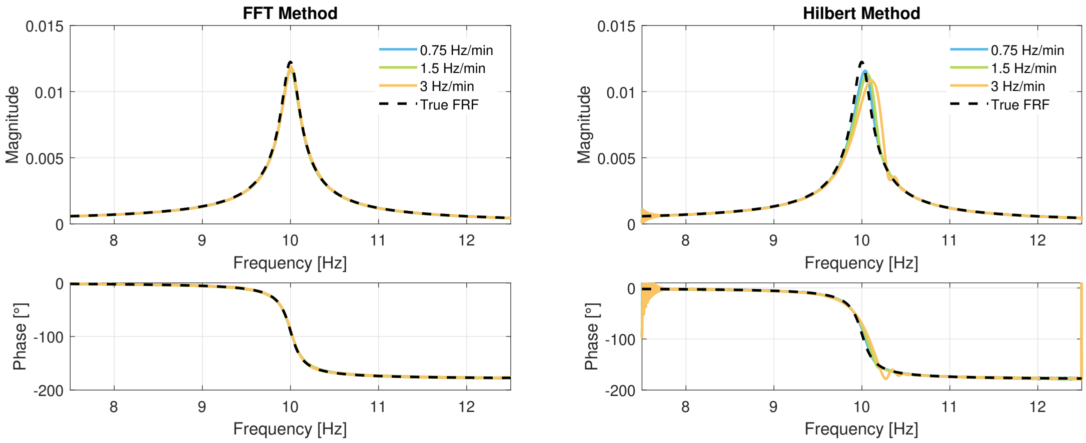

(a) FFT Method

(b) Hilbert Method

Figure 4.8 – SDOF system FRF obtained from sweep test at different sweep rate

In [6] the authors detail advantages and disadvantages of the most common ways of analyzing sweep sine tests, giving recommendations on how to obtain a proper FRF estimation. As for the impact test post-processing, the choice here is again between frequency domain and time domain methods.

Considering frequency-domain methods, these all involve performing the Discrete Fourier Transform, or simply a Fast Fourier Transform (see [6]) on the test time history data. This family of methods is very simple to implement but the main disadvantage concerns the frequency resolution, which is directly linked to the time signal length. The latter has to be quite big, in order to have an acceptable frequency resolution to be able to perform a proper modal identification on the resulting FRF.

On the other hand, considering time-domain methods, these all involve the calculation of the time signal envelope. The most common technique is the Hilbert Transform [3, 5]. By using time-domain methods, it's assumed that the FFT of the sweep data can be approximated by the signal envelope. The FRF can then be obtained by dividing the output envelope by the input one.

The problem of both frequency and time domain-methods, however, is that, if the sweep rate is too high, distortion in the calculated FRF may occur. In figure 4.8, evaluation of FRF with FFT (fig. 4.8a) and Hilbert Transform (fig. 4.8b) are shown for different sweep rates on a simple SDOF linear system. It can be seen that, while for the FFT method the distortion slightly affects only the FRF amplitude, for the Hilbert Transform there is a consistent shift in frequency if the sweep rate is too high. From this it's possible to understand the importance of a well chosen sweep rate and a correct test execution in order to have a correct estimate.

The development of a new method using Kalman filter is motivated by the intent of taking advantage of the better frequency resolution property of time-domain methods, while reducing the FRF distortion. Additionally, the other objective is to be able to track signal harmonics, that can show up when the tested system is nonlinear.

As it was carried out in section 4.2.1 for impact tests, in the next section the model implemented in the Kalman filter will be developed for sweep tests. The method is a Single-Input-Multiple-Output method (SIMO). The method aim is to track signals envelopes and the instantaneous oscillation frequency, in order to be subsequently used for nonlinear modal identification and experimental FRF visualization.

4.3.2 Model Formulation

In order to develop a model adapted to sweep sine test, it's important to understand with which kind of data we have to deal during these kind of tests. Concerning input signals, we can generally have N input measurements. For example, in a case of base excitation on an electromagnetic shaker, the base input acceleration can be measured in several points. Concerning the output signals, there are M sensors measuring the system response. In addition, there is an array Λ of H harmonics to track defined as:

$$\Lambda = [\lambda_1, \lambda_2, \cdots, \lambda_H] \quad \lambda_1 = 1 \tag{4.70}$$

where the array elements are the coefficients by which the first instantaneous harmonics oscillating frequency ω_{out} has to be multiplied to obtain higher-order harmonics.

4.3.2.1 State-space transition part

Differently from the impact test formulation, in this case we don't track the natural frequency and damping of the system but we simply reconstruct the signal in order to find its instantaneous oscillation frequency, amplitude and phase. The tracked signal has the same form as the generic sine signal defined in eq. 4.42. The assumptions made are again that the signal amplitude and frequency are slowly modulated. In order to obtain a good FRF estimate it's necessary to track separately input and output instantaneous frequencies of the system.
Starting from the tracking of the input signal part, we can start defining the following basic block:

$$F_{in,k} = \begin{bmatrix} \cos(\omega_{in,k}\Delta t) & -\sin(\omega_{in,k}\Delta t) \\ \sin(\omega_{in,k}\Delta t) & \cos(\omega_{in,k}\Delta t) \end{bmatrix} \tag{4.71}$$

Secondly, considering the input measure point i, we can define:

$$x_k^{in,i} = (x_{1,k}^{in,1}, x_{2,k}^{in,i})^\intercal \tag{4.72}$$

The state-space transition function for the part dedicated to the input signals can be written as:

$$f(X_k^{in}) = F_k^{in} X_k^{in} = \begin{bmatrix} F_{in,k} & & & & \\ & F_{in,k} & & & \\ & & \ddots & & \\ & & & F_{in,k} & \\ & & & & 1 \end{bmatrix} \begin{pmatrix} x_k^{in,1} \\ x_k^{in,2} \\ \vdots \\ x_k^{in,N} \\ \omega_{in,k} \end{pmatrix} \tag{4.73}$$

recalling that $\omega_{in,k}$ is the instantaneous oscillating frequency of the input signals.
Regarding the tracking of the output part, the tracked frequency is only one, which is the fundamental $\omega_f = \lambda_1 \omega_{out}$ (with $\lambda_1 = 1$), while the harmonics are assumed to be their exact multiples. The basic block including the harmonics can be written as:

$$F_{\lambda_n,k} = \begin{bmatrix} \cos(\lambda_n \omega_{out,k}\Delta t) & -\sin(\lambda_n \omega_{out,k}\Delta t) \\ \sin(\lambda_n \omega_{out,k}\Delta t) & \cos(\lambda_n \omega_{out,k}\Delta t) \end{bmatrix} \tag{4.74}$$

Considering the i^{th} output measure point and the n^{th} harmonic, we can define:

$$x_k^{\lambda_n,i} = (x_{1,k}^{\lambda_n,1}, x_{2,k}^{\lambda_n,i})^\mathsf{T} \tag{4.75}$$

The state-space transition part dedicated to the output signals can now be written as

$$f(\mathrm{X}_k^{out}) = \mathrm{F}_k^{out}\mathrm{X}_k^{out} = \begin{bmatrix} \mathrm{F}_{\lambda_1,k} &&&&&&&&&& \\ & \ddots &&&&&&&&& \\ && \mathrm{F}_{\lambda_1,k} &&&&&&&& \\ &&& \mathrm{F}_{\lambda_2,k} &&&&&&& \\ &&&& \ddots &&&&&& \\ &&&&& \mathrm{F}_{\lambda_2,k} &&&&& \\ &&&&&& \ddots &&&& \\ &&&&&&& \mathrm{F}_{\lambda_\mathrm{H},k} &&& \\ &&&&&&&& \ddots && \\ &&&&&&&&& \mathrm{F}_{\lambda_\mathrm{H},k} & \\ &&&&&&&&&& 1 \end{bmatrix} \begin{pmatrix} x_k^{\lambda_1,1} \\ \vdots \\ x_k^{\lambda_1,\mathrm{M}} \\ x_k^{\lambda_2,1} \\ \vdots \\ x_k^{\lambda_2,\mathrm{M}} \\ \vdots \\ x_k^{\lambda_\mathrm{H},1} \\ \vdots \\ x_k^{\lambda_\mathrm{H},\mathrm{M}} \\ \omega_{out,k} \end{pmatrix} \tag{4.76}$$

At this point it's possible to put the input and output part together to obtain the total state-space transition part as:

$$f(\mathrm{X}_k) = \mathrm{F}_k\mathrm{X}_k = \begin{bmatrix} \mathrm{F}_k^{in} & \\ & \mathrm{F}_k^{out} \end{bmatrix} \begin{pmatrix} \mathrm{X}_k^{in} \\ \mathrm{X}_k^{out} \end{pmatrix} \tag{4.77}$$

The total system dimension is $\mathrm{N}_{in} + \mathrm{HN}_{out}$, where H is the number of harmonics considered, including the fundamental one.

4.3.2.2 Observation function

Now we need to find the observation function. As for the cases treated previously, the only observed data is the real part of the input and output sensors. Concerning the inputs, the observation function is directly the real part tracked by the filter, as follows:

$$h(\mathrm{X}_k^{in}) = \begin{pmatrix} x_{1,k}^{in,1} \\ x_{1,k}^{in,2} \\ \vdots \\ x_{1,k}^{in,\mathrm{N}} \end{pmatrix} \tag{4.78}$$

Regarding the outputs, the observed data correspond to the sum of the real part of all the harmonics for each measure point. It can be written as:

$$h(\mathrm{X}_k^{out}) = \begin{pmatrix} \sum\limits_{h=1}^{\mathrm{H}} x_{1,k}^{\lambda_h,1} \\ \sum\limits_{h=1}^{\mathrm{H}} x_{1,k}^{\lambda_h,2} \\ \vdots \\ \sum\limits_{h=1}^{\mathrm{H}} x_{1,k}^{\lambda_h,\mathrm{M}} \end{pmatrix} \tag{4.79}$$

The total observation function becomes:

$$h(\mathrm{X}_k) = \begin{pmatrix} h(\mathrm{X}_k^{in}) \\ h(\mathrm{X}_k^{out}) \end{pmatrix} \tag{4.80}$$

4.3.2.3 FRF Calculation

Obtaining the FRF estimation is a straightforward operation. Inputs and outputs amplitude and phase of each sensors and harmonics are obtained with eqs. 4.43 and can be grouped into arrays as:

$$\mathrm{A}_{in,k} = \left[\mathrm{A}_k^{in,1}, \mathrm{A}_k^{in,2}, \ldots, \mathrm{A}_\mathrm{N}^{in,1}\right]; \tag{4.81a}$$

$$\mathrm{A}_{out,k} = \left[\mathrm{A}_k^{\lambda_1,1}, \mathrm{A}_k^{\lambda_1,2}, \ldots, \mathrm{A}_k^{\lambda_1,\mathrm{M}}, \ldots, \mathrm{A}_k^{\lambda_\mathrm{H},1}, \mathrm{A}_k^{\lambda_\mathrm{H},2}, \ldots, \mathrm{A}_k^{\lambda_\mathrm{H},\mathrm{M}}\right]; \tag{4.81b}$$

$$\phi_{in,k} = \left[\phi_k^{in,1}, \phi_k^{in,2}, \ldots, \phi_\mathrm{N}^{in,1}\right]; \tag{4.81c}$$

$$\phi_{out,k} = \left[\phi_k^{\lambda_1,1}, \phi_k^{\lambda_1,2}, \ldots, \phi_k^{\lambda_1,\mathrm{M}}, \ldots, \phi_k^{\lambda_\mathrm{H},1}, \phi_k^{\lambda_\mathrm{H},2}, \ldots, \phi_k^{\lambda_\mathrm{H},\mathrm{M}}\right]; \tag{4.81d}$$

Then, since the input can be measured by different sensors (and it's advisable to do so for control reasons) but it's unique, the instantaneous input amplitude and phase are calculated as the input sensors instantaneous averages $\bar{\mathrm{A}}_{in,k}$ and $\bar{\phi}_{in,k}$. Then, the instantaneous FRF amplitude for each measurement point is obtained simply by dividing the output amplitude by the input one as:

$$\mathrm{A}_{i,k} = \frac{(\mathrm{A}_{out,k})_i}{\bar{\mathrm{A}}_{in,k}} \tag{4.82}$$

Regarding the FRF phase, it is obtained as the difference of phase between the input and the output as:

$$\phi_{i,k} = (\phi_{out,k})_i - \bar{\phi}_{in,k} \tag{4.83}$$

The FRF phase is calculated only for the first harmonic, since for the rest of them the phase difference between an higher-order harmonic and the input phase is meaningless and it will not be shown in the results. The FRF can be truly calculated only for the first harmonic or fundamental frequency. This is because, even if higher harmonics exist, the input spectrum does not include these higher harmonics, but only the fundamental. Therefore, the FRF amplitudes obtained with eq. 4.82 for the higher harmonics are not part of true FRFs, but they are important to evaluate the non-linearity entity.

4.3.3 Modal Identification with the FORCEVIB method

Differently from the Kalman filter used for impact tests described in section 4.2, the developed method for sweep tests doesn't perform a direct modal identification. In order to do this, a slightly modified version of the FORCEVIB method [4] is used. The latter is a nonlinear modal analysis method which utilizes the Hilbert transform to obtain modal parameters from forced systems. It derives from another method, called FREEVIB [3], used on free vibrating systems. At first the original FORCEVIB method will be described. Then it will be shown how it has been used in combination with the UKF. Let's consider a quasi-linear forced SDOF system with viscous damping, expressed in its analytic form as:

$$\ddot{Y} + 2h_0(A)\dot{Y} + \omega_0^2(A)Y = X/m \tag{4.84}$$

where the undamped natural frequency ω_0 and the damping coefficient $h_0(A) = \zeta(A)\omega_0(A)$ are nonlinear function of the oscillation amplitude A. The system solution Y and the forced excitation X are both expressed in the analytic form and, by using the latter for the system solution it's possible to obtain the following equation:

$$Y\left[\frac{\ddot{A}}{A} - \omega^2 + \omega_0^2 + 2h_0\frac{\dot{A}}{A} + j\left(2\frac{\dot{A}}{A}\omega + \dot{\omega} + 2h_0\omega\right)\right] = X(t)/m \tag{4.85}$$

where A is the envelope of the system solution Y and ω its instantaneous frequency. By solving eq. 4.85 for its real and imaginary parts, it's possible to find the expressions of instantaneous modal parameters:

$$\omega_0^2(t) = \omega^2 + \frac{\alpha(t)}{m} - \frac{\beta(t)\dot{A}}{\omega m A} - \frac{\ddot{A}}{A} + \frac{2\dot{A}^2}{A^2} + \frac{\dot{A}\dot{\omega}}{A\omega} \tag{4.86a}$$

$$h_0(t) = \frac{\beta(t)}{2\omega m} - \frac{\dot{A}}{A} - \frac{\dot{\omega}}{2\omega} \tag{4.86b}$$

where m is the modal mass, while $\alpha(t)$ and $\beta(t)$ are the real and imaginary parts of the input and output signal ratio:

$$\alpha(t) = \Re\left[\frac{X(t)}{Y(t)}\right] \tag{4.87a}$$

$$\beta(t) = \Im\left[\frac{X(t)}{Y(t)}\right] \tag{4.87b}$$

With respect to the modal mass m, it is a priori unknown, but it can be considered constant. It has to be estimated by finding the slope of the line fitting the denominator (on the x-axis) and the numerator (on the y-axis) of the following expression:

$$m = \frac{\Delta\left(\alpha - \frac{\beta\dot{A}}{\omega A}\right)}{\Delta\left(-\omega^2 + \frac{\ddot{A}}{A} - \frac{2\dot{A}^2}{A^2} - \frac{\ddot{A}\dot{\omega}}{A\omega}\right)} \tag{4.88}$$

The classic method follows this order of actions:

1. The Hilbert transform is applied to the input and output signals in order to obtain their analytic form;

2. The output envelope A and phase ϕ are calculated with eq. 4.43;

3. The instantaneous frequency ω is obtained by deriving the phase;
4. The envelope A is derived to obtain $\dot{A}$ and $\ddot{A}$;
5. The instantaneous frequency ω is derived to obtain $\dot{\omega}$;
6. $\alpha(t)$ and $\beta(t)$ are calculated with eqs. 4.87;
7. The modal mass m is approximated by the line fitting procedure of denominator and numerator of eq. 4.88;
8. The instantaneous modal parameters are obtained with eqs. 4.86.

. Now, the main problems with this procedure are the following:

- The double derivation of the phase can produce substantial errors on the identified parameters;
- The Hilbert transform is naturally less precise in the presence of signal noise.

The coupled usage of Kalman filter and FORCEVIB can be more accurate. In fact, through the application of the UKF on sweep sine tests signals, the instantaneous oscillating frequency ω is **directly** identified and it doesn't have to be derived. Furthermore, the Kalman filter is naturally more capable of handling noisy signals. Therefore, the used method consists of the same equations of the FORCEVIB method, but the necessary data are calculated through the UKF instead of the Hilbert transform.

4.3.4 Test Case

As provided for the impact case, also the sweep method is tested on the SDOF nonlinear system shown in fig. 4.4. A series of sweep sine excitation profiles at different amplitudes have been numerically simulated on the system in order to apply the method previously described. The first step, performed through the UKF, is the calculation of input and output signal amplitude and instantaneous frequency. In addition, also the amplitude of the third harmonic is detected. Figure 4.9 shows the reconstructed input and output signals, together with their tracked amplitudes, for a sweep sine test of amplitude A = 10N. For these tests it was assumed that the output signal could be well represented by the first and third harmonics frequencies. Their amplitudes are shown in fig. 4.10.
Concerning the instantaneous frequency tracking, the input frequency, the first and third harmonics output frequencies are given in fig. 4.11. The black dashed lines represent the *theoretical* excitation frequency imposed to the system: it's possible to see that, while the input tracked frequency is exactly the same as the *theoretical* one, the output tracked frequencies don't follow it exactly. We'll discuss more this aspect later in this section. It can be observed that, at the beginning, there is a very short transient in order for the Kalman filter to correctly track the frequencies and signals.
Once the signals amplitudes and instantaneous frequencies are tracked, the next step is to perform the nonlinear identification on the sweep tests (upward and downward) at several excitation amplitudes using the FORCEVIB method, described in section 4.3.3. The nonlinear evolution of natural frequency and damping as a function of the mass displacement amplitude are therefore obtained in fig. 4.12, compared to the theoretical implemented Iwan model. It's important to recall the fact that, at the transition between micro-slip and macro-slip there exists a discontinuity which is not representative of the real behavior but it's due to the limit in the analytic formulation of the 4-parameter Iwan model.

In section 4.3.2.3 it was explained how to obtain the frequency response function from the results of the Kalman filter procedure. We consider now the same SDOF nonlinear system, but

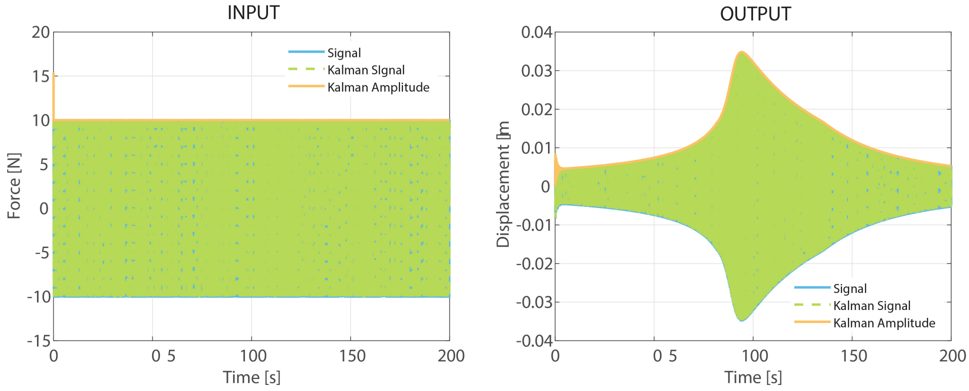

Figure 4.9 – Signal and amplitude tracking on input and output with Kalman filter for the SDOF test case

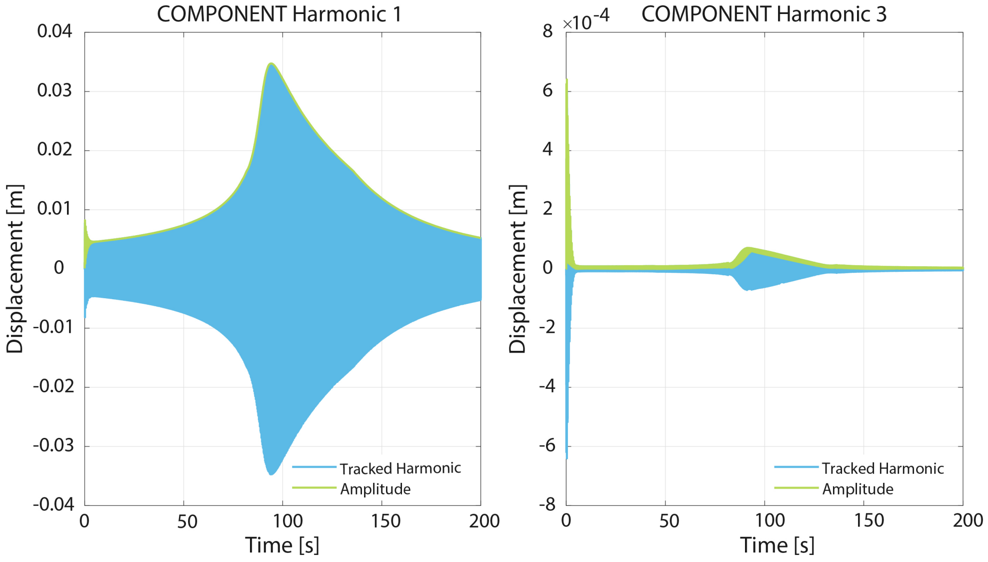

Figure 4.10 – Harmonic components tracking on output signal for the SDOF test case

this time we remove the Iwan element and we replace it with a Duffing stiffness term so that eq. 4.67 becomes:

$$m\ddot{x} + c\dot{x} + kx + k_d x^3 = \mathrm{F}(t) \tag{4.89}$$

We can now perform an high excitation upward sweep sine test on the system and apply the Kalman filter method to calculate the FRF amplitude and phase with eqs. 4.82-4.83. Furthermore, instead of plotting them as a function of the *theoretical* input frequency, the FRF are plotted as a function of the **instantaneous** output frequency detected by the Kalman filter. The result is given in fig. 4.13: the light blue curve represents the FRF obtained with the Kalman filter procedure, plotted against the **input** frequency, while the green curve represents the same FRF, but this time plotted against the tracked output **instantaneous** frequency. In order to make a simple distinction between the two, we will call the first one *classical FRF* and the second *Kalman FRF*, as shown in the figure's legend. The black dashed line represents the theoretical nonlinear evolution of the natural frequency, the so called *backbone*.

Furthermore, fig.4.13b represent the same FRFs of fig.4.13a, but in this cased a light smoothing

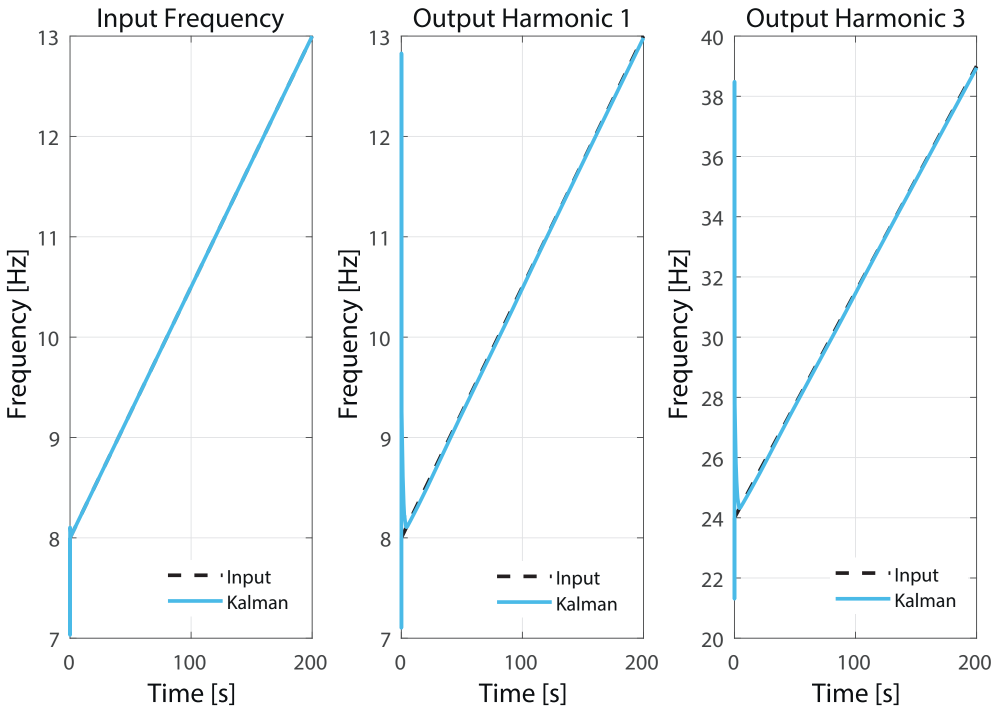

Figure 4.11 – Frequency tracking on input and output signals for the SDOF test case

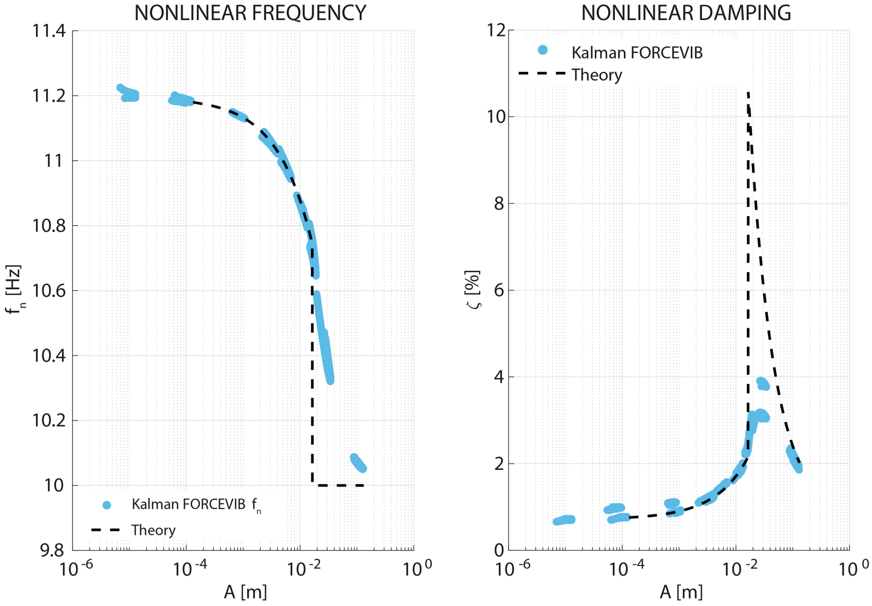

Figure 4.12 – Nonlinear frequency and damping evolution calculated with the FORCEVIB method for the SDOF test case

procedure is applied. It's possible to see that, until the natural frequency of the system, the *classical FRF* and *Kalman FRF* are essentially the same. However, once the natural frequency is passed, the behaviors of the two are considerably different: for the *classical FRF* there is a jump because the considered frequency is the one of the input, while for the *Kalman FRF* it can be noted that the system *tries* to follow its nonlinear branch, especially if we look at the smoothed version. The ability to find the *Kalman FRF* is one of the reason why the Kalman fil-

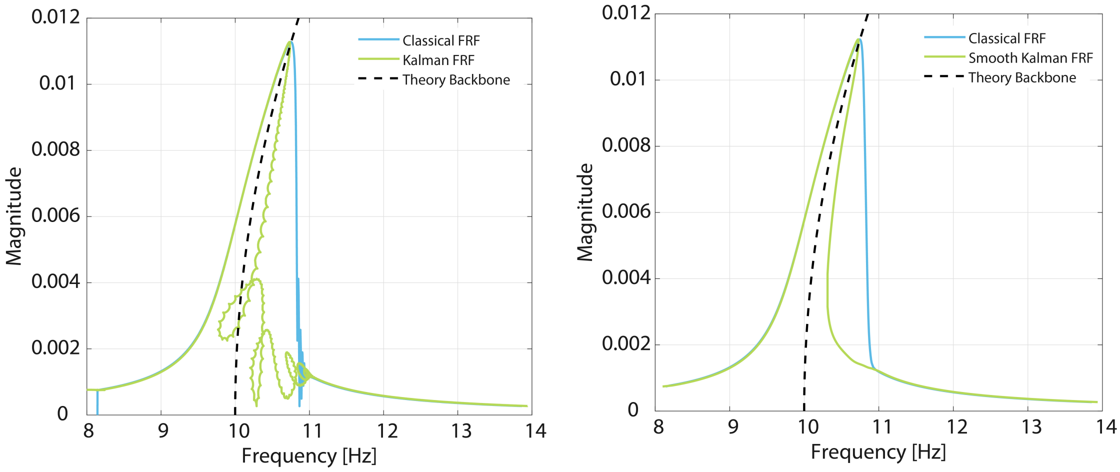

(a) Raw FRF of the Duffing SDOF system

(b) Smooth FRF of the Duffing SDOF system

Figure 4.13 – FRF of the Duffing SDOF system obtain through the Kalman filter procedure on a sweep sine test

ter technique applied on sweep sine testing can provide more and better pieces of information compared to Hilbert-based methods.
In the next section Kalman filter will be applied to random testing, completing the toolbox and fulfilling the objectives of this chapter.

4.4 Kalman Filter for random vibration testing

The last tool created in this work concerns random vibration testing. In this kind of tests, a structure is excited by a random vibration profile defined by a certain Power Spectral Density function (PSD). Random vibration testing is the most common type of validation and qualification tests. In fact, the majority of vibration environments are predominantly characterized by random vibration conditions. Therefore, the advantage of random vibrations is that they are more realistic than the mono-component sinusoidal vibrations seen earlier. However, when used for modal identification, random vibration tests tends to give a linearized version of the frequency response functions [16] depending on the amplitude of the PSD, which could lead to leave unnoticed the system's nonlinearities. The identification methods on random vibration tests are based either on a linearization approach [8, 9, 19, 23] or on a time-domain approach using ARMA models [20, 26].
In this section a post-processing method using Kalman filter will be developed. The approach will be quite different from the one used for impact and sine sweep testing. The method can be extended to a multitude of other mechanical systems and can be used for general parameter identification. In particular, the focus will be placed on modal identification of a structure undergoing random vibrations: a linear method will be described and a nonlinear extension will be proposed.

4.4.1 Differential equations inside Kalman

In the methods developed in sections 4.2-4.3, the system evolution between the step k and the step $k+1$ was described by the state-transition function $f(\mathrm{X}_k)$. In the previous cases these functions could be represented in a matrix form. The novelty in the case of random vibrations is that it can be replaced by the differential equations system representing the system. In the following section the method will be theoretically explained and afterwards it will be applied on a simple general case. Then the method will be developed for the actual need of this work, i.e. nonlinear modal identification.

4.4.1.1 Method description

The general case of the method considers a system that can be described by a set of differential equations in its generic form:

$$y^{(n)} = \mathbf{F}\left(t, y', y'', ..., y^{(n-1)}\right) \tag{4.90}$$

where y is a vector whose terms are functions of the time t.
The system state vector at the step k can be generally written as:

$$\mathrm{X}_k = y_k, y'_k, y''_k, y_k^{(n-1)}, p_{1,k}, p_{2,k}, ..., p_{m,k} \tag{4.91}$$

where $p_1, p_2, ..., p_m$ are m unknown parameters that are tracked by the Kalman filter.
The Kalman filter formulation used for this application is the unscented version (UKF), as it was already the case for the impact and sweep examples. Therefore the method follows the algorithm represented by eqs. 4.23-4.31. The main feature of the presented method is that the differential equations system is solved between the time t_{k-1} and t_k at each time step as the state transition function $f(\chi_{k-1})$. Then the observation function $h(\chi_k)$, that can either be linear or nonlinear depending on the system, extracts the data to compare it to the known ones.
In order to show how this works, a general example will be provided in the next section.

4.4.1.2 General Example

The problem chosen to show a general parameter identification is represented in fig. 4.14. It consists of a three Degrees-Of-Freedom dynamic system with three springs and three viscous dampers. The system can be described by the following differential equation system:

$$\mathrm{M}\ddot{y} + \mathrm{C}\dot{y} + \mathrm{K}y = \mathrm{F}(t) \tag{4.92}$$

where:

$$\mathrm{M} = \begin{bmatrix} m_1 & 0 & 0 \\ 0 & m_2 & 0 \\ 0 & 0 & m_3 \end{bmatrix} \quad \mathrm{C} = \begin{bmatrix} c_1 & 0 & 0 \\ 0 & c_2 & 0 \\ 0 & 0 & c_3 \end{bmatrix} \quad \mathrm{K} = \begin{bmatrix} k_1 + k_2 & -k_2 & 0 \\ -k_2 & k_2 + k_3 & -k_3 \\ 0 & -k_3 & k_3 \end{bmatrix} \tag{4.93}$$

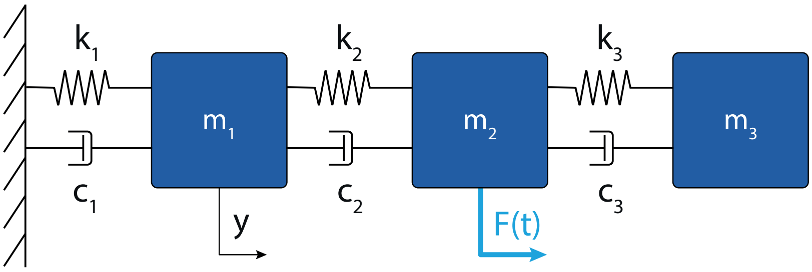

Figure 4.14 – Three masses dynamic system used as a general example

A numerical simulation of a random force $\mathrm{F}(t)$ application on the mass m_2 is performed, obtaining the displacement profile of the three masses, which are the observed data to post-process with the Kalman filter. A gaussian noise is added to the numerically obtained data to simulate measurement noise. At this point we assume that we actually don't know the values of the two stiffnesses k_1 and k_3 and that we want to identify them from the displacement histories y_1, y_2, and y_3. The vector of state variables can then be written as:

$$x = \{y_1, y_2, y_3, k_1, k_3\}^\mathsf{T} = \{y, k_1, k_3\}^\mathsf{T} \tag{4.94}$$

The differential equations system described by eqs. 4.92-4.93 is the one that is going to be solved at each time step and updated with the tracked parameters. In fact, after each correction step, the tracked parameters are injected again in the system matrices — in this case the stiffness matrix K — in order to converge to the correct solution.

Figure 4.15 contains the results for this simple case. The top graph shows the displacement tracking, which is accurate, while the two bottom plots display the tracking of the two researched parameters k_1 and k_3. The error after the initial transient part is always under 3% of the stiffness value, which is a good result. It can also be observed that the convergence time is less than 0.5 seconds for both stiffnesses: it only takes a small number of cycles to converge to the solution.

The method explained and demonstrated here is very general and can be applied theoretically to any system whose evolution can be described by an ordinary differential equations system. In the next sections the same approach will be exploited for modal identification of random tests.

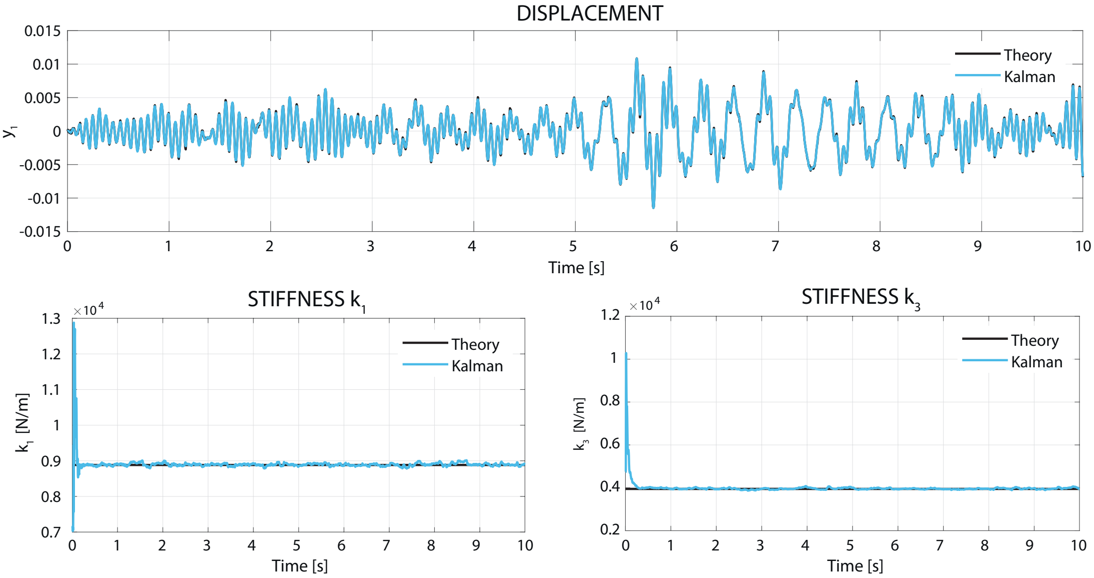

Figure 4.15 – Results for the displacement and stiffness tracking for the three-masses system undergoing random excitation

4.4.2 Linear Modal Formulation

The goal of this work is to find post-processing tools for vibration testing using Kalman filter. Here a linear method is developed to track natural frequencies and damping as the founding basis for a subsequent nonlinear formulation capable of identifying systems' non-linearities.

Here we assume that a full dynamic system described by eq. 4.92 can be projected on the modal base through the modal transformation:

$$q = \Phi^{-1} y \quad \text{with} \quad q\,[\mathrm{N} \times m] \quad ; \quad \Phi\,[n \times \mathrm{N}] \quad ; \quad y\,[n \times m] \tag{4.95}$$

where Φ is the mode shape matrix, y is the *real* displacement, and q is the projected *modal* displacement. In addition, N is the number of measurement points, n is the number of sensors, and m is the number of considered modes. The modal transformation is applied to eq. 4.92 to obtain the linear modal system:

$$\mathrm{M}_q \ddot{q} + \mathrm{C}_q \dot{q} + \mathrm{K}_q q = \Phi^{\mathsf{T}} \mathrm{F}(t) \tag{4.96}$$

where $q, \dot{q}, \ddot{q}$ are respectively the system displacement, velocity and acceleration projected on the modal basis, and where the modal matrices are represented by:

$$\mathrm{M}_q = \begin{bmatrix} 1 & 0 & \cdots & 0 \\ 0 & 1 & \cdots & 0 \\ \vdots & \vdots & \ddots & \vdots \\ 0 & 0 & \cdots & 1 \end{bmatrix} \quad \mathrm{C}_q = \begin{bmatrix} 2\zeta_1\omega_1 & 0 & \cdots & 0 \\ 0 & 2\zeta_2\omega_2 & \cdots & 0 \\ \vdots & \vdots & \ddots & \vdots \\ 0 & 0 & \cdots & 2\zeta_n\omega_n \end{bmatrix} \quad \mathrm{K}_q = \begin{bmatrix} \omega_1^2 & 0 & \cdots & 0 \\ 0 & \omega_2^2 & \cdots & 0 \\ \vdots & \vdots & \ddots & \vdots \\ 0 & 0 & \cdots & \omega_n^2 \end{bmatrix} \tag{4.97}$$

At this point, we assume having the three following ingredients:

- Numerically obtained mode shape matrix Φ of the system under study;
- Displacement y, velocity $\dot{y}$, or acceleration $\ddot{y}$ time history related to a random test, preferably at different locations;
- Input force time history $\mathrm{F}(t)$ related to the same random test.

The goal is to track and determine the natural frequencies and damping ratios of the modes excited by the random profile. In a case in which the displacement is available, the variable state vector x is written as:

$$x = \{q, \omega_1, \omega_2, ..., \omega_n, \zeta_1, \zeta_2, ..., \zeta_n\}^{\mathsf{T}} \tag{4.98}$$

where ω_i and ζ_i are respectively the i$^{\text{th}}$ natural frequency and damping ratio. The differential equations system described by eqs. 4.96-4.97 is the one that is going to be solved at each time step and updated with the tracked parameters.

However, for a linear system identification the described method is probably not the best option available. Nevertheless, it can be used for slightly nonlinear systems or as a base for the full nonlinear approach described in the next section.

4.4.3 Nonlinear Modal Formulation

In chapters 2 and 3 we have seen that bolted joints nonlinearity strongly depends on how the contact interface is excited and where the contact actually takes place. Also, an important aspect is that, if the nonlinearity is not excited for a certain mode, the latter will be pretty much linear. The modal basis Φ, that from here on we will refer to as Φ_y, only offers us a view on the structure displacement, and it doesn't give us any additional information. In order to link a particular type of mode deformation in the contact region to a certain nonlinearity function, we will use the modal strain matrix Φ_ϵ. Each term of this matrix can be written as $\Phi_{\epsilon_{i,j}}$, where i

is the node number and j is the mode, and it consists of the following modal strain matrix:

$$\Phi_{\epsilon_{i,j}} = \begin{bmatrix} \phi_{\epsilon_{11}} & \phi_{\epsilon_{12}} & \phi_{\epsilon_{13}} \\ \phi_{\epsilon_{21}} & \phi_{\epsilon_{22}} & \phi_{\epsilon_{23}} \\ \phi_{\epsilon_{31}} & \phi_{\epsilon_{32}} & \phi_{\epsilon_{33}} \end{bmatrix}_{i,j} \qquad \text{i}^{\text{th}} \text{ point, j}^{\text{th}} \text{ mode} \tag{4.99}$$

Assuming the strain components matrix to be symmetric ($\phi_{\epsilon_{i,j}} = \phi_{\epsilon_{j,i}}$), the total modal strain matrix Φ_ϵ will be a three-dimensional matrix of dimensions [6 × N × M]. The relations with the real quantities can be written as:

$$y = \Phi_y q_y \qquad \epsilon_{11} = \Phi_{\epsilon_{11}} q_{\epsilon_{11}}, \quad \epsilon_{22} = \Phi_{\epsilon_{22}} q_{\epsilon_{22}}, \quad ... \tag{4.100}$$

where, in order to summarize, we can define the following nomenclature as:

- Φ_y: mode shape matrix;
- Φ_ϵ: modal strain matrix;
- y: real displacement;
- ϵ: real strain;
- q_y: modal displacement;
- q_ϵ: modal strain.

The second step of the method is to write natural frequencies and damping ratios as functions of the modal strain q_ϵ. However, only the modal strain components that actually affect the nonlinearity will be used. A possible way of expressing the nonlinear behavior of natural frequencies and damping ratios could be the following:

$$\omega_j = 1 + \sum_k \alpha_{jk} q^k_{\epsilon_{11,j}} + \sum_k \beta_{jk} q^k_{\epsilon_{22,j}} + ... \tag{4.101}$$

$$\zeta_j = 1 + \sum_k \gamma_{jk} q^k_{\epsilon_{11,j}} + \sum_k \lambda_{jk} q^k_{\epsilon_{22,j}} + ... \tag{4.102}$$

where α, β, γ, λ are the parameters describing the nonlinear frequency and damping behavior. The variable state vector shown in eq. 4.98 can therefore be updated to:

$$x = \{q_1, q_2, ..., q_M, \omega_1, \omega_2, ..., \omega_M, \zeta_1, \zeta_2, ..., \zeta_M, \alpha_{jk}, \beta_{jk}, ..., \gamma_{jk}, \lambda_{jk}, ...\} \tag{4.103}$$

Considering the physics behind jointed structures, it can be foreseeable that the modal strain components involved in eq. 4.102 will mainly be the tangential components.
The drawback of this method is that the state vector x dimension can become quite large, depending on how many parameters are necessary to describe the nonlinearity. This can make the parameter initialization a very complicated task.
The method shown here was only theoretically developed and it has not been implemented for the analysis of real systems. It was presented as a possible approach to nonlinear modal analysis for random tests.

4.5 Conclusion

In this chapter a set of methods based on Kalman filter tool was developed. It was shown that the Kalman filter is an incredibly flexible tool, that can be used for a large number of different systems and applications in very different fields, from econometrics to engineering. Furthermore, its performances are remarkable. However, flexibility and performances come with a price, which is the parameters' initialization task. It was shown that, while for the initial state x_0 and its covariance P_0 is possible to automate the task efficiently, for the model covariance vector Q and for the measurements covariance vector R the situation is quite different. A universal approach has not been found yet and the hypothesis of their *gaussianity* is a strong assumption that requires an extensive investigation from the whole research community orbiting around Kalman filter. In fact, without an automated approach, the determination of an optimal set of parameters involves a trial and error process that can become quite long and frustrating, usually requiring a certain level of experience with Kalman filters and a good knowledge of the implemented model and variables.

Beside these disadvantages, the Kalman filter adaptations for impact and sweep sine vibration testing have both been successfully tested for a nonlinear modal identification of SDOF test case. A general method including the solution of an ordinary differential equations inside the Kalman filter have been developed and implemented, while its adaptation for random testing have been developed but not yet implemented.

In the next chapter some of the tools described here will be applied on experimental data gathered throughout the CLIMA project.

Bibliography

[1] Del Moral, P. (1995). Nonlinear Filtering Using Random Particles. *Theory Probab. Appl.*, 40(4):690–701. 88

[2] Dion, J.-L., Stephan, C., Chevallier, G., and Festjens, H. (2013). Tracking and removing modulated sinusoidal components: A solution based on the kurtosis and the Extended Kalman Filter. *Mechanical Systems and Signal Processing*, 38(2):428–439. 91

[3] Feldman, M. (1994a). Non-linear system vibration analysis using Hilbert transform–I. Free vibration analysis method 'Freevib'. *Mechanical Systems and Signal Processing*, 8(2):119–127. 93, 101, 105

[4] Feldman, M. (1994b). Non-linear system vibration analysis using Hilbert transform-II. Forced vibration analysis method 'Forcevib'. *Mechanical Systems and Signal Processing*, 8(3):309–318. 105

[5] Feldman, M. (2011). Hilbert transform in vibration analysis. *Mechanical Systems and Signal Processing*, 25(3):735–802. vi, 92, 93, 101

[6] Gloth, G. and Sinapius, M. (2004). Analysis of swept-sine runs during modal identification. *Mechanical Systems and Signal Processing*, 18(6):1421–1441. 101

[7] Huang, N. E., Shen, Z., Long, S. R., Wu, M. C., Snin, H. H., Zheng, Q., Yen, N. C., Tung, C. C., and Liu, H. H. (1998). The empirical mode decomposition and the Hubert spectrum for nonlinear and non-stationary time series analysis. *Proceedings of the Royal Society A: Mathematical, Physical and Engineering Sciences*, 454(1971):903–995. 94

[8] Iwan, W. D. (1973). A Generalization of the Concept of Equivalent Linearization. 8:279–281. 109

[9] Iwan, W. D. and Mason, A. B. (1980). Equivalent linearization for systems subjected to non-stationary random excitation. *International Journal of Non-Linear Mechanics*, 15(2):71–82. 109

[10] Jouin, M., Gouriveau, R., Hissel, D., Péra, M. C., and Zerhouni, N. (2016). Particle filter-based prognostics: Review, discussion and perspectives. *Mechanical Systems and Signal Processing*, 72-73:2–31. 89

[11] Julier, S. (2003). The spherical simplex unscented transformation. *Proceedings of American Control Conference, 2003.*, 3:2430–2434. 88

[12] Julier, S. and Uhlmann, J. (2004). Unscented Filtering and Nonlinear Estimation. *Proceedings of the IEEE*, 92(3):401–422. 85

[13] Julier, S. J. and Uhlmann, J. K. (1997). New extension of the Kalman filter to nonlinear systems. *Spie 3068*, page 182. 84

[14] Kalman, R. E. (1960). A New Approach to Linear Filtering and Prediction Problems. *Journal of Basic Engineering*, 82(1):35. 82

[15] Kim, K. and Park, C. G. (2010). Non-symmetric unscented transformation with application to in-flight alignment. *International Journal of Control, Automation and Systems*, 8(4):776–781. 88

[16] Maia, N. M. and Silva, J. M. (2001). Modal analysis identification techniques. *Philosophical Transactions of the Royal Society A: Mathematical, Physical and Engineering Sciences*, 359(1778):29–40. 109

[17] Masoumnezhad, M., Jamali, A., and Nariman-Zadeh, N. (2015). Optimal design of symmetrical/asymmetrical sigma-point Kalman filter using genetic algorithms. *Transactions of the Institute of Measurement and Control*, 37(3):425–432. 88

[18] McGee, L. A. and Schmidt, S. F. (1985). Discovery of the Kalman Filter as a Practical Tool for Aerospace and Industry. (November):21. 84

[19] Miles, R. N. (1989). An approximate solution for the spectral response of Duffing's oscillator with random input. *Journal of Sound and Vibration*, 132(1):43–49. 109

[20] Pi, Y. L. and Mickleborough, N. C. (1989). Modal Identification of Vibrating Structures Using ARMA Model. *Journal of Engineering Mechanics*, 115(10):2232–2250. 109

[21] Schneider, R. and Georgakis, C. (2013). How to NOT make the extended kalman filter fail. *Industrial and Engineering Chemistry Research*, 52(9):3354–3362. 91

[22] Smith, G. L., Schmidt, S. F., McGee, L. A., and Field, M. (1962). Application of statistical filter theory to the optimal estimation of position and velocity on board a circumlunar vehicle. *NASA*. 84

[23] Soize, C. and Le Fur, O. (1997). Modal identification of weakly non-linear multidimensional dynamical systems using a stochastic linearisation method with random coefficients. *Mechanical Systems and Signal Processing*, 11(1):37–49. 109

[24] Uhlmann, J. (1995). Dynamic Map Building and Localization: New Theoretical Foundations. 84

[25] Wan, E. A. and Van Der Merwe, R. (2000). The unscented Kalman filter for nonlinear estimation. *IEEE 2000 Adaptive Systems for Signal Processing, Communications, and Control Symposium, AS-SPCC 2000*, v:153–158. 88

[26] Wang, Z.-n. and Fang, T. (1986). A Time-Domain Method for Identifying Modal Parameters. *Journal of Applied Mechanics*, 53(1):28. 109

[27] Wu, Y., Hu, D., Wu, M., and Hu, X. (2005). Unscented Kalman Filtering for Additive Noise Case : Augmented versus Nonaugmented. 12(5):357–360. 91

5

Experimental study on a complex bolted structure

Contents

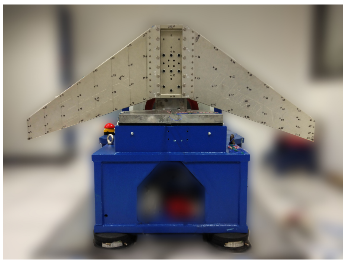

Summary During the CLIMA project several experimental campaigns were carried out on a set of different structures and mock-ups. This chapter will analyze the experimental data gathered on the AERO mock-up. It will be a way to test the post-processing tools based on Kalman filter described in the previous chapter and, at the same time, to evaluate the mock-up's nonlinear dynamic behavior and how it is influenced by parameters such as the type, the number and the tightening torque of the deployed bolts.

5.1 Experimental Setup

The main object of investigation of this work and of the CLIMA project in general is the AERO mock-up, described in section 1.5.2. Two different test campaigns were carried out on the mock-up, the first of which took place in the AIRBUS labs, while the second at the SOPEMEA company.

Every experiment, especially when dealing with nonlinearities, needs a proper and correct setup. A particular attention was paid to the pre-testing phase by applying some dedicated methods in order to choose support location, accelerometers placement, and excitation points. In the next section experimental setup choices will be justified and motivated by a careful pre-testing evaluation of the structure.

5.1.1 Pre-Testing

When a new structure arrives into a lab to be tested, it's not always easy to understand how it's going to behave dynamically and what is the best way to test it. This problem usually involves three main questions:

- How do I support the structure?
- Where do I excite the structure?
- Where do I put the sensors?

In order to avoid losing time on these matters, a procedure is developed to quickly find the answer to these questions. The ingredients needed for this analysis are the following:

- The structure finite element mesh;
- The numerical structure's natural frequencies;
- The numerical mass normalized mode shape matrix Φ;
- A condition on the number and/or type of modes to consider. A typical condition is to consider the M modes whose natural frequencies are lower than a maximum value ω_{max}.

These data are usually already available from the design phase, without generating any additional time losses.

5.1.1.1 Optimal Support

The first question to answer is: how do I support the structure? Regardless of the type of excitation, the test structure will always have to be supported or suspended in some way. However, the two possible configurations are *grounded* or *freely supported*. In the first case the structure is firmly fixed to the ground or to a supporting device, in order to simulate the real working conditions. In this case, the operating boundary conditions define the structure support, and this step can be skipped. In the second case the goal is to ideally arrive at free-free boundary conditions, which will be easier if the process explained in this section is followed.

Considering a selection of M modes, in [3] D. Ewins defines the **Average Driving Degree Of Freedom Displacement** as:

$$\mathrm{ADDOFD}(j) = \sum_{m}^{M} \frac{\phi_{mj}^2}{\omega_m^2} \tag{5.1}$$

which is an indicator of the modal average displacement of the j^{th} degree of freedom for the chosen mode range. The application of eq. 5.1 to all the degrees of freedom leads to a map describing the structure displacement. The most suitable region to support the structure is the one where the ADDOFD displacement is lower. An example of this procedure on the AERO mock-up can be observed in fig. 5.1. In this case the most suitable zone to support the structure is represented by the upper central part, characterized by a deeper blue color.

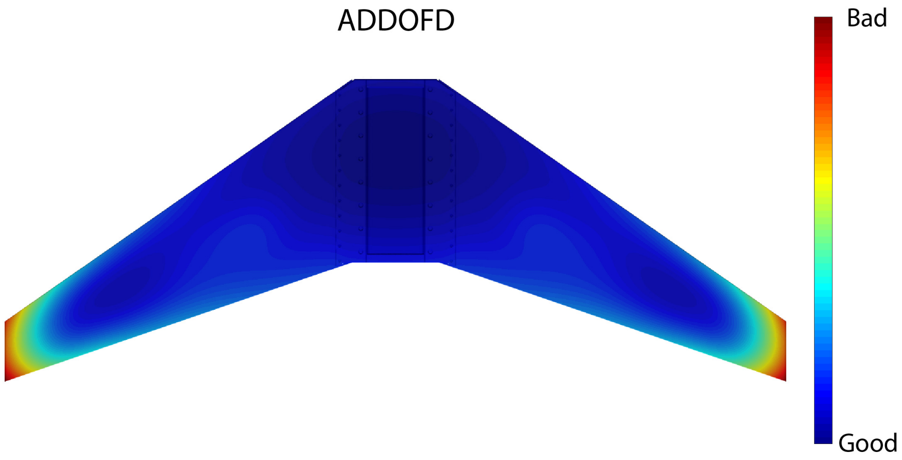

Figure 5.1 – Average Driving DOF Displacement map for the AERO mock-up

5.1.1.2 Optimal Driving Point

The second question concerns the optimal location for structure excitation. When considering an impact hammer excitation or a suspended shaker, the combination of two different parameters is helpful to decide where to place the excitation points:

1. **Optimal Driving Point ODP:** it's a parameter used to visualize the points of the structure which are more suitable as driving points. The ODP of a single degree of freedom j in the selected mode range can be calculated as:

$$\mathrm{ODP}(j) = \prod_{m}^{M} |\phi_{mj}| \tag{5.2}$$

   Its key feature is to visualize the nodes region of the modes under study. In fact, it's usually a bad idea to hit a structure in a point corresponding to a mode node, because in this way that mode won't be well excited. By calculating the ODP for every degree of freedom is possible to built a visual map to help you decide the driving points position. The ODP has been calculated on the AERO mock-up and the resulting map is shown in fig. 5.2.

2. **Average Driving Degree Of Freedom Velocity ADDOFV:** it's a parameter used to visualize the average node velocity and calculated as:

$$\mathrm{ADDOFV}(j) = \sum_{m}^{M} \frac{\phi_{mj}^2}{\omega_m} \tag{5.3}$$

   The main information provided by this parameter is the fact that areas with high velocity are more prone to double impact problems and a special attention has to be paid when hitting the structure in these areas. The ADDOFV has been calculated on the AERO mock-up and the result is shown in fig. 5.3.

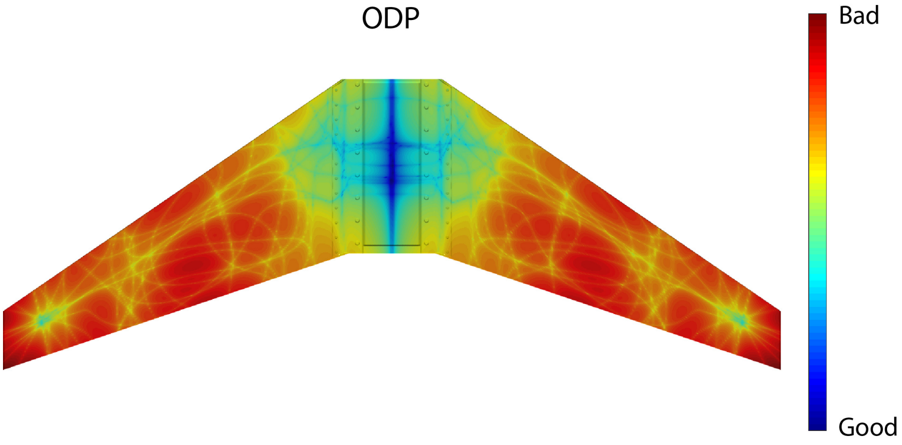

Figure 5.2 – Optimal Driving Point map for the AERO mock-up

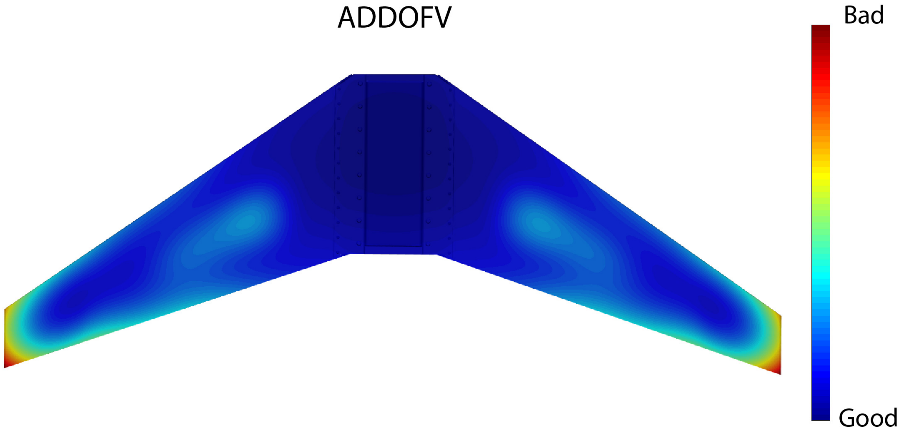

Figure 5.3 – Average Driving DOF Velocity map for the AERO mock-up

The combination of the two parameters outlined in this section gives a detailed insight of the structure from a driving point perspective. It's particularly interesting to observe the ODP and ADDOFV maps of figs. 5.2-5.3. On one hand, the ODP map shows the location of mode shapes' nodes as colored streams running on the wings, evaluating the degrees of freedom based on their value as driving point. On the other hand, the ADDOFV map warns us about the fact that the points close to the wings tips need to be treated with particular care, in order to perform acceptable impact tests.

5.1.1.3 Optimal Accelerometers Placement

The last question to answer concerns the optimal placement of sensors. Since the availability of accelerometers is usually limited, the optimization of their placement is essential in order to be able to clearly capture the interested modes. In the case of a simple modal analysis, this aspect can be by-passed by choosing a roving hammer approach over a roving accelerometer approach, as explained in section 2.3.1. However — when investigating nonlinear systems — it's important to have all the measurements at once, which makes the accelerometers placement an important task.

The approach used for the determination of an accelerometers placement capable of repre-

senting and distinguishing the mode shapes inside a certain frequency range is the Orthogonal Maximum Sequence (OMS) method developed by Balmes [1]. The method starts by defining the target modes that have to be captured. Next, a criteria is defined to select the best degree of freedom to put a sensor and a certain number of accelerometers are placed by reiterating this process.
An example of the application of this method can be observed in fig. 5.4, where 15 accelerometers are placed for the free-free conditions case. However, since the linear modal analysis is performed with the roving hammer approach and the sweep tests are going to be focused only on a few modes, the OMS have been used in this work as a complementary tool to define the experimental mesh and the accelerometers positions.

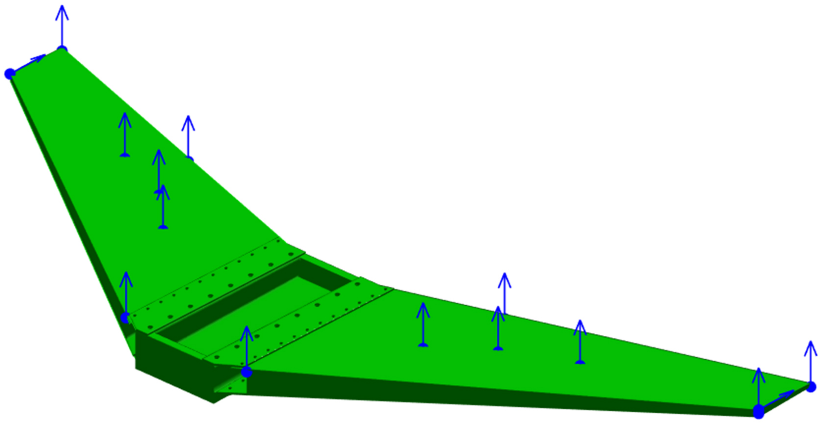

Figure 5.4 – Example of OMS method application on the AERO Mock-up.

5.1.2 Configurations and Objectives

The AERO mock-up has been object of different types of tests. At first, in order to understand what kind of structure we were dealing with, a linear modal analysis in free-free conditions was carried out. Secondly, the structure has been mounted on an electromagnetic shaker and its behavior was evaluated at higher levels of excitation in order to characterize its nonlinearities. Fig. 5.5a shows the AERO mock-up suspended by a combination of bungees and fish lines to reproduce free-free conditions. Let's note how the structure's support location has been chosen thanks to the ADDOFD parameters seen in section 5.1.1.1. Fig. 5.5b shows the AERO mock-up mounted on the shaker, with the excitation direction perpendicular to the wings.
Besides the different tests performed, different configurations of the mock-up have been tested, in particular on the shaker. As said in section 1.5.2, the AERO mock-up was developed to simulate real joints of real aerospace structures. In fact, except for the two rows of M10 bolts connecting the plate to the caisson, all the other bolts are close-tolerance titanium bolts and they are mounted according to existing norms. However, different configurations of these bolts have been tested, which are:

- **ABT**: All-Bolts-Titanium. This is the basic configuration, with all the close-tolerance titanium bolts mounted following the norm. Their tightening torque is set to the nominal torque of 7Nm.

- **HBT**: Half-Bolts-Titanium. It's the same as the ABT configuration, but with one bolt out of two. This configuration is tested to understand how the number of bolts influences the dynamic behavior. The tightening torque is again set to the nominal torque of 7Nm.

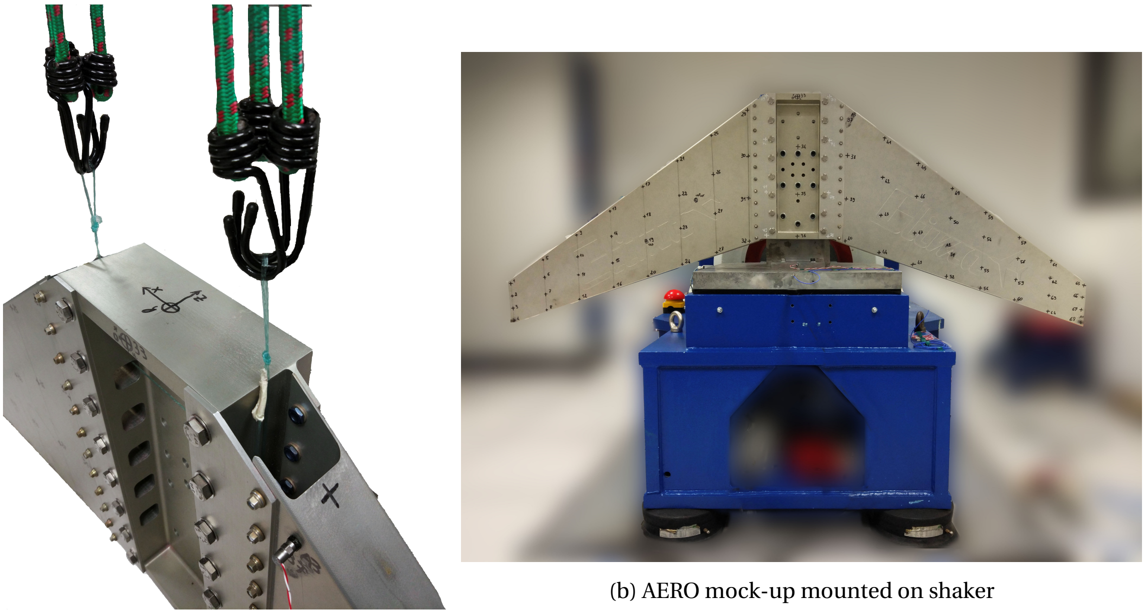
(a) AERO mock-up in free-free conditions

(b) AERO mock-up mounted on shaker

Figure 5.5 – AERO mock-up experimental boundary conditions

- **ABM**: All-Bolts-M6. Again, it's the same as the ABT configuration, but this time all the titanium bolts are replaced with standard M6 bolts. This configuration is tested to understand how the bolt-hole clearance and the different type of bolts influence the dynamic behavior. For this configuration the tightening torque is varied between three different values:
    - 8Nm: nominal tightening torque;
    - 6Nm: 75% of the nominal torque;
    - 3Nm: 37,5% of the nominal torque.

The abbreviations in bold will be used throughout this chapter to indicate the different configurations.

A linear modal analysis on the ABT configuration of the AERO mock-up suspended in free-free conditions and mounted on the shaker have been carried out. Then, an attempt of nonlinear modal analysis with the impact hammer have been performed and post-processed with the help of the Kalman filter. Then, an extensive experimental sweep sine testing campaign has been accomplished and post-processed on the different mock-up configurations. The results will be given in section 5.2.

The objectives of the different test campaigns performed on the AERO mock-up can be divided into two categories. On one hand, there is the aim to study the dynamic behavior of a *real* bolted structure and to understand how this is influenced by several parameters such as the number of bolts, the type of bolts, and their tightening torque. On the other hand, there is the need to validate the modeling tools and post-processing methods developed in this work for the CLIMA project.

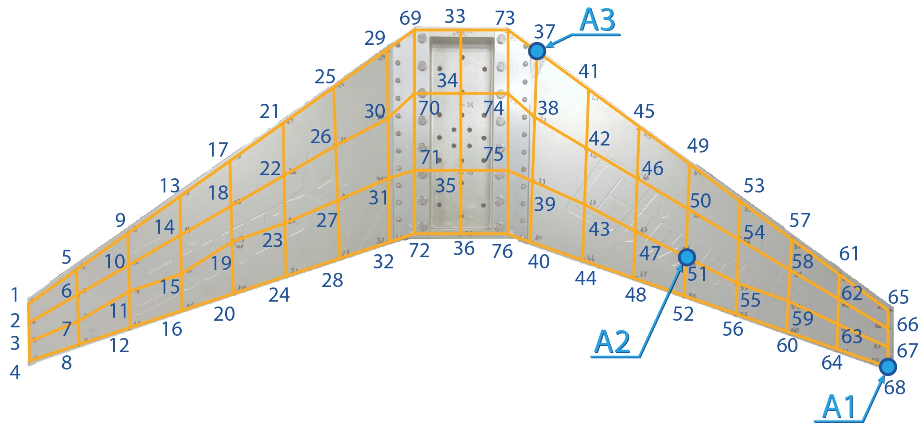

Figure 5.6 – Experimental mesh and accelerometers' position for impact testing modal identification.

5.2 Experimental Results

This section will give the results obtained from the experimental campaign on the AERO mock-up. In particular, impact hammer tests and sweep sine test will be the main post-processed data.

5.2.1 Impact Testing

The part of the experimental campaign dedicated to impact hammer tests is divided in two main parts:

1. Linear modal analysis: a classic analysis to build a linear model of the structure;
2. Nonlinear modal analysis: the application of the nonlinear Kalman filter tool seen in chapter 4 to evaluate the dynamic behavior at higher shock forces.

5.2.1.1 Linear Modal Analysis

The linear modal analysis has been carried out on the ABT configuration of the AERO mock-up for the free-free boundary conditions and when mounted on the shaker. The method used for the modal identification is the Line-Fit Method (see Appendix A), a SDOF identification method in the frequency domain first created by Dobson [2], and then further developed by Ewins [3] and [5]. With the help of the pre-testing process described in section 5.1.1, and considering that the roving hammer method is used, 76 points have been identified on the structure to constitute the experimental mesh. The latter can be observed in fig. 5.6. For the measurements, three accelerometers have been placed in strategic points — indicated by the dots in fig. 5.6 — in order to be able to compare the identified results.The structure was hit in each of the points defining the experimental mesh at a very low impact force, so that any possible nonlinearity wouldn't be excited.

The frequency range of interest is between 0 Hz and 400 Hz. Fig. 5.7 shows the CMIF (Complex Mode Indication Factor) relative to the AERO mock-up in free-free conditions. The CMIF is an indicator which takes into account all the frequency response functions gathered and returns a curve indicating where the modes are more likely to exist (for more information see Appendix A). A total of 15 modes are identified in the frequency range of interest, and their modal quantities obtained through the Line-Fit method are given in table 5.1. It can be noticed that the identified damping ratios are very small for all the modes — always smaller than 0.11% —

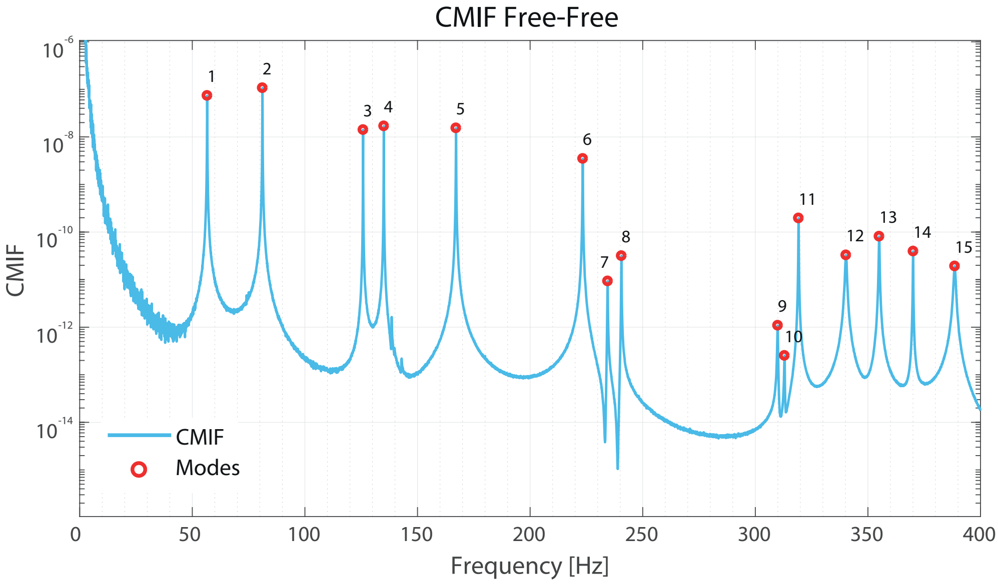

Figure 5.7 – Complex Mode Indicator Factor for the AERO mock-up in free-free conditions.

MODE ID	f_n [Hz]	ζ_n[%]	MODE ID	f_n [Hz]	ζ_n[%]
1	56.61	0.06	9	309.92	0.05
2	81.12	0.02	10	312.94	0.03
3	125.83	0.01	11	319.19	0.02
4	135.04	0.03	12	340.23	0.10
5	167.10	0.02	13	355.07	0.04
6	223.35	0.02	14	370.03	0.02
7	234.40	0.04	15	388.54	0.11
8	240.54	0.03			

Table 5.1 – Modal analysis results for the AERO mock-up in free-free conditions.

making of the AERO mock-up a very lightly damped structure. Finally, the mode shapes of the first six modes can be observed in fig. 5.8. The same analysis has been carried out on the same configuration of the AERO mock-up, but this time mounted on the shaker. Fig. 5.9a shows the CMIF for the case of the structure mounted on the shaker. In the same frequency range are now identified 12 modes, whose modal parameters are given in table 5.2. The calculated damping ratios are still small, but slightly larger than the free-free conditions case.

In this case, an additional complexity is noticed: the presence of double modes. In fact, due to the structure's boundary conditions and its symmetrical nature, each mode has its symmetric and anti-symmetric counterparts. In theory, the symmetric and anti-symmetric modes have the same natural frequency. However, due to small symmetry imperfections, these modes are not exactly at the same frequency, but they are slightly separated. This phenomenon can be observed in fig. 5.9b, in which is shown a detail of a frequency response function of the AERO mock-up mounted on the shaker. It's possible to see the symmetric and anti-symmetric part of the first flexion mode separated only by about 1Hz. The presence of double modes like these adds a degree of difficulty to the modal identification process.

The main aspects to be underlined and to be taken away are that the AERO mock-up is a very lightly damped structure in both boundary conditions cases, and that there are close double modes in the case the structure is mounted on the shaker. Furthermore, at the very low ex-

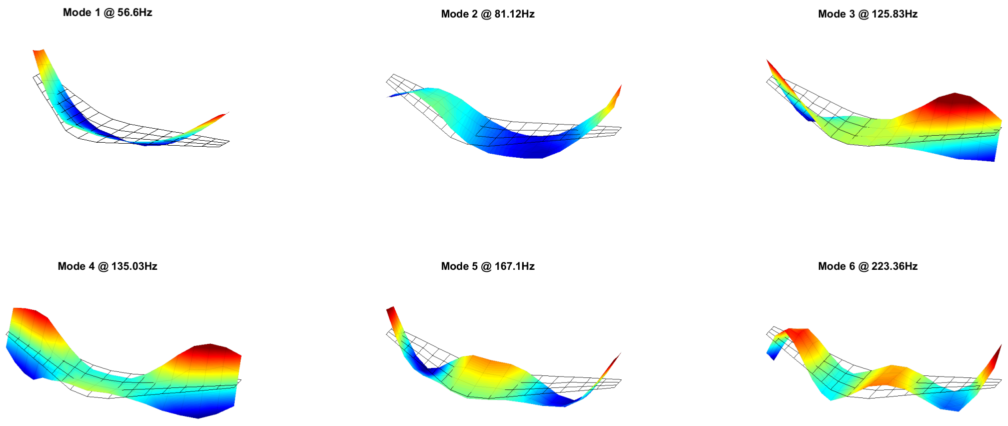

Figure 5.8 – First six mode shapes for the AERO mock-up in free-free conditions.

MODE ID	f_n [Hz]	ζ_n[%]	MODE ID	f_n [Hz]	ζ_n[%]
1	33.77	0.16	7	234.12	1.41
2	34.55	0.04	8	266.69	0.73
3	125.51	0.20	9	308.87	0.60
4	127.83	0.02	10	327.27	0.12
5	135.33	1.07	11	334.32	0.11
6	146.56	0.42	12	342.19	0.42

Table 5.2 – Modal analysis results for AERO mock-up mounted on the shaker.

citation levels provided by the impact hammer for the linear modal identification, no signs of nonlinearity were detected in the calculated FRFs.
The linear modal analysis is therefore completed.

5.2.1.2 Nonlinear Modal Analysis

In the previous section we obtained the linear modal parameters of the AERO mock-up. The goal now is to see if it's possible to spot a nonlinear behavior by exciting the structure through high forces impacts. If this is the case, the nonlinearity will be evaluated with the help of the Kalman filter method for impact tests built in section 4.2.
The impact point is set to be the point 19 on the experimental mesh, which was chosen by considering both the ODP and ADDOFV parameters, seen in section 5.1.1.2. The considered measures are the one gathered by accelerometers A1 and A2 indicated in fig. 5.6. Several shocks at different impact forces have been carried out. At this point we have to open a small parenthesis to talk about the application of the Kalman filter method on real experimental measurements, which are usually characterized by a high modal density. In fact, considering the AERO mock-up, during the linear modal analysis it was possible to see that, in the considered frequency range (0-400Hz), there are 15 modes. Taking into account the complexity of the different covariances initialization, extensively discussed in chapter 4, it would be very difficult to follow the nonlinear evolution of all the modes. Therefore we will here consider only the first two modes. To do this, two initialization approaches can be followed:

1. Include all the other modes contributions in the measurement covariance R. However, in the developed method, R is assumed to be constant, while in reality, considering the decaying nature of time histories, it varies in time. Therefore, without an additional mod-

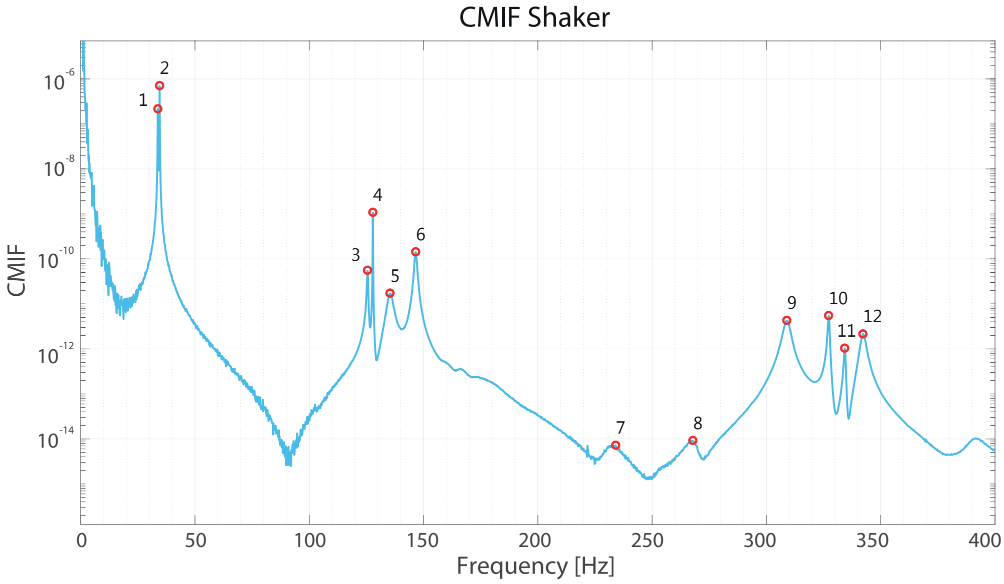

(a) Complex Mode Indicator Factor for the AERO mock-up mounted on the shaker.

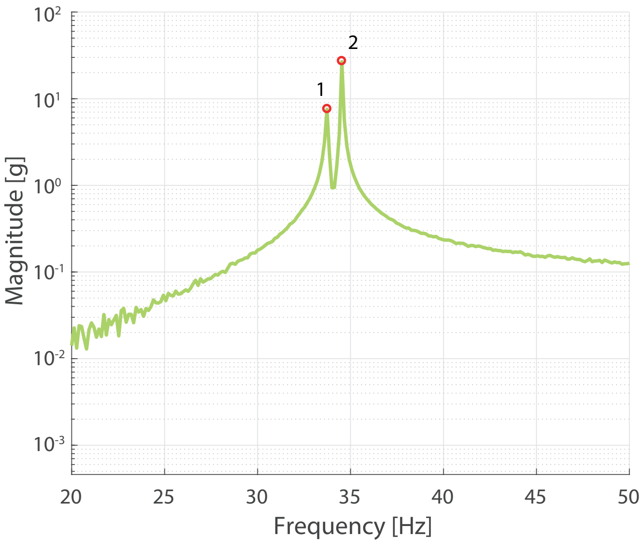

(b) Particular of the first double mode of an impact FRF.

Figure 5.9 – Linear modal analysis of the AERO mock-up mounted on the shaker.

eling of the evolution of measurements' covariance R in time, this method will fail.

2. Filter the time signal to remove the contributions of the modes we don't want to track. In this way, the assumption of a constant covariance R will be respected.

The approach used here is the second one. A low-pass filter is applied to the time signal in order to have the contributions of the first two modes only. The original FRF and the filtered one for the AERO mock-up are shown in fig. 5.10, for an impact peak force of 800N.

At this point, the Kalman filter method is applied on the filtered signal. For this, two accelerometers' measurements are taken into account and two modes are tracked. The state vector length is therefore $L = 12$.

Fig. 5.11 shows the tracking of the accelerometer A1 (see fig. 5.6) time history and the identified

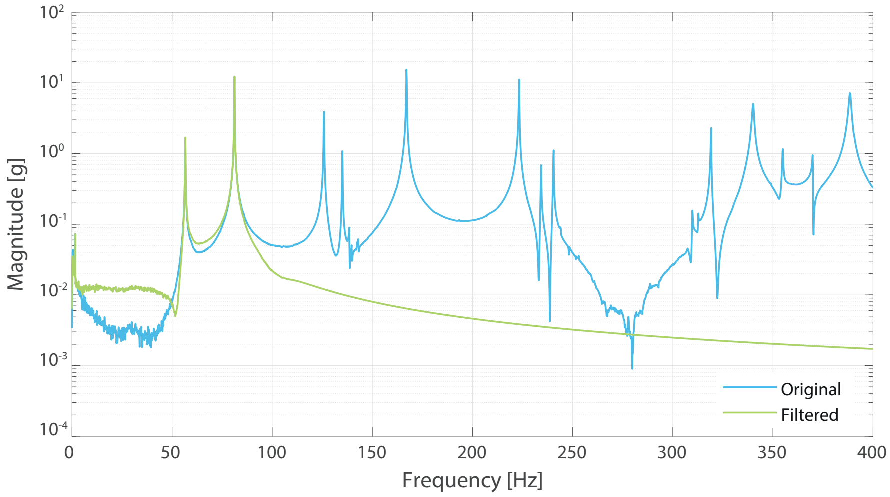

Figure 5.10 – Original FRF and the low-pass filtered one

modes contributions for an impact peak force of 800N. The method is able to track the single modes contributions and their amplitudes.

More interesting, fig. 5.12 shows the tracking of natural frequencies and damping ratios as a function of time. As we already noticed in section 4.2.2 for the application of the method on

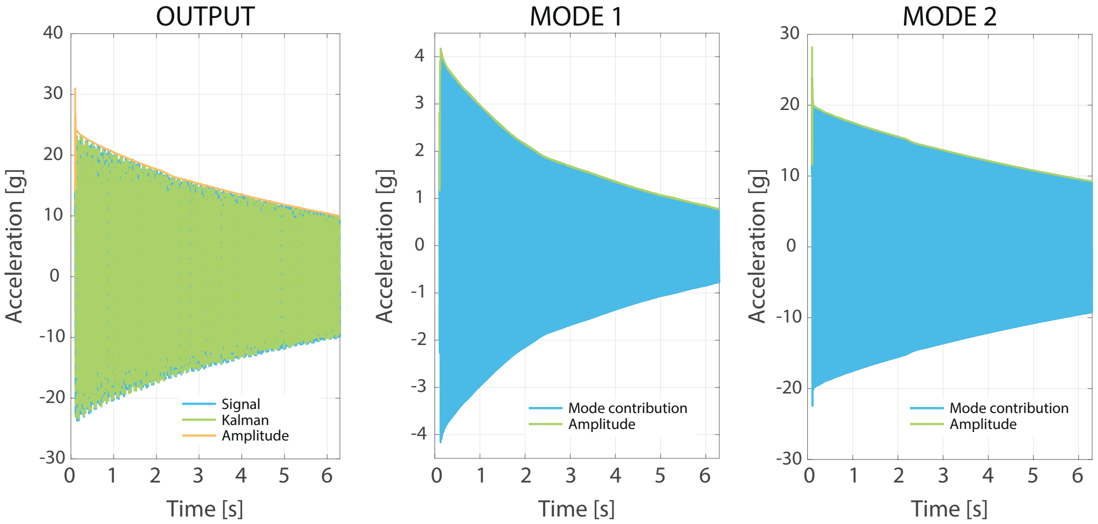

Figure 5.11 – Total signal and modes contributions tracking for accelerometer A1 for a test at 800N impact force.

the test case, at the very beginning of the tracking there is a quick transient phase, needed for the algorithm in order to converge to the solution.

If we remove the transient part and we plot the tracked natural frequencies and damping ratios as functions of the instantaneous tracked amplitude, it's possible to visualize their nonlinear behaviors. Fig. 5.13 shows the nonlinear behavior of the two modes a a function of the amplitude at point 1: the blue lines represent the raw results coming from the Kalman filter, while the red lines are cubic spline interpolations of the raw results. Let's start by looking at the results for the second mode in fig. 5.13b. Concerning the frequency, a slight softening behavior can be appreciated, while the damping becomes somewhat larger with amplitude. However, if we

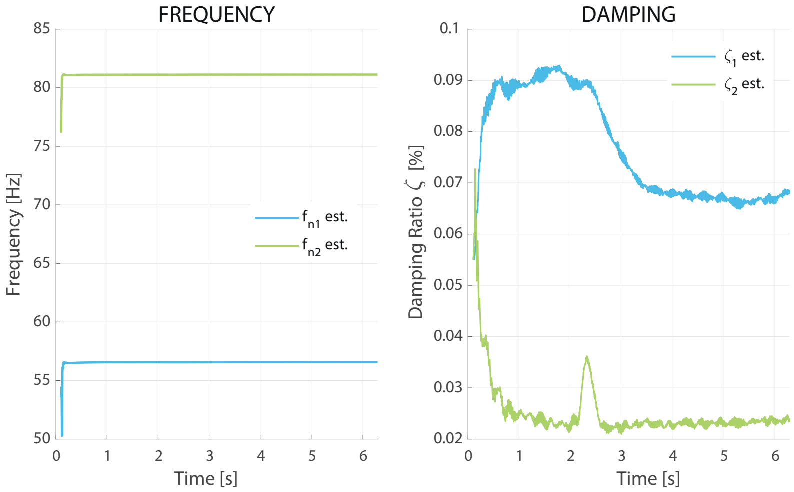

Figure 5.12 – Tracking of natural frequencies and damping ratios in time for a test at 800N impact force.

take a look at the the entity of the variations in frequency and damping, the level of nonlinearity is almost non-existent. It's also important to notice that the damping at low amplitude corresponds to the linear damping calculated by the linear modal analysis and given in table 5.1 as $\zeta_1 = 0.02$. From these results we could say that the impact hammer excitation is not enough powerful to *awaken* the nonlinearity.

Analogous considerations can be made by observing the results for the first mode in fig. 5.13a. Here the shift in frequency is again very small, and it shows a slight softening behavior. However, the shift is so small that it's difficult to talk about a real nonlinearity. Observing the damping, in this case the trend is not as clear as the one of the second mode, but it's important again to notice that the low amplitude damping reaches the *linear* damping given in table 5.1 as $\zeta_1 = 0.06$.

Taking into account the very small damping values, it can be said that the Kalman filter method performs well and its accuracy is remarkable. However, from the analyzed results, it looks like the nonlinearity of the system is only slightly or not at all excited. In fact, the main takeaway of these results is that the hammer impact excitation is not sufficient to interest the structure nonlinearities, and a more powerful excitation method has to be chosen. In the next section the AERO mock-up will be positioned on the shaker and the results, obtained with the adequate Kalman filter post-processing method, will be described.

5.2.2 Sweep Sine Testing

In order to excite the structure nonlinearities, the AERO mock-up has been mounted on the electromagnetic shaker for a sweep sine testing campaign.

In the linear modal analysis performed in section 5.2.1.1 it was noticed the presence of *double modes*, especially in the low frequency range. However, using the impact hammer, all the modes in the chosen frequency range were well excited. This is not the case with the electromagnetic shaker. Fig. 5.14 shows the FRF obtained from a random excitation with a PSD of amplitude 0.2 g in the 0-400 Hz frequency range. It's possible to see that only a few modes are truly excited. In fact, due to the symmetric nature of structure and excitation, only the flexion modes are interested.The modes on which we will focus throughout this section are shown in fig. 5.14 and they are named as it follows:

- **Mode 1a**: the anti-symmetric part of the first double mode, nominally at 33.7 Hz

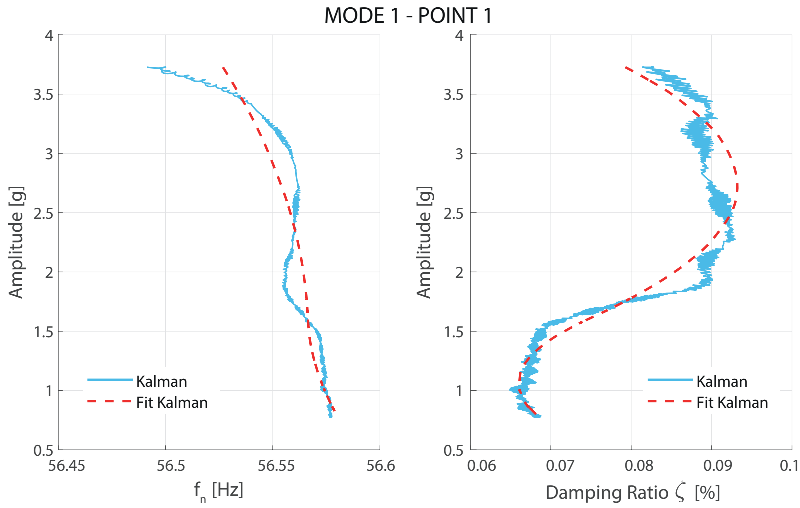

(a) Mode 1

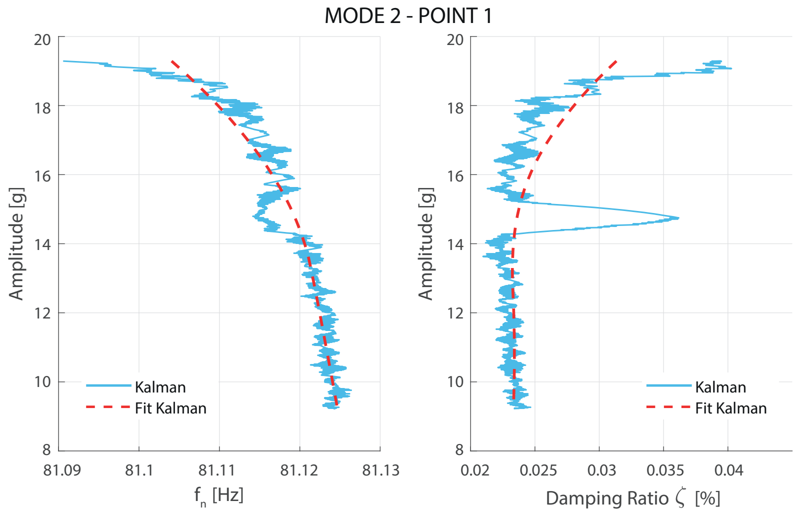

(b) Mode 2

Figure 5.13 – Nonlinear natural frequencies and damping as a function of amplitude for the accelerometer A1.

- **Mode 1b**: the symmetric part of the first double mode , nominally at 34.5 Hz;
- **Mode 2b**: the symmetric part of the second flexion double mode, nominally at 146.5 Hz.

These chosen modes are the ones that are more excited by the shaker. In fact, taking for example the first pair of torsion double modes, linearly identified as 125.5 Hz and 127.8 Hz the anti-symmetric and symmetric parts respectively, it's possible to see that their contribution during shaker excitation is very low.

At this point a series of sweep sine tests at different amplitude levels are carried out on the ABT configuration of the AERO mock-up. The experimental results are post-processed with the method developed in section 4.3, which is a combination of the Unscented Kalman Filter (UKF) and the FORCEVIB method. In fig. 5.15 is shown an example of UKF application for an upward sweep sine test around the first double mode for a forcing amplitude of 0.1 g. The left and center figures show the input and output signals tracking: the blue lines represent the experimental data, while the green and orange lines represent respectively the signal reconstructed

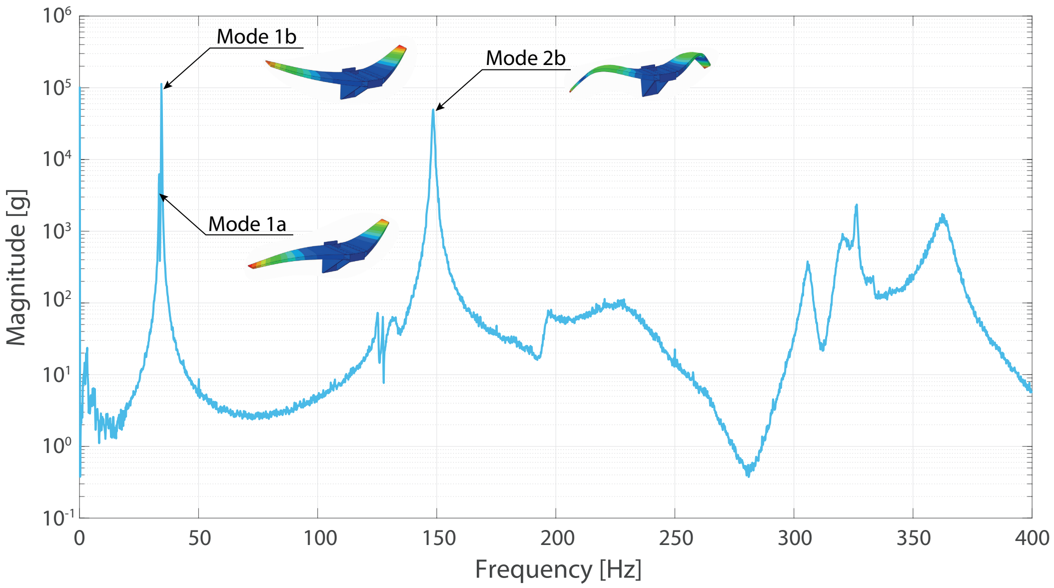

Figure 5.14 – FRF for a random excitation on the shaker in the frequency range 0-400Hz.

by the UKF and its amplitude. It's important to see how the Kalman filter manages to remove the signal noise, which in this case is particularly relevant for the input signal. The right figure, instead, shows the input and output instantaneous frequencies tracking. Since it's an upward sweep sine test, the frequency lines have a positive slope, while for a downward sweep the slope would have been negative.

After having analyzed the experimental results for different forcing amplitudes, the *Kalman FRFs* can be calculated as explained in section 4.3.2.3. These are gathered in fig. 5.16: the upper figures represent the FRFs for modes 1a and 1b, while the lower ones are relative to mode 2b. In addition, the figures on the left represent the results for upward sweeps, while figures on the right represent the results for downward sweeps. It's possible to notice the typical behavior of bolted structures that we have seen in section 2.1.4, ie a progressive reduction of the response amplification with a growing excitation amplitude. It's also possible to see how well the phase is tracked by the Kalman filter. Therefore, the shaker excitation, differently from the impact hammer, conveys enough energy to clearly visualize the structure nonlinearity.

However, until now we have just described the post-processing part relative to the Kalman filter, with which we can qualitatively see the nonlinear nature of the considered modes. The other part consists in quantifying the nonlinearity through the FORCEVIB method. For each mode, the sweep sine tests at different amplitudes and directions have been post-processed to find the nonlinear behavior of natural frequency and damping as a function of displacement amplitude. The results are shown in fig. 5.17: the orange lines represent the results of the nonlinear identification for the upward sweeps at each forcing amplitude, while the yellow lines are relative to downward sweeps. In addition, a four-parameter Iwan model [6], represented by a dark green line, has been semi-automatically fitted to the results. The word “semi-automatically” means that the initial fit is performed automatically, while a manual fine-tuning of the parameters is requested to the user. In fact, as pointed out by Lacayo et al. [4], it's impossible to correctly fit the nonlinear natural frequency **and** damping of a real bolted structure at the same time. Therefore, a trade-off has to be found. In addition the green areas around the Iwan fits represent the Root Mean Square Error (RMSE) of the fit.

From the results it can be pointed out that the nonlinear behavior is well identified for all the considered modes, except for mode 1a damping, for which a trend is visible but the uncer-

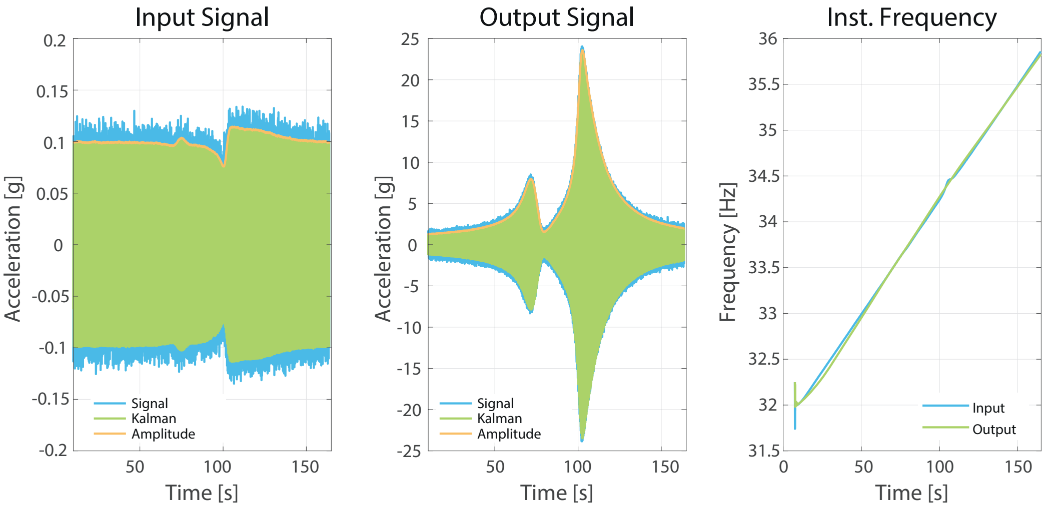

Figure 5.15 – Example of signal and instantaneous frequency tracking for an upward sweep of 0.05g excitation amplitude.

tainty level is a problem. The latter is probably due to the proximity of the anti-symmetrical and symmetrical part of the first double mode and to the fact that the contribution of mode 1a is lower than the one of mode 1b. In general, the nonlinear natural frequency is better identified than the damping, as it's usually the case in nonlinear modal identification. However, considering the low damping values, the accuracy is still acceptable. It's also possible to notice that it's essential to have the results from several forcing amplitudes tests in order to recognize a nonlinear trend.

The results shown until now were concerning the ABT configuration of the AERO mock-up. The process can be repeated for the other configurations in order to compare them. Fig. 5.18 shows a series of comparisons between the four-parameter Iwan models fitted to the different configurations:

- Fig. 5.18a shows the comparison between the three configurations — ABT, HBT and ABM (see section 5.1.2) — at nominal torque. Concerning the natural frequency, the HBT shows a lower natural frequency, which is logical, considering it has half of the bolts of the other configurations. Regarding the damping, there are no big differences between the three configurations, but again the HBT looks slighlty more damped.

- Fig. 5.18b shows the comparison for the ABM configuration at three different values of the tightening torque. The configuration with the lowest tightening torque shows a lower natural frequency and an higher damping than the others.

- Finally, fig. 5.18c shows the results for the same exact configuration — ABT at nominal torque — but from two different test campaigns in two different testing facilities — Airbus and Sopemea. The damping behavior is very similar while the natural frequency is lower for the test campaign at the Sopemea. This results is easily justifiable by the fact that a different number of accelerometers were used (4 at Airbus, 22 at Sopemea), with the subsequent amount of cables, increasing in this way the structure total mass, and therefore lowering the natural frequency.

It can be noticed that, in these comparisons, the amplitude range is not always the same for all the configurations. This is due to the fact that sometimes the experimental data were not available, due to the inability of passing through the resonance without a failure of the shaker

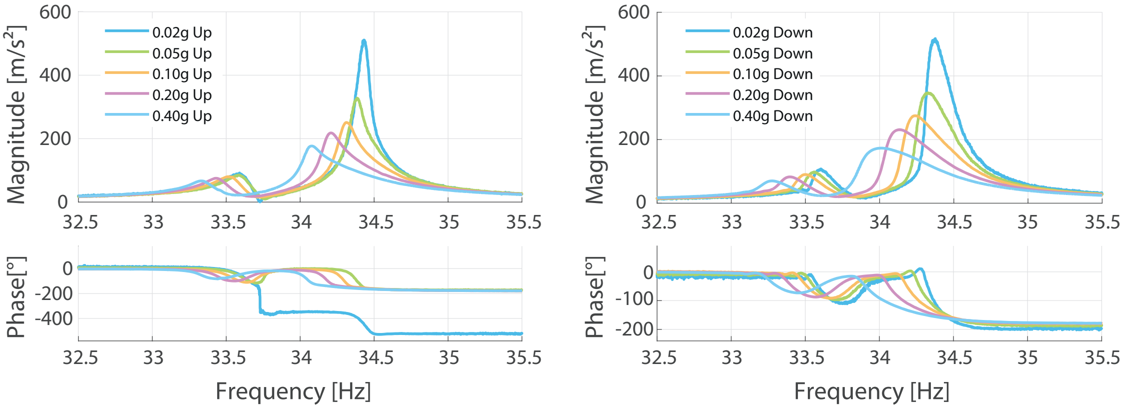

(a) Modes 1a and 1b. Upward sweep

(b) Modes 1a and 1b. Downward sweep

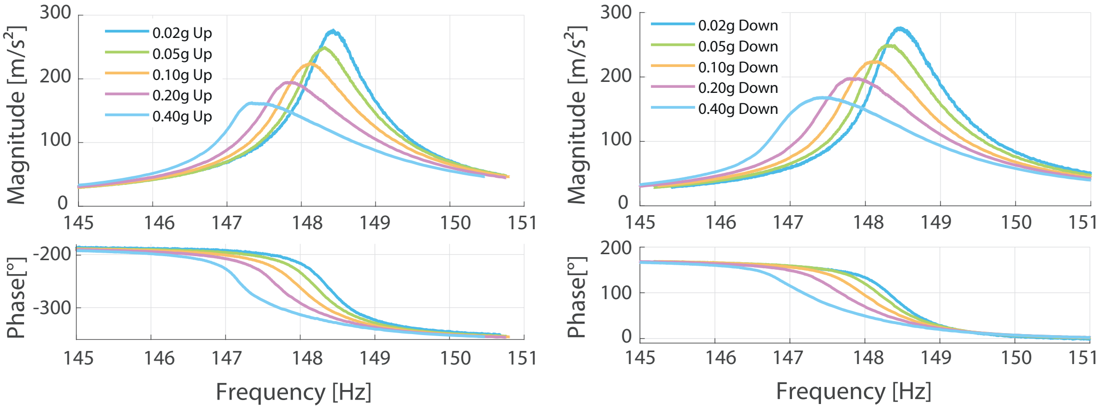

(c) Mode 2a. Upward sweep

(d) Mode 2a. Downward sweep

Figure 5.16 – Comparison of FRFs obtained with the UKF at different forcing amplitudes, for upward and downward sweeps on the ABT configuration.

control loop.

From these results it's possible to say that the developed nonlinear modal analysis tool for sweep sine tests is reliable and can be an alternative solution to the current post-processing methods. However, with regard to technological solutions to increase damping in bolted structures, it was shown that the type of used bolts (close-tolerance titanium or standard M6) didn't influence the amount of damping provided, which was instead the case when the number of bolts was reduced by half. However, removing bolts in a real world doesn't look like a robust solution. The same applies when talking about the bolts' tightening torque. Results show that a lower torque brings a larger damping, but it's not an applicable solution in the aeronautical world, where bolts are subjected to strict mounting norms and directives. Nevertheless, a possible solution can be to have a certain number of *structural* bolts and a certain number of *dissipative* bolts, with the task of increasing damping through friction. However, an utilization like this one would need a deeper understanding of the phenomenon and an extensive additional experimental study to evaluate which is the best way to implement it.

5.3 Conclusion

In this chapter was shown how the post-processing tools based on Kalman filter — with the exception of the formulation for random vibration testing — can be applied to real experimental

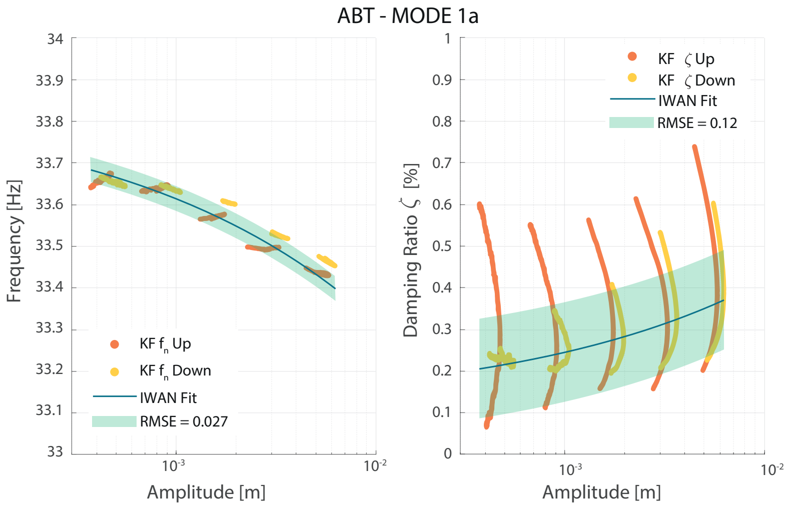

(a) Mode 1a.

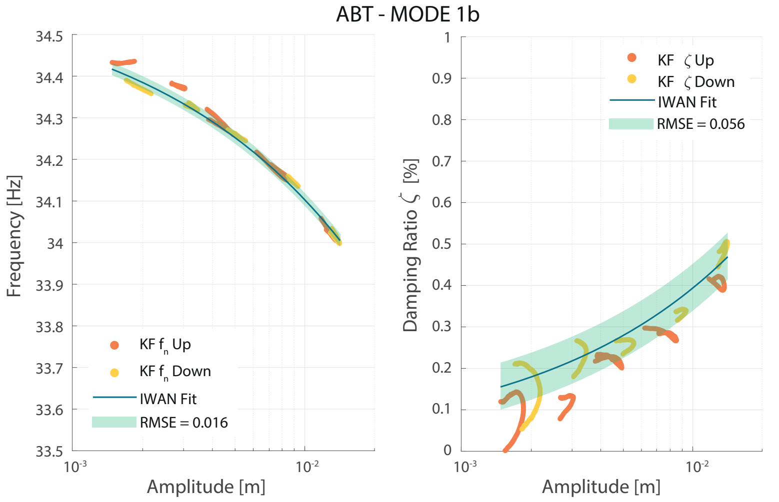

(b) Mode 1b.

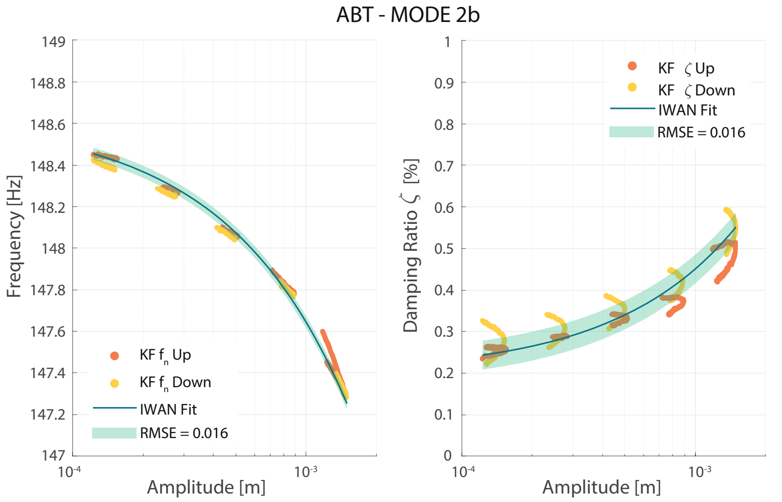

(c) Mode 2b.

Figure 5.17 – Nonlinear modal identification on the ABT configuration of the AERO mock-up, through the combination of Kalman filter and FORCEVIB method, fitted with four-parameter Iwan models.

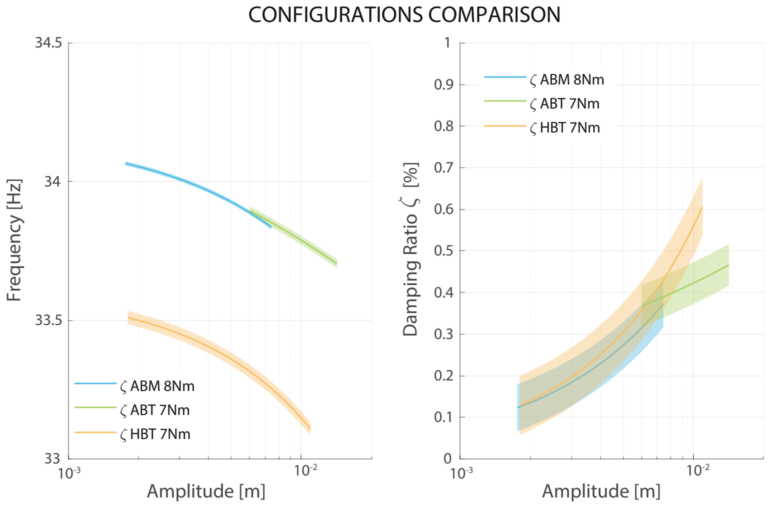

(a) Comparison between ABT, HBT, and ABM configurations. Mode 1b.

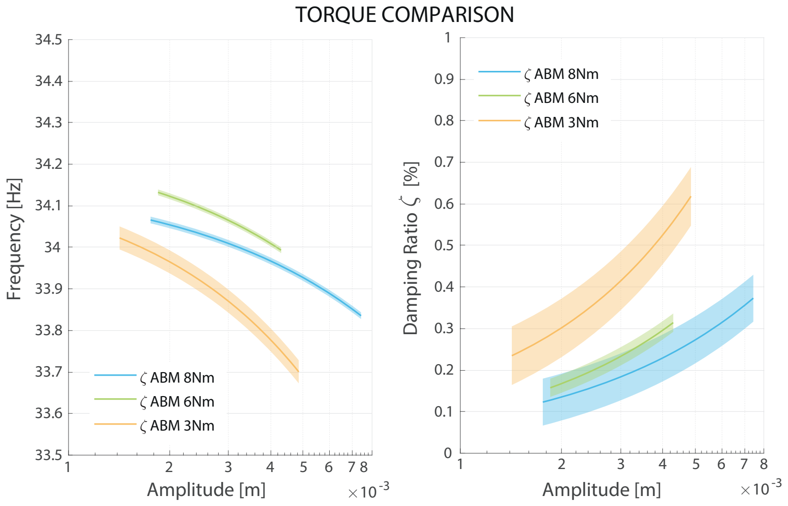

(b) Configuration ABM, different tightening torque levels. Mode 1b.

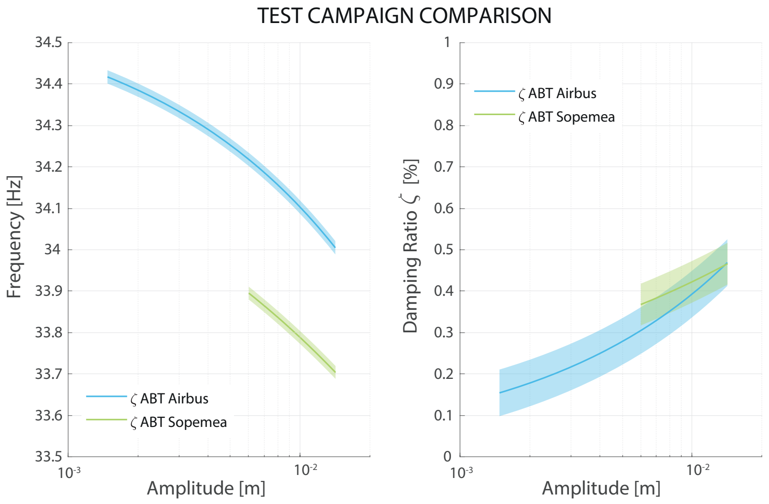

(c) Configuration ABT, different experimental campaign. Mode 1b.

Figure 5.18 – Nonlinear behavior comparison based on configuration, tightening torque, and experimental campaign.

data deriving from a real structure. Results have shown that the developed methods are able to evaluate the nonlinear evolution of natural frequency and damping with an acceptable precision, especially considering how lightly damped is the AERO mock-up.

That said, it's time to point out the limitations carried by the Kalman filter post-processing tools. Regarding the method for impact tests, the main limitation is, without any doubt, the difficulty of characterizing many modes at the same time, due to the growing complexity of parameters initialization. In fact, each mode adds $2N+2$ variables in the state vector — where N is the number of sensors considered — which not only adds complexity to the initialization task, but it also makes computation times longer. In the author's experience, when the number of modes to characterize becomes larger than three, the time spent in the initialization task can become very large and mode coupling can lead to faulty results. In addition, it's always advisable to have at least two measure points in order for the method to be more robust. This is valid as a general rule for all the Kalman filter based tools developed in this work.

Turning to the sweep sine tests, the main method's limitation, compared to the most used time-domain methods such as the Hilbert Transform, is its longer computation time. However, the author believes that a deeper code optimization process can lead to significant improvements. Also, the parameter initialization task is easier and more automated than for impact tests. In addition to the computation time, another possible limitation is the time needed for the actual experimental campaign. In fact, the structure under examination has to be tested at several forcing amplitudes, for upward and downward sweeps, in order to have a full characterization of the nonlinearity. Furthermore, it could be trivial to say, but the time measurements have to be continuous, ie without the interruptions that sometimes can take place in correspondence of a resonance, due to failures in shaker input control.

When a proper test campaign is performed, the method for sweep sine tests is capable of correctly evaluating a structure's nonlinear dynamic behavior, as previously shown. In the results the typical behavior of jointed structures has been observed and characterized.

The AERO mock-up chosen for the CLIMA project is a very lightly damped structure, and the characterized modes have shown a low but non-negligible level of nonlinearity, due to friction taking place at the contact interface. In particular, the level of accuracy in the determination of such small values of damping is remarkable.

Bibliography

[1] Balmes, E. (2005). Orthogonal Maximum Sequence Sensor Placements Algorithms for modal tests , expansion and visibility. *International Modal Analysis Conference.* 121

[2] Dobson, B. J. (1987). A straight-line technique for extracting modal properties from frequency response data. *Mechanical Systems and Signal Processing*, 1(1):29–40. 123

[3] Ewins, D. (2000). *Modal testing: Theory, practice, and application.* 118, 123

[4] Lacayo, R., Pesaresi, L., Groß, J., Fochler, D., Armand, J., Salles, L., Schwingshackl, C., Allen, M., and Brake, M. (2019). Nonlinear modeling of structures with bolted joints: A comparison of two approaches based on a time-domain and frequency-domain solver. *Mechanical Systems and Signal Processing*, 114:413–438. 130

[5] Maia, N. M. and Silva, J. M. (2001). Modal analysis identification techniques. *Philosophical Transactions of the Royal Society A: Mathematical, Physical and Engineering Sciences*, 359(1778):29–40. 123

[6] Segalman, D. J. (2001). An Initial Overview of Iwan Modeling for Mechanical Joints Acknowledgments. *Control*, (March):3–8. 130

Conclusion

The research works carried out in this thesis have covered the modeling and evaluation of the damping contribution of bolted in assembled structures.

At first, the author has tried to clearly outline the typical static and dynamic behavior of bolted structures, with the help of customized illustrations, mixed with numerical and experimental tests performed on real simple structures. This part was very important to understand complexities and challenges to which we are faced when dealing with bolted structures.

Secondly, a tool for the modeling of bolted joints that takes into account the friction at the contact interface was proposed and tested in real case. The tool consisted in a finite element connectors' system with nonlinear contact laws implemented inside of it. The goal was to be able to model bolted joints nonlinear behavior only by using the physical dimensions and data relative to the contacting surfaces. Results of the application of this tool on a real structure, demonstrated that the adopted approach cannot reproduce the detailed contact pressure distribution visible at bolted joints' interfaces. A different approach may be used in order to be able to actually predict the nonlinear behavior. However, the connector system was tested on a case in which the bolt tightening torque was chosen very low on purpose, in order to maximize the damping. In cases where the contact pressure distribution around the bolted joints interfaces doesn't vary considerably, the developed finite element system is able to reproduce the behavior of a real structure. Furthermore, it's a tool that can be efficiently used to model linear bolted structures.

Next, a post-processing nonlinear modal identification set of tools has been developed in order to be able to analyze experimental data from the most common types of tests. The common feature of the different tools is that they all use the Kalman Filter, a powerful mathematical instrument currently applied in many different fields. The theory of the methods is developed and tested on a simple nonlinear numerical system. The methods are able to identify the nonlinear evolution of natural frequencies and damping in the case of impact, sweep sine, and random vibration testing. However, the main drawback is the initialization of the filter parameters, which is not always simple, and it can sometimes lead to erroneous results. The use of Kalman Filter allows for a higher degree of accuracy in the determination of the modal quantities, especially considering the low damping values of the structure on which the method has been applied.

Finally, the set of tools based on Kalman Filter were tested on a real and complex structure, built specifically for the project. The methods for impact and sweep sine tests have been proved to be efficient and performing, while the one for random tests has not been implemented and therefore not tried out. The application on real experimental data has confirmed the advantages and imitations of the Kalman filter algorithm. The results showed the ability of the developed methods to follow the nonlinearities that are typical of bolted structures. However, the methods can be applied more in general to all nonlinear systems.

This work's main contribution was to explore and extend the existing knowledge about the dynamics of assemblies, first by creating a tool to help engineers to design bolted joints, and then to actually be able to evaluate with precision the nonlinear dynamic properties of structures in the testing phase. The future works linked to this thesis will have to address the different problems came out from the modeling and evaluation phases. Starting by the modeling, the future development will definitely have to be about finding the way of correctly describing the contact pressure distributions at bolted joints' interfaces, keeping at the same time a reasonable amount of ease of use for the final user. Concerning the evaluation, the future efforts will have to be turned to the automation of Kalman parameters' initialization, a crucial aspect which by itself it's a topic that could produce several PhD thesis. However, the latter it's an essential task to make the Kalman Filter a universal tool, that can be used not only by *Kalman experts*, but by a wider range of users.

A

Line-Fit Method

In chapter 5, when a linear modal analysis of the AERO mock-up is provided, it is mentioned that the latter has been carried out with the Line-Fit method. The appendix is intended to describe this linear SDOF modal identification technique, its nonlinear extension, and the toolbox created for the CLIMA project. The method was first developed by [1], and is referred to as the Bendent method by Maia and Silva [2]. The latter also defines the Line-Fit as the most powerful SDOF modal identification method.

A.1 Method Description

First of all, it's important to define the method's assumptions. Since it's a SDOF analysis method, the main assumption is that, in the vicinity of a mode, the system response is dominated by the single mode. Furthermore, the contribution of all the other modes can be expressed by a term independent of the frequency. The receptance of a linear system around its r^{th} natural frequency ω_r can therefore be written as:

$$\alpha_{jk}(\omega)_{\omega\approx\omega_r} = \frac{\mathrm{A}_{r_{jk}}}{\omega_r^2 - \omega^2 + j\eta_r\omega_r} + \mathrm{B}_{r_{jk}} \tag{A.1}$$

where η_r is the damping coefficient, $\mathrm{B}_{r_{jk}}$ is the residual term, which is the contribution of all the other modes to the system response in the vicinity of the r_{th} mode, and $\mathrm{A}_{r_{jk}}$ is the complex modal constant:

$$\mathrm{A}_{r_{jk}} = a_r + j b_r \tag{A.2}$$

where a_r and b_r are respectively its real and imaginary coefficients.
At this point it's possible to define the term $\alpha'_{jk}(\omega)$, which is the difference between the actual receptance and the value of the receptance at certain frequency Ω, defined as a *fixing* frequency. The $\alpha'_{jk}(\omega)$ can therefore be written as:

$$\alpha'_{jk}(\omega) = \alpha_{jk}(\omega_r) - \alpha_{jk}(\Omega) \tag{A.3}$$

Now, the following inverse FRF function $\Delta(\omega)$ is defined:

$$\Delta(\omega) = \frac{\omega^2 - \Omega^2}{\alpha'_{jk}(j\omega)} = \mathrm{Re}(\Delta) + j\,\mathrm{Im}(\Delta) \tag{A.4}$$

The real and imaginary parts of the Δ function can be expressed as functions of the frequency ω as:

$$\mathrm{Re}(\Delta) = m_\mathrm{R}\omega^2 + c_\mathrm{R} \quad ; \quad \mathrm{Im}(\Delta) = m_\mathrm{I}\omega^2 + c_\mathrm{I} \tag{A.5}$$

With this in mind, it's possible to perform the first part of the modal analysis for the chosen r^{th} mode. A frequency range around the receptance peak is considered, and the Δ function is calculated for each *fixing* frequency in the frequency range. The real and imaginary parts of the calculated Δ function are plotted as a function of the ω^2.
Then, the slope coefficients m_R and m_I of eq. A.5 are obtained and again plotted against the squared frequency ω^2. Now, it's possible to write the slope coefficients m_R and m_I as a function of ω^2 in the following way:

$$m_\mathrm{R} = n_\mathrm{R}\Omega^2 + d_\mathrm{R} \quad ; \quad m_\mathrm{I} = n_\mathrm{I}\Omega^2 + d_\mathrm{I} \tag{A.6}$$

where the different coefficients can be expressed as function of the researched modal quantities as:

$$n_\mathrm{R} = a_r \quad ; \quad n_\mathrm{I} = b_r \tag{A.7}$$

$$d_\mathrm{R} = -a_r\omega_r^2 - b_r\omega^2\eta_r \quad ; \quad d_\mathrm{I} = -a_r\omega^2\eta_r + b_r\omega_r^2 \tag{A.8}$$

Next, the coefficients p and q are defined as:

$$p = \frac{n_\mathrm{I}}{n_\mathrm{R}} \quad ; \quad q = \frac{d_\mathrm{I}}{d_\mathrm{R}} \tag{A.9}$$

Therefore, if the coefficients n_R, d_R, n_I and d_I are obtained by line-fitting the m_r and m_i data plotted against ω^2, the modal quantities can be calculated with the following equations:

$$\eta_r = \frac{q-p}{1+pq} \tag{A.10}$$

$$\omega_r^2 = \frac{d_\mathrm{R}}{n_\mathrm{R}(p\eta_r - 1)} \tag{A.11}$$

$$a_r = \frac{\omega_r^2(p\eta_r - 1)}{d_\mathrm{R}(1+p^2)} \quad ; \quad b_r = -pa_r \tag{A.12}$$

The whole process is shown in fig. A.1, applied on a linear system composed of three masses. The two top plots show the real and imaginary part of Δ, for the different values of *fixing* frequency in the chosen range spanning the receptance peak. It's possible to see that, for a linear system, the real and imaginary parts of the Δ function are represented by a series of lines, when plotted against the squared frequency f^2. The slope coefficients m_R and m_I are then calculated and shown in the bottom graphs as green circles. Considering eq. A.6, the m_r and m_i values are interpolated in order to find the coefficients n_R, d_R, n_I, d_I. At this point modal quantities can be calculated and they are shown in the bottom-right table. Finally, the receptance is reconstructed in the chosen frequency range with the identified modal parameter and compared to the original one in the top-right plot. This process is performed for each point available and for each chosen mode. Finally, results obtained on each measurement point are visualized and averaged to obtain the modal identification final results. The standard deviation is also calculated to evaluate the accuracy of the results.

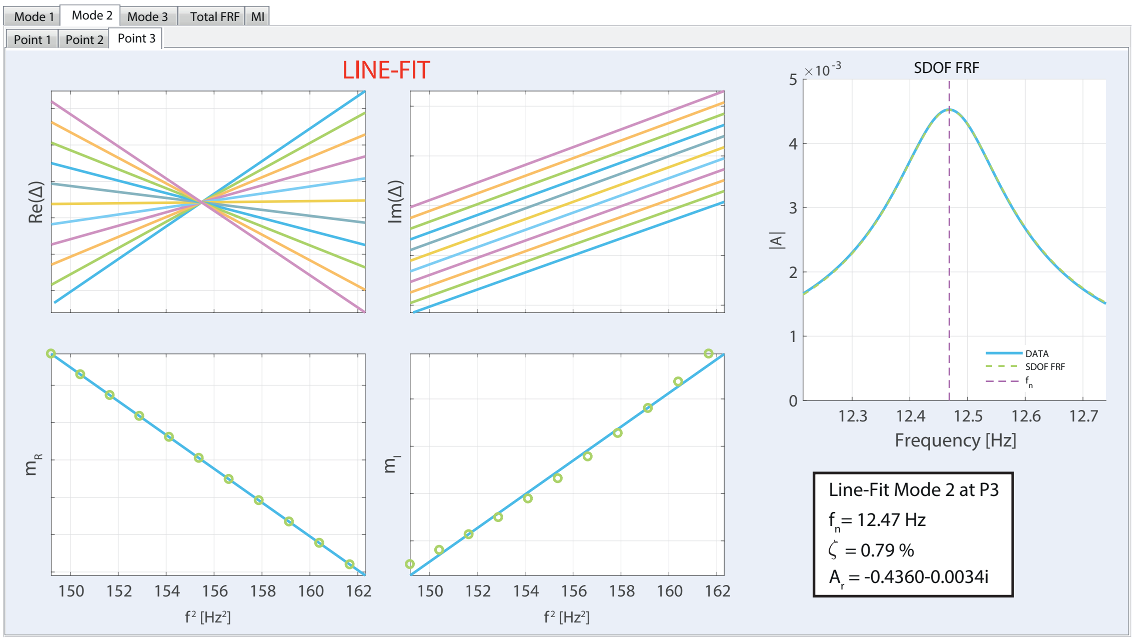

Line-Fit Mode 2 at P3
f_n = 12.47 Hz
ζ = 0.79 %
A_r = -0.4360-0.0034i

Figure A.1 – Example of Line-Fit method application on a linear 3-DOF system.

A.2 Nonlinear extension

The Line-Fit method is a linear modal analysis tool. However, it can be adapted to treat lightly nonlinear system. The process is exactly the same as before, but this time we add some features in order to see if we can discern and characterize a nonlinear behavior.

The procedure is the same until the calculation of the coefficients m_R and m_I, which are the slopes of the reala nd imaginary parts of the Δ function. At this point, instead of interpolating the full sets of coefficients m_R and m_I, the latter are divided into N_{est} subsets, and each one of these is interpolated to identify the modal quantities. In order to be more precise, an overlay factor N_{over} can be defined in order to create the subsets like a moving average and avoid sudden variations in modal identification results.

Each one of the subsets can then be related to a certain receptance amplitude, and the identified natural frequency and damping ratio can be visualized as functions of the receptance amplitude.

An example of this approach is applied on a three masses system in which an Iwan model has been implemented. The results are shown in fig. A.2 for the second mode at the 3^{rd} degree of freedom. It's possible to see how the Δ function — especially the imaginary part — is different from the linear case of fig. A.1. In addition, the set of coefficients m_R and m_I are divided into $\mathrm{N}_{est} = 10$ subsets. Then, in the bottom plots, the results of the nonlinear identification can be observed. As expected, it's possible to see a softening effect for the natural frequency, while for the damping the behavior is not clear. Finally the linear and nonlinear receptance reconstruction are compared with the experimental one in the left figure. The nonlinear reconstruction follows better than the linear one the experimental data.

Of course we are not saying that this is a complete nonlinear modal identification tool, but it can be very helpful in a preliminary test phase to qualitatively identify nonlinearities in the system under study, and to understand for which modes a deeper and more complete analysis is required.

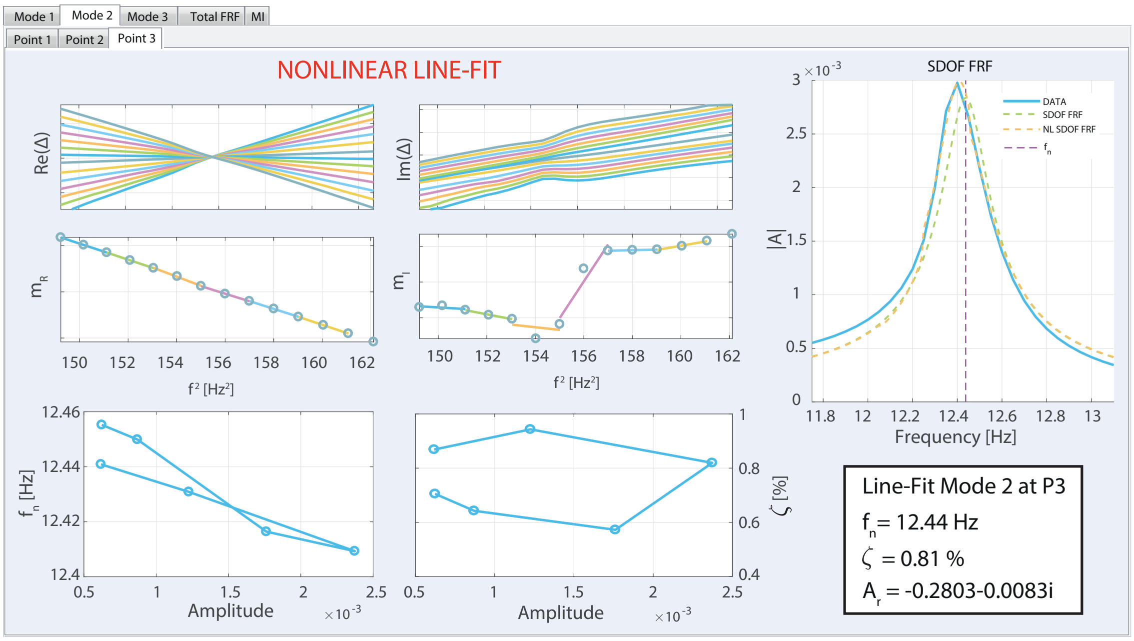

Line-Fit Mode 2 at P3

f_n = 12.44 Hz

ζ = 0.81 %

A_r = -0.2803-0.0083i

Figure A.2 – Example of nonlinear Line-Fit method application on a three-masses system with an Iwan model.

A.3 Advantages and Limitations

After having described the method theory and its application to a general case, it's time to point out its limitations and advantages.

Concerning the limitations, the latter lie principally in the fact of being a single degree-of-freedom identification technique, and its inability to consider several modes at once, and to combine different measurements. Furthermore, user interaction and interpretation of results is still important. In fact, the user has to select the range of frequency around each resonance and to visually check the results in order to avoid odd behaviors.

Turning to the advantages, these can be summed up in a few points:

1. The method id fairly simple and straightforward;
2. The modal residual $B_{r_{jk}}$ is automatically considered.
3. Unlike other SDOF modal identification methods such as the Circle-fit, it doesn't rely heavily on the points measured close to the resonance, and on the frequency resolution. In fact, with its inverse nature, the data that are most important are the one further from the resonance peak.
4. It can be used to spot non-linearities, even in its linear version, by observing discrepancies and abnormalities in the Δ function.

Finally, it's important to specify that the method have been used in its purely linear form to perform the linear modal analysis of the AERO mock-up in free-free conditions and when mounted on the electromagnetic shaker.

Bibliography

[1] Dobson, B. J. (1987). A straight-line technique for extracting modal properties from frequency response data. *Mechanical Systems and Signal Processing*, 1(1):29–40. I

[2] Maia, N. M. and Silva, J. M. (2001). Modal analysis identification techniques. *Philosophical Transactions of the Royal Society A: Mathematical, Physical and Engineering Sciences*, 359(1778):29–40. I

université
PARIS-SACLAY

ÉCOLE DOCTORALE
Sciences mécaniques et
énergétiques, matériaux
et géosciences (SMEMAG)

Titre : Contribution à l'ètude de l'amortissement dans les assemblages vissés.

Mots clés : Liaisons vissés, connecteur, frottement, filtre de Kalman, analyse modale non-linèaire.

Résumé : La dynamique des structures assemblées est un sujet de recherche actuel. En particulier, une prédiction correcte de l'amortissement apporté par les liaisons vissés est devenu une condition essentiel pour un certain nombre d'applications, comme par exemple les avions et les véhicules spatiaux. En effet, pour ces applications, l'utilisation de matériaux avec un coefficient d'amortissement plus élevée, comme des matériaux visco-élastiques, est limité par les conditions de fonctionnement.

Ces travaux apportent deux contributions principales. La première porte sur la phase de conception et modélisation, avec la création d'un système de connecteurs pour la reproduction des comportements normal et tangentiel d'une liaisons vissée. Cela est accomplie en considérant seulement les données physiques de la liaison et des surfaces en contact. La deuxième contribution concerne l'évaluation des propriétés dynamiques non-linéaires des assemblages. Un set d'outils de post-traitement utilisant le filtre de Kalman est développé pour réaliser une analyse modale non-linéaire pour les types d'essais les plus communs: les essais aux chocs, les essais en balayage sinus, et les essais en sinus aléatoire.

Les méthodes développées ont été appliqués et évaluées sur une structure boulonnée réel, en soulignant les avantages et les inconvénients. Notamment, le filtre de Kalman permet une meilleure précision sur les paramétrés identifiés, mais le procédé d'initialisation du filtre est le problème principal. Une automatisation partiel de l'initialisation est prévu, ainsi que des conseils pratiques grâce à l'expérience acquise sur le sujet.

Title : Contribution to the study of damping in bolted structures.

Keywords : Bolted joints, finite element connector, friction modeling, Kalman filter, nonlinear modal analysis.

Abstract : Bolted structures dynamics is an ongoing research topic. In particular, a correct prediction of the damping provided by bolted joints has became an essential requirement for a certain number of applications, such as aircrafts and space vehicles. In fact, for these applications, the use of materials with higher damping coefficients is limited by environmental conditions.

This work provides two main contributions. The first one concerns the design and modeling phase, with the creation of a finite element connectors' system, that reproduces the bolted joint normal and tangential behaviors. The latter is accomplished only by taking into account readily available physical data, such as the bolted joint dimensions and the properties of the surfaces in contact. The second contribution regards the evaluation of assembled structures' nonlinear dynamic properties. A set of post-processing tools making use of the Kalman filter is developed to perform a nonlinear modal analysis for the most common types of experimental tests: impact hammer tests, sweep sine tests, and random vibration tests.

The developed methods are then applied and evaluated on a real bolted structure, pointing out advantages and drawbacks. In particular, the Kalman filter allows for a higher accuracy in the determination of modal parameters, but the filter initialization is the main problem. A partial automation of the initialization task is provided, together with practical tips thanks to the experience gained on the subject.

Université Paris-Saclay
Espace Technologique / Immeuble Discovery
Route de l'Orme aux Merisiers RD 128 / 91190 Saint-Aubin, France